Hydrodynamic Simulation of Active Galactic Nuclei in Galaxy Cluster

christoph becker

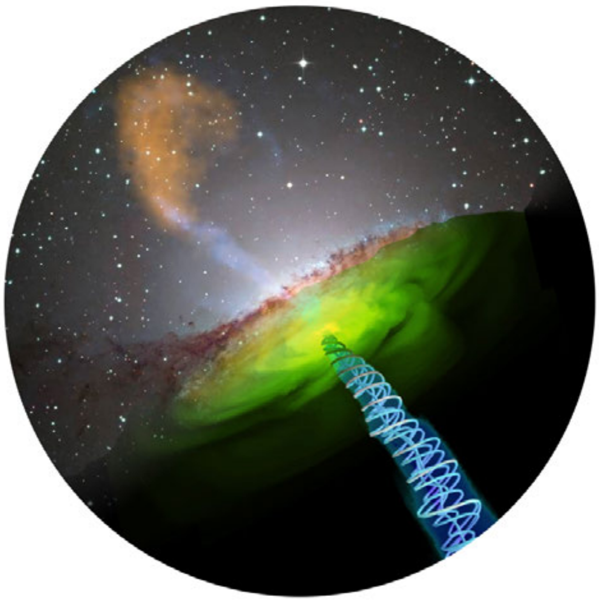

January 2017

Hydrodynamische Simulation von Aktiven Galaxie Kernen in Galaxienhaufen

Hydrodynamic Simulation of Active Galactic Nuclei in Galaxy Cluster

Master Arbeit
Master Thesis

zur Erlangung des Master of Science
for the Master of Science degree in natural science

an der Fakultät für Physik
at the Faculty for Physics

der Ludwig-Maximilians-Universität (LMU), München
of the Ludwig-Maximilians-University (LMU) of Munich

vorgelegt von
presented by

Christoph Becker

aus Berlin, Deutschland
from Berlin, Germany

München, August 10, 2017

Supervisors:	Prof. Dr. Klaus Dolag,	(USM, LMU)
	Prof. Dr. Giuseppe Murante	(INAF, Trieste)
	Prof. Dr. Stefano Borgani	(INAF, Trieste)

... Also the astronomers surely will not have to continue to exercise the patience which is required for computation... For it is unworthy of excellent men to lose hours like slaves in the labor of calculation which could safely be relegated to anyone else if the machine were used.

— Leibnitz 1674

ABSTRACT

Active galactic nuclei (AGN) are among the brightest objects in universe and the least understood. They interact with their environment through several energy feedback mechanisms such as radiation, winds, and jets. Even though many details of these feedback processes are still to be worked out, it is certain that they strongly influence the evolutionary history of their host galaxy and galaxy clusters. Furthermore can AGNs hold the answers to open standing questions of observational measurements such as star formation rate quenching in galaxies and the cooling catastrophe of the intra-cluster medium.
In this work, the effects of AGNs on galaxy clusters were studied with the help of the TreePM-SPH-code GADGET-3. The main focus lies on the comparison of two AGN feedback routines, which have the treatment of the radio-mode as their major difference. Since this is a preliminary study of concepts, low resolution simulations are used. Whereas the fiducial simulation implements the mechanical outflow, which dominates in the radio-mode, as thermal feedback, the new simulations impart kinetic energy. This is motivated through the closer agreement with a unified AGN model.

CONTENTS

LIST OF FIGURES

ACRONYMS

AGN Active Galactic Nuclei
BCG Brightest Cluster Galaxy
BH Black Hole
BLRG Broad-Line Radio Galaxy

CMB	Cosmic Microwave Background
EW	Equivalent Width
FoF	friends-of-friends
FWHM	Full Width at Half Maximum
FSRQ	Flat-Spectrum Radio Quasar
GBH	Galactic Black Holes
HPQ	Highly Polarized Quasars
HST	Hubble Space Telescope
IC	Initial Condition
ICM	Inter-Cluster Medium
IGM	Inter-Galaxy Medium
IMBH	Intermediate-Mass Black Hole
IMF	Initial Mass Function
ISM	Inter-Stellar Medium
JWST	James Webb Space Telescope
LINER	Low-ionization nuclear emission-line region
LOS	Line-Of-Sight
MBH	Mirco Black Hole
MIR	Mid InfraRed
MHD	MagnetoHydroDynamics
NLRG	Narrow-Line Radio Galaxy
OVV	Optical Violent Variables
PBH	Primordial Black Hole
QSO	Quasi-Stellar Objects
QSRO	Quasi-Stellar Radio Objects
SBH	Stellar Black Hole
SF	Star Formation
SFR	Star Formation Rate
SKA	Square Kilometer Array
SN	Supernova
SPH	Smoothed Particle Hydrodynamics
SMBH	Super Massive Black Hole
VLBR	Very Long Baseline Array
WHIM	Warm-Hot Intergalactic Medium

ASTRONOMICAL AND PHYSICAL CONSTANTS

Physical Constants

Speed of light	c	$2.997\,924\,58 \times 10^{10}\ cm\, s^{-1}$
Planck constant	h	$6.626\,07 \times 10^{-27}\ g\, cm^2\, s^{-1}$
Boltzmann's constant	k	$1.380\,65 \times 10^{-16}\ erg\, K^{-1}$
Gravitational constant	G	$6.6738 \times 10^{-8}\ cm^3\, g^{-1}\, s^{-2}$
Electron mass	m_e	$9.109\,383 \times 10^{-28}\ g$
Proton mass	m_p	$1.672\,621\,8 \times 10^{-24}\ g$
Thomson cross-section	σ_T	$6.65 \times 10^{-25}\ cm^2$

Astronomical Constants

Solar mass	$1\ M_\odot$	$1.989 \times 10^{33}\ g$
Solar luminosity	$1\ L_\odot$	$3.839 \times 10^{33}\ erg\, s^{-1}$
Light year	$1\ ly$	$9.4605 \times 10^{17}\ cm$
Parsec	$1 pc$	$3.0857 \times 10^{18}\ cm$
		$3.2616\ ly$
Hubble constant	H_0	$70.8\ km\, s^{-1}\, Mpc^{-1}$

1

INTRODUCTION

Active galactic nuclei (AGN) are the most energetic objects in the Universe. This compact region at the centre of a active galaxy (the host galaxy of an AGN) comprises a broad class of subtypes that collectively occupy a vast parameter space. The diversity makes it difficult to rigorously categorize these objects, which let to frequent changes in their definition as more of them were discovered. With our current understanding, we think of a AGN as an object, which is fundamentally powered by accretion onto a supermassive ($> 10^5 M_\odot$) black hole (SMBH).
The history of our understanding of AGN is a long and complex one, which always relied on the advances of other research areas. The first documented person to have observed an AGN is Edward Arthur Fath in 1908. Although back then, this object was interesting whim for entirely different reasons than they are today for scientists. During his time at the Lick Observatory, he undertook a series of observations of astronomical objects, which were then known as "spiral like nebulae". His studies inadvertently settled the question, which reached back until 1750, when Tomas Wright speculated that some of the nebulae seen in the sky were not actually part of the Milky Way, but rather independent 'Welteninseln'. Spending long nights of observing the sky, he wanted to find out the true nature of spiral like nebulae.

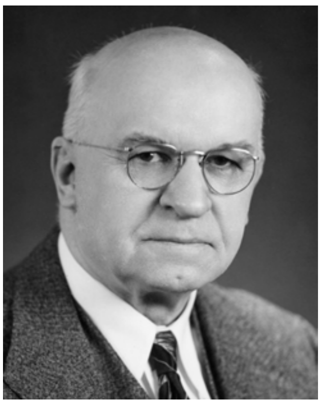

Figure 1.1: Edward Arthur Fath: 1880-1959

Analyzing his data, he found a absorption line spectra, suggestive of an unresolved collection of solar-type stars. He concluded that they needed to be clusters of stars, which are very far away, outside of the Milky Way (Fath [70]). This was contra to the common believe that those objects are nebulae located in the Milky Ways, sending out a continuous spectrum.
However, in the case of one of his observed spiral nebulae, NGC1068, he noticed that the spectrum is composite, showing both bright emission and dark absorption lines. There were six bright lines, recognizable as the ones seen in the spectra of gaseous nebulae.
NGC1068, which is also labeled as M77, is now known to be a barred spiral galaxy about 47 million light-years away, having a AGN in it's centre. After Fath's publication, NGC1068 gained much attention and was under more detailed investigation by Slipher [162], Hubble [100], and Seyfert [156]. The latter published the first systematic study of galaxies with high-excitation nuclear emission lines, like those of NGC1068, which are now called

after him Seyfert galaxies (pronounced 'seefurt').

During the time of WWII, many observatories scaled back their work and only a few astronomers where working full time on their research. Therefore, WWII slowed down the scientific progress in astrophysics. However, it fueled others, which would become invaluable for the astronomical community. The most prominent being radio engineering and computer science.

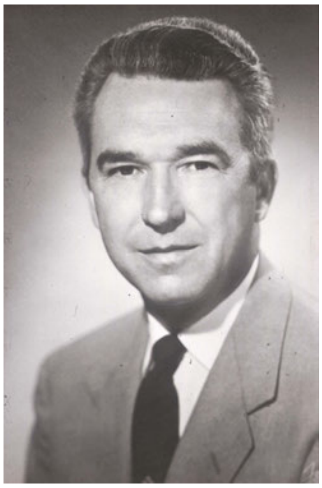

Figure 1.2: Carl Keenan Seyfert: 1911-1960

Karl Jansky was the first radio engineer, turning his attention to the sky. Using a rotatable antenna, he studied for three years a phenomenon that he described as: "a steady hiss type static of unknown origin". He concluded in 1935 that the radiation came from the entire disk of the Milky Way, being strongest in the direction of the galactic centre. This lead to the beginning of radio astronomy. WWII lead to a great progress in radio technology, as it was realized, that maintaining control of a huge army over large distances is impossible, without having the means for fast and wireless communication. As the war ended, several groups of radio engineers, who know had the time again to follow their interest, used the technological advances for the study of radio astronomy.

Just as the military funding enabled radio astronomy to advance, did it give Alan Turing the ability to turn his theories on computability into practice. At Bletchley Park he build his first computers named Bomb and Colossus. They were meant to decipher high-level German army messages produced by Enigma and the Lorenz machine. The success of the cryptanalysis machines secured Turing funding by the government also after the war and was asked to build duplicates of the Bomb for the United States in 1943. John von Neumann, who would later become the designer of the 'von Neumann'-architecture which still is the basis of most modern computer designs, became seriously interested in computational mathematics when he visited England in 1943. During a train ride from London to Greenwhich, von Neumann wrote his first computing program, which lead to his realization of the importance of this new technology. When von Neumann build the IAS electrical computer at Princeton University, which operated from 1952 to 1957, he would give up to 50% of the computer time to the department of astrophysics. He understood that astrophysics differs from other physical sciences by the circumstance that its objects of study can be observed but cannot be experimented with. This impossibility of physical experimentation can be compensated for to a remarkable degree by numerical experimentation. The other point was, that many astrophysical problems can't be solved analytically, making the use of numerical methods inevitable.

The first breakthrough in radio astronomy was made in 1943 with the realization, that at least some radio sources are extragalactic. Until then it was believed, that the discrete radio sources with small angular sizes originate from 'radio stars' in our galaxy. Through the joint work of optical and radio astronomy, John G. Bolton, Gordon J. Stanley and Owen B. Slee identified radio sources with already optically known galaxies [20]. One radio source, named Virgo A, was found to be identical with the optical identified galaxy M87. A large elliptical galaxy, with a jet, which was first described in 1918 by Curtis et al.[43] of the Lick Observatory as a "curious straight ray [...] connected with the nucleus by a thin line of matter".

Figure 1.3: This Hubble Space Telescope photograph shows the jet of matter ejected from M87 at nearly the speed of light, as it stretches 1.5 kpc (5 kly) from the galactic core.

The progress in radio surveys, position determinations, and optical identifications, enabled Baade and Minkowski[6] in 1954 to take emission lines of two radio sources, Cas A and Cyg A, and estimate their redshift to be $z \approx 0.05$, implying an enormous luminosity of $8 \times 10^{42} erg/s$ (as a comparison the bolometric solar luminosity is $3.83 \times 10^{33} erg/s$) in the radio (for the now known values of H_0 the radio luminosity is even larger).
These results were puzzling, since such tremendous energy outputs where hitherto unseen and propelled the interest to find theoretical frameworks. First attempts tried to explain the galactic radio background in terms of thermal emission by interstellar dust (Whipple and Greenstein[190]), free-free emission by ionized gas in the interstellar medium (Reber[142]), and extragalactic "radio stars" (Alfvén and Herlofson[4]). The discovery by Woltjer[191] in 1959, that a mass of $M > 1.3 \times 10^8 M_\odot$ in the central $100pc$ is required, to explain the concentration of emission of the nucleus of the Milky Way and NGC1068 brought us a stop close to the current understand of AGN. With such a high mass, Hoyle and Fowler[98] found out that the luminosity could be explained with an massive object in the centre of these galaxies, emitting mainly by accretion processes of a surrounding disk of gas. This idea was taken further by Salpeter [149] and Zel'dovich and Novikov [193], who assumed that the accreting body in the centre could be a SMBH. The idea of a SMBH in the centre of active galactic nuclei and also in the centre of our own galaxy was a powerful model. It explained not

only the large energy output based on the release of gravitational energy through accretion phenomena, but also the small size of the emitting regions.

The advent of the use of computers in astrophysics in the 50's was mainly to understand stellar physics, which is highly non-linear and can't be analytically solved. The 60's saw the beginning of N-body simulations due to Von Hoerner [187] and Aarseth and Hoyle [1], who simulated clusters of stars ($N = 4 - 16$) and galaxies ($N = 25 - 100$) respectively. With the development of fast and efficient algorithms to deal with collisionless systems, such as particle-mesh codes Hockney and Eastwood [95] and the tree method Barnes and Hut [8], cosmological dark matter only simulations made a leap forward. For collisional systems, regularization techniques were developed to deal with close encounters and binary dynamics (e.g. see Aarseth's NBODY-X code series based on KS and chain regularization - Aarseth and Aarseth[2] and references therein).

Next to advancements in algorithms grew the CPU speed exponentially, making larger simulations possible. Today's N-body simulations are performed with up to $7210^3 \approx 374 \times 10^9$ particles for a collisionless cosmology (New Horizon simulation, Kim et al. [110]). Simulations of AGN gave us insight in the evolution of galaxies, otherwise unattainable. They gave explanations to the sharp drop-off in the galaxy mass function above $M_* \simeq 10^{11} M_\odot$, prevention of the cooling catastrophe in galaxy clusters, and the production the hot gas atmospheres seen around many galaxies.

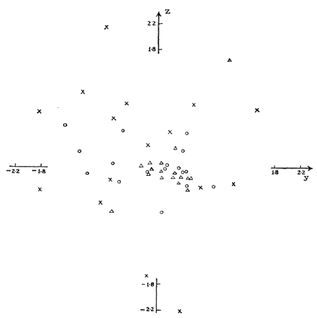

Figure 1.4: Aarseth's simulation of a $N = 50$ galaxy

Having started as a narrow discipline, AGN research combines now many areas including large-scale structure formation, galaxy evolution, particle physics, and the physics of extremely energetic phenomena like γ-ray jets just to name a few. Whereas in the mid-70's about 200 articles were being published in refereed journals per year on AGNs, now more than 1000 become publicised.

This thesis will give a glimpse onto the current theoretical and observational pictures of AGNs in Ch. 2. How cosmologies with the current theoretical framework are explored with the help of smoothed particle hydrodynamics (SPH) is outlined in Ch. 3. An analyzes of the resulting simulation space is given in Ch. 4, followed by the discussion Ch. 5 and ending with the conclusion Ch. 6.

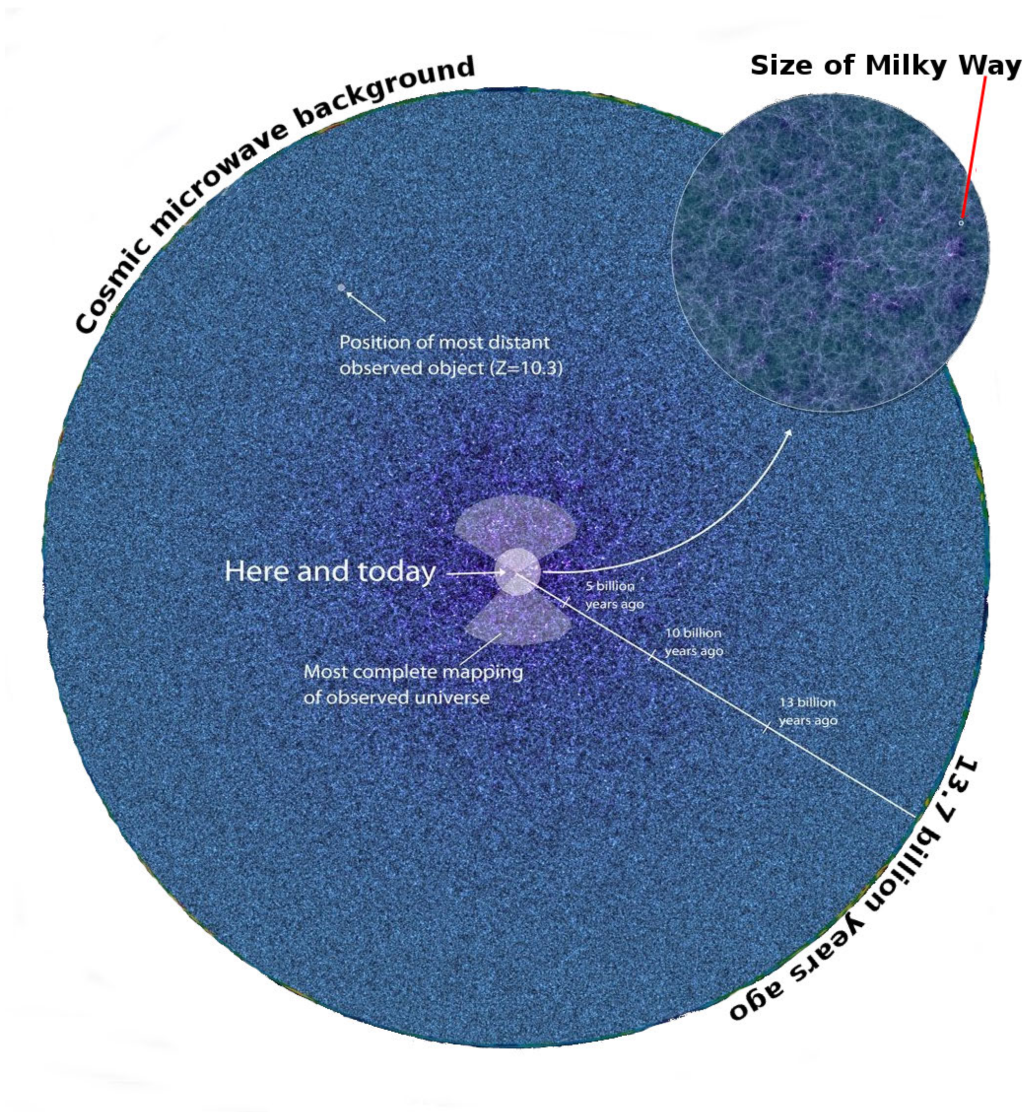

Figure 1.5: Volume of the universe accessible through the New Horizon simulation, i.e. the full observable universe. At the edge of the disk extracted from the full celestial sphere, we find the Cosmic Microwave Background
Graphic from the DEUS consortium.

2

THE OBSERVATIONAL PICTURE OF AGNS

Active galactic nuclei [1] stands for galaxies with a accreating supermassive black hole (SMBH) in their centre. In the 13th 'Veron Catalog of Quasars & AGN', 168.941 objects are registered [184]. It is estimated that in the local universe, at $z \leq 0.1$, about 1 out of 50 galaxies contains a fast accreting SMBH, and about 1 in 3 contains a slowly accreting supermassive BH.
In the following, a summary on the current understanding of AGN based on observational and theoretical models is given.

2.1 AGN ORIGIN

Over the past decades, a growing body of observational and theoretical evidence has suggested that SMBHs exist in the centres of all galaxies with spheroids (e.g. Kormendy and Richstone [113]; Ferrarese and Merritt [73]) and that the properties of these SMBHs are tightly correlated with the properties of the spheroid in which they reside.
The exact mechanisms leading to the tight observed coupling between galaxy spheroidal components and central AGN are not yet fully understood, although it has long been recognized that the formation mechanisms of SMBHs (e.g. Silk and Rees [160]) and stars (e.g. Dekel and Silk [50]) are most likely self-regulating. These results suggest that the same processes that shape galaxy spheroids also act on the central BHs. Correlations between AGN activity and other processes provide other clues about the mechanisms that lead to the buildup of the SMBH population.
The massive BHs present in the centres of galaxies are likely to have started their lives as 'seed' BHs. The typical masses of seed BHs remain somewhat uncertain, and depend upon the mechanism by which they form. Plausible mechanisms include the collapse of Population III stars, giving rise to BHs with masses in the range $10^2 < M_{BH} < 10^3\, M_\odot$ (e.g. Madau and Rees [117]; Islam, Taylor, and Silk [102]), and direct collapse of matter in high-redshift, low angular momentum haloes, which may give rise to seed BHs with masses $\sim 10^5\, M_\odot$ (e.g. Begelman, Volonteri, and Rees [15]6; Volonteri and Natarajan [186]). These seed mass BHs can then grow either by mergers with other BHs or through accretion of gas and/or stars.

2.2 AGN TYPES AND UNIFICATION

The mystery of AGNs is that they produce very high luminosities in a very concentrated volume, probably through physical processes other than the nuclear

1 As it is used since 1968, when at the Solvay Conference on Physics, V.A. Ambartsumian addressed the "enormous explosions" taking place in galactic nuclei and called them 'active nuclei'.

fusion that powers stars. AGN are thus special laboratories for extreme physics which one would like to understand. They are also our principal probes of the Universe on large scales, so understanding them is essential to studying the formation and evolution of the Universe.
Nowadays, AGN are defined by six main properties, as stated by the National Radio Astronomy Observatory:

(i) very compact angular size

(ii) high luminosity

(iii) Continuum emission from the core, meaning that the objects emit radiation at a range of wavelengths from radio to X-ray and sometimes even γ-range

(iv) emission lines, which can in some cases be up to 1000 $km\,s^{-1}$

(v) variability of the continuum and spectral line emission

(vi) strong emission of radiation at radio wavelengths

Besides these common factors, AGN span a vast parameters space. Masses of the central BH can range from $10^5 - 10^{10}\,M_\odot$ and bolometric luminosities have been measured from $10^{41} - 10^{48}\,erg\,s^{-1}$ ($10^8 - 10^{15}\,L_\odot$). This has led to a division in many subgroups and the attempt to find a unified model. Thereby it is important to note, that the classification of an AGN depends on the frequency range in which sources are studied. This has the consequence, that the same object can belong two to AGN subgroups simultaneously.

A general scheme, shown in Table 2.1, which tries to classify AGNs is a modified version of Tadhunter[177], who uses separate types for LINERs and Blazars. It is based on the emission lines visible in the optical domain.

Type	Optical lines	Radio-quiet	Radio-loud
Type-I	Broad and narrow	Seyfert 1	FSRQ, SSRQ, BLRG
	lines	Seyfert 1.5	
		NLS1	
Type-II	Narrow lines only	Seyfert 1.8, 1.9, 2	NLRG, type 2 QSO
	Weak narrow lines	LINER/LLAGN	WLRG
Type-0	No lines	SgrA^*?[(a)]	BL Lac, OVV, FSRQ
		QSO (BALs)	

Table 2.1: The general AGN classification, based on the emission lines visible in the optical domain. Images of some AGN types can be found in the appendix A.3
[(a)] It is not quite clear yet how to classify SgrA^*. Currently ALMA is observing SgrA^* with the longest baseline ever used with ALMA. The results will give us more clarification.

In the following, the main differences between AGN Type-0,-I,-II, radio-quiet, and radio-loud will be clarified.

2.2.1 *AGN of Type-I, Type-II and Type-0*

Type-I and type-II AGNs are mainly differentiated through the obscuration of the central region.
Type-I AGNs are those objects with little or no obscuration of radiation in the central $\sim 1000\,R_g$ around the BH (with R_g the gravitational/Schwarzschild radius, given in App.). Furthermore do they have very broad permitted lines, more than about $1000 - 30.000\,km\,s^{-1}$. [2]
Type-II AGNs have a completely obscured line of sight to the centre at UV, optical, and NIR wavelengths and permitted lines with FWHMs that are significantly smaller than of type-I AGNs ($< 1000\,km\,s^{-1}$) and are consistent with the velocities of stars in the host galaxy.
Due to the ambiguity of the threshold between type-I and type-II AGN, there always are exceptions to this simplified scheme. Thus, line width by itself cannot be used to distinguish thoroughly type-I from type-II AGNs.
In most type-I sources, the forbidden lines are considerably more narrow than the permitted lines. In type-II sources, the width and other features of the forbidden line profile are very similar to the permitted lines. An additional difference between the groups is the line EW. In high-luminosity type-I AGNs, the forbidden lines are seen against the AGN continuum, and hence their EWs are considerably smaller than in type-II sources, where the lines are seen against the (fainter) stellar continuum.
To detect and measure the line-of-sight-obscuring column in AGNs is most efficiently done with X-ray observations. Numerous observations of type-II sources show a wide column density distribution with a peak at around $10^{23}\,cm^2$ and a long tail toward very large columns. X-ray obscuration is not restricted to type-II AGNs. In fact, most low-luminosity type-I sources show some X-ray absorption along the line of sight with column densities that range between 10^{21} and few $10^{23}\,cm^{-2}$.

Very different from the other two are type-0 AGN, which represent a small subgroup of very unusual spectral characteristics. An prominent example are blazars, which can be subdivided into BL Lacertae (BL Lac) , flat-spectrum radio-loud quasars (FSRQ), optically violently variables (OVV) and highly polarized quasars (HPQ). Blazars are highly variable core-dominated radio-loud sources showing polarization at radio and optical wavelengths. Many blazars are also powerful γ-ray emitters, and some of them show indications of superluminal motion. To be more specific, a blazar is defined as an AGN that shows one or more of the following properties:

(i) Intense, highly variable high-energy emission in the γ-ray part of the spectrum.

2 It is necessary to mention here, that different thresholds have been used in the literature to distinguish type-I and type-II AGN ranging from $1000\,km\,s^{-1}$ (e.g. Stocke et al.[173]) up to $2000\,km\,s^{-1}$ (e.g. Fiore et al.[75]). The minimum and maximum value found in literature are further used to define type-I AGNs.

(ii) Intense, highly variable radio emission associated with a flat radio spectrum and, occasionally, superluminal motion.

(iii) Radio, X-ray, and/or γ-ray jet with clear indications for relativistic motion.

(iv) A double-peak SED with a lower-frequency peak at radio-to-X-ray energies and a high-frequency peak at X-ray-to-γ-ray energies.

(v) Very weak (small EW) broad and/or narrow emission lines indicative of photoionization by a nonstellar source of radiation on top of a highly variable continuum.

The common model for blazar emission is that these sources are quasars in which a relativistic jet is pointing at the observer, or very close to the observer's line of sight.

2.2.2 *Radio-quiet and Radio-loud AGN*

The definition, what a radio-loud and a radio-quiet AGN is, has not always been the same over the years. Nowadays, radio-loudness is usually defined as flux ratio of the radio band versus the optical band. Sramek and Weedman[168] used K-corrected[3] flux values,

$$z = \frac{\lambda_{observed} - \lambda_{emitted}}{\lambda_{emitted}} = \frac{u_{emitted} - u_{observed}}{u_{observed}} \tag{2.1}$$

of the observed versus emitted energy band, defining the radio-loudness as:

$$R^* = \frac{f_{5GHz}}{f_{2500\mathring{A}}} \tag{2.2}$$

Sometimes a source is called radio-loud when the simple flux ratio is larger than 10, or if the radio luminosity is larger than $L_r > 10^{33}\, erg\, s^{-1}\, Hz^{-1}$ (Stocke et al.[173]). For radio-quiet, Peterson[135] used as definition $0.1 < R < 1$. Another way to make the distinction is to use the spectral slope between the optical and radio band. This can be defined as

$$a_{ro} = \frac{log \frac{L_{5GHz}}{L_{2500\mathring{A}}}}{log \frac{u_r}{u_o}} = \frac{logR^*}{5.38} \tag{2.3}$$

Here, sources with $a_{ro} > 0.35$ ($R^* > 76$) are called radio-loud (Della Ceca et al.[52]).
Another difference in appearance is, that radio-loud objects produce large scale radio jets and lobes, with the kinetic power of the jets being a significant fraction of the total bolometric luminosity. Whether jets are ubiquitous in AGN (as theorized by Mannheim[118]) or only found in radio-loud AGN (as the work of Lal, Shastri, and Gabuzda[114] suggests) is still debated and depends mainly on

3 K correction to an astronomical object's magnitude allows a measurement of a quantity of light from an object at a redshift z to be converted to an equivalent measurement in the rest frame of the object.

the achievable resolution of the central region. So far, of all detected AGN, 10% possess a jet. However it may be, that one can say that the weak radio ejecta of the radio-quiet objects are energetically insignificant.
With surveys such as SDSS [174], NVSS [38], and FIRST [12], very detailed statistical studies of the AGN host galaxy were made possible. Thus now it is known, that radio-loud objects are associated with elliptical galaxies which have undergone recent mergers, while the radio-quiets prefer spiral hosts.
Furthermore is the space density of radio-loud AGN at a given optical luminosity ≈ 10 times lower than that of the radio-quiet AGNs.
Additionally, only the radio-loud AGN are prolific emitters of gamma radiation (photons with energies above $\sim 100\,keV$), which believed to result from Compton scattering within the relativistic jets.
The radio-loud AGN have variability characteristics that are distinct from their radio-quiet counterparts. Variability in these objects is widely believed to be dominated by emission from a relativistic jet.
Moreover, studies (e.g. Best et al.[17]) have shown that the fraction of radio AGN increases strongly for more massive galaxies, suggesting that radio jets are more readily triggered in galaxies with more massive black holes.

2.2.3 *AGN Unification*

A fundamental question in AGN research is, whether all these distinct appearances of the AGN phenomenon can be explained by a common underlying model, or whether the different classes are intrinsically distinct.
The first attempts to construct unification models for AGNs were in the 80's following various polarization experiments that were able to show the presence of broad emission lines in polarized light in type-II sources. The present generally accepted unified scheme depends on the following parameters: orientation, black hole mass, accretion rate in terms of Eddington ratio, and covering factor.
Using a axisymmetric model, Antonucci[5] could explain with the orientation of the axis, and a central obscuration the spectral differences between type-I, type-II, and type-0 AGNs (see Fig. 2.1). The central obscurer is toroidal and the exact structure is an active field of research. Current results are in favor of a clumpy structure [63] instead of a smooth one [136] (as was assumed earlier, mainly due to computational limitations). For a clumpy structure the covering factor has to be added to the parameters in the unifying scheme. It gives the probability of detecting a type-I or type-II AGN depending on the observing angle with respect to the axis. Models involving central tori of different properties are quite successful in explaining many AGN properties, including the relative numbers of type-I and type-II sources in the local universe.
A direct correlation of the radio luminosity with black hole mass had been found in several investigations. This connection has roughly the form of $L_r \propto M_{BH}^{2.5}$, according to Franceschini, Vercellone, and Fabian[76], and confirmed in several other studies (e.g. [130]). Thus, following this result, an AGN is radio-quiet of radio-loud depending on its black hole mass. On the contrary, Ho[94] did not find a simple relation between the radio luminosity and M_{BH}. This motivated

Component	Distance in R_g	Density in cm^{-1}	Ionization parameter	Characteristics
Jet	0	$\sim 10^3$		found in 10% of all observed AGN
Accretion disk	~ 100	$\sim 10^{15}$	$U_{oxygen} = 10^{-3} - 10^{-1}$	
BLR	$10^4 - 10^5$	$\sim 10^{10}$	$U_{hydrogen} \sim 10^{-2}$	high velocity, high density gas on pc scales
Torus	$10^5 - 10^6$	$10^3 - 10^6$	$U_{oxygen} = 10^{-2}$	gaseous & molecular absorbing medium in equatorial plane
HIG	$\sim 10^5$	$10^5 - 10^5$	$U_{oxygen} = 10^{-2}$	
NLR	$10^7 - 10^8$	$10^5 - 10^5$	$U_{hydrogen} = 10^{-2}$	lower velocity, lower density gas on kpc scales
Starburst	$10^7 - 10^8$	$10^0 - 10^3$	$U_{hydrogen} = 1 - 10^{-2}$	

Table 2.2: AGN components: Location, density, ionization parameter, and characteristics

Garofalo, Evans, and Sambruna[80] to consider the relative spin of the central black hole with respect to the accretion disk to be the crucial unifying factor. This scheme predicts that the highest prograde black hole spins might be discovered in the least active AGNs. This scenario is supported by a theoretical approach of Daly ([45], [46]) determining the black hole spin that is model-independent, but assuming that spin changes only by extraction of the reducible black hole mass. This shows us, that the separation of AGN into sources with and without a jet (radio-quiet and radio-loud) is not as clean as assumed in the past.
If the unified scheme is considered as correct, one can derive the following AGN composition:

Even though the present unified scheme has been quit successful in explaining many AGN phenomena, many recent findings are posing challenges (e.g. [108]). With the evaluation of current (Herschel Observatory) and future space-based IR observations (James Webb Space Telescope), the judgement of the correctness of the current unified scheme will be guided.
The final quest is to find a grand unified scheme which not only applies to BH in AGNs, but also to the galactic black holes (GBH).

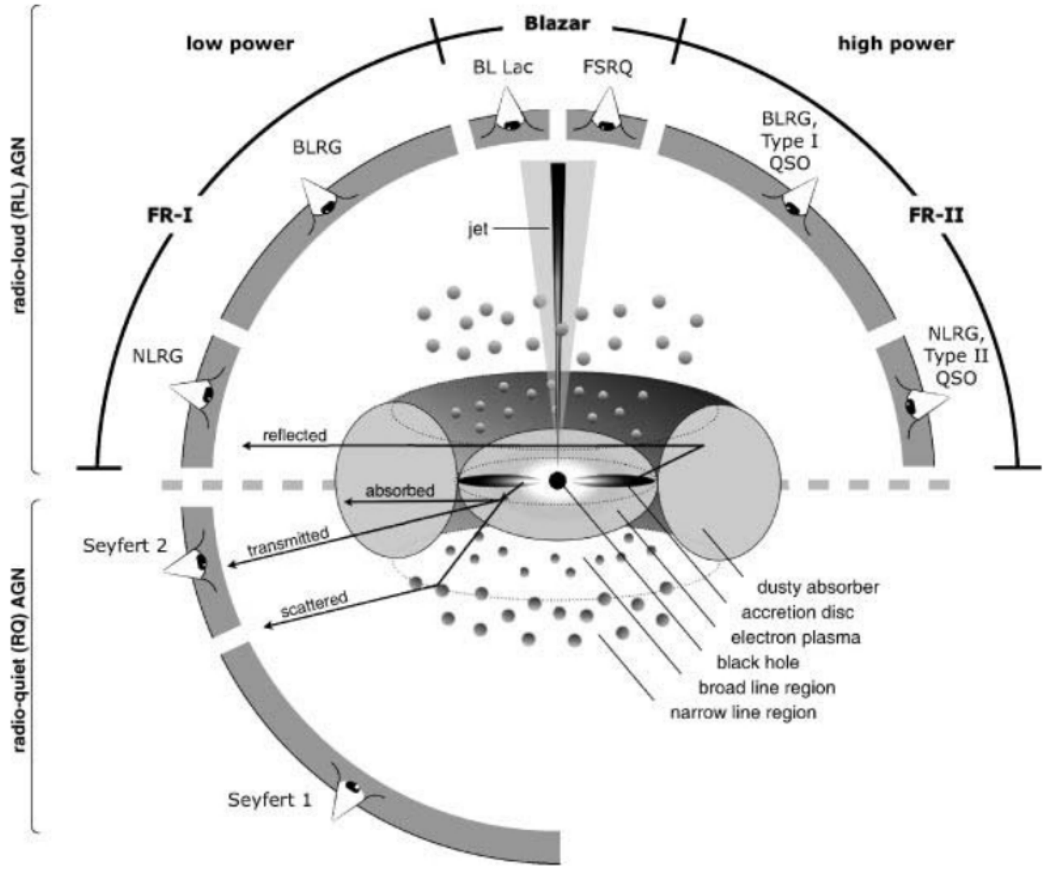

Figure 2.1: Schematic representation of our understanding of the AGN phenomenon in the unified scheme. The type of object one sees depends on the viewing angle, whether or not the AGN produces a significant jet emission, and how powerful the central engine is. Note that radio-loud objects are generally thought to display symmetric jet emission.
Graphic by Beckmann and Shrader [13].

2.3 AGN ACCRETION

Over the past decades, a picture has emerged in which SMBHs are embedded in dense stellar systems in the centres of galaxies and increase their masses primarily by the accretion of gas (e.g. Begelman and Rees [14])
In an astrophysical context, accretion describes the inflow of matter toward a central gravitating object. It is one of the most ubiquitous processes in astrophysics, traversing many scales. Starting with small objects such as comets, which can form by accreting cometesimals in the Oort cloud, up to galaxies, which formed early in the universe as gas flowed in toward the centre of gravitational potential wells established by dark matter.

The first hypothesis on the formation of large gravitating bodies, came from R.M. Du Ligondes Du Ligondès and Moreux[57], T. C. Chamberlin Chamberlin[30], and F.R. Moulton Moulton[127] in the beginning of the 20th century. However, their ideas remained unnoticed, until O. Yu. Schmidt revived them in the 1944, which lead to an increasing interest into analyzing accretion processes.
As accretion processes were studied more carefully, it became apparent that it is a highly efficient way of converting rest mass energy into radiation, with an efficiency of $\sim 10\%$ [4]. Thus, a lot higher than nuclear burning in the core of stars, which liberates at most $\sim 0.7\%$ of the rest mass energy. This realization led to believe, that a massive BH could be present in the centre of a AGN, as mentioned in Ch. 1.
Nowadays there are many different accretion models for different scenarios. Details of the exact nature of BH accretion flow remain to be worked out, however, disk accretion scenarios are strongly favored by theoretical arguments.

The simplest accretion scenario one might consider is a spherically symmetric flow onto a compact object which is at rest with its surrounding. It is generally referred to as Bondi accretion, although F. Hoyle and R. Lyttleton lay the foundations for him (Hoyle and Lyttleton [99]; Bondi and Hoyle [23]; Bondi [22]). A compact object will accrete matter at an approximate rate of

$$\dot{M} = 4\pi r^2 \rho(r) u(r), \tag{2.4}$$

where $\rho(r)$ and $u(r)$ are the baryon density and velocity at a given radial distance r.

To find the total accretion rate r needs to be integrated. A useful starting point for the integration is the radius r_{sonic} at which the gas inflow becomes supersonic. The radius is found through the Euler's equation by setting $u = c_s$, where c_s is the sound speed, which gives

$$r_{sonic} = \frac{GM_{BH}}{2c_s^2}. \tag{2.5}$$

4 An insight into the derivation of such efficiency is given in App. A.2

Now the Bernoulli integral can be used to relate c_s and ρ at distance r with r_∞, assuming a polytropic medium,

$$\begin{aligned} c_{s,sonic}^2 &= c_{s,\infty}\left(\frac{2}{5-3\gamma}\right)^{1/2}, \\ \rho_{sonic} &= \rho_\infty\left(\frac{c_{s,sonic}}{c_{s,\infty}}\right)^{2/(\gamma-1)}, \end{aligned} \tag{2.6}$$

where the raltion $c_s^2 \propto \rho^{\gamma-1}$ was used.

Inserting equ. 2.6 into equ. 2.4 gives then:

$$\dot{M} = \pi G^2 M_{BH}^2 \frac{\rho_\infty}{c_{s,\infty}^3}\left(\frac{2}{5-3\gamma}\right)^{(5-3\gamma)/2(\gamma-1)} \tag{2.7}$$

For $\gamma \to 5/3$, the accretion rate becomes

$$\begin{aligned} \dot{M} &= \pi G^2 M_{BH}^2 \frac{\rho_\infty}{c_{s,\infty}^3} \\ &= \pi\left(\frac{GM}{c_{s,\infty}^2}\right)^2 \rho_\infty c_{s,\infty} \\ &= \pi r_{acc}^2 \rho_\infty c_{s,\infty}, \end{aligned} \tag{2.8}$$

where r_{acc} is the accretion radius and represents the approximate radius of influence of an accreting body. It is defined as:

$$r_{acc} = GM_{BH}/c_{s,\infty}^2. \tag{2.9}$$

However, in most cases the ambient medium is not at rest (e.g. BH moving through a uniform interstellar medium). The compact body is then exposed to a wind of velocity $u_{w,\infty}$ which it accretes. Setting the potential and kinetic energy of the wind medium equal, gives us an approximation for the accretion radius:

$$r_{w,acc} = \frac{2GM_{BH}}{u_{w,\infty}^2}. \tag{2.10}$$

Inserting this in the Bondi accretion rate (equ. 2.4) gives

$$\dot{M} = \frac{4\pi G^2 M_{BH}^2 \rho_\infty}{u_{w,\infty}^3}. \tag{2.11}$$

Bondi went further than this and treated the accretion in its velocity- and temperature limit seperatly, to arrive at an intermediate result between those two extremes:

$$\dot{M} = \frac{4\pi G^2 M_{BH}^2 \rho_\infty}{(u_{w,\infty}^2 + c_{s,\infty}^2)^{3/2}}. \tag{2.12}$$

Ultimately, accretion onto a compact object is limited by the effects of the radiation pressure experienced by the in-falling plasma, which forms close to the centre. This limit, first pointed out by Arthur Eddington in the 20's, depends on the mass of the compact object and the mean opacity of the in-falling material.

The Eddington limit therefore describes the balance between the force of radiation acting outward and the gravitational force acting inward. The observational quantity corresponding to the critical mass-accretion rate is the Eddington luminosity, L_{Edd}. It can be obtained by using the hydrostatic equilibrium equation

$$\frac{dP}{dr} = \frac{-GM\rho}{r^2}, \tag{2.13}$$

together with the radiation pressure equation,

$$\frac{dP}{dr} = \frac{-\sigma_T \rho}{m_p c} \frac{L_{Edd}}{4\pi r^2}. \tag{2.14}$$

Here, M is the central object mass, σ_T is the Thomson scattering cross-section and m_p the proton mass. This leads to:

$$L_{Edd} = \frac{4\pi G M m_p c}{\sigma_T} \simeq 1.3 \times 10^{38} \frac{M}{M_\odot} \, erg\, s^{-1}. \tag{2.15}$$

One knows that the Eddington limit is reached, if the ratio between the bolometric luminosity and Eddington luminosity equals one.
However, Bondi accretion is unlikely to power AGN, as has been found by measuring the X-ray luminosity of nearby nonactive galaxies, which were orders of magnitude smaller than what would be predicted based on the Bondi accretion rate.

Through the law of conservation of angular momentum, one knows that orbiting material always settle into a disk. Even though this is and was common knowledge, it was much harder to write down a mathematical model for it. The problem is that the total angular momentum of the system must be conserved, thus, the angular momentum lost due to matter falling onto the centre has to be offset by an angular momentum gain of matter far from the centre.
The physical mechanisms underling this transport of angular momentum is an active field of study. Though, an common used approximate solution was found in the 70's by Shakura and Sunyaev[157], which is now called the α-disk model.

Theoretically there are parameter-space regimes where the assumptions of the α-disk model break down. This can happen if e.g., the viscosity of the disk is high, prohibiting efficient cooling and causing thickening of the disk into a torus. Possible observational arguments for such case are found in the presence of double-peaked emission lines, most commonly in Hα, as found by Eracleous and Halpern[65].

It has been shown that X-ray binaries switch between two states: 1) 'low/hard' state: a steady radio jet is present and the hard X-ray spectrum is observed 2) 'high/soft' state: the jet vanishes and the X-ray spectrum shows a soft, thermal component.
The multitude of different AGNs, has lead to the question, whether it actually is possible to construct a simple unified model that accounts for the different modes

of AGN in a cosmological framework. First attempts have been made ([36]; [42]; [124]), motivated by the observational findings of X-ray binaries ([71]; [79]). It has been shown that X-ray binaries switch between two states:

(i) 'low/hard' state: a steady radio jet is present and the hard X-ray spectrum is observed.

(ii) 'high/soft' state: the jet vanishes and the X-ray spectrum shows a soft, thermal component.

The transition between these two states is regulated by the accretion rate on the BH, where the threshold value is of the order of $10^{-2} - 10^{-1}\,\dot{M}_{Edd}$. The 'low/hard' state corresponds to optically thin, geometrically thick and radiatively inefficient accretion, as described by the theoretical Advection-Dominated Accretion Flow (ADAF) ([128]) model. The 'high/soft' state can be explained by the standard, optically thick and geometrically thin accretion disc ([157]), with BH accretion occurring at high rates and in a radiatively efficient mode. This suggests that there are also two distinct phases of AGN accretion: the radio-mode and the quasar-mode correspond to the 'low/hard' state ([147]; [125]) and 'high/soft' state (e.g. [64]; [140]) respectively.

2.4 AGN FEEDBACK

As was outlined in the previous section, accreted matter will lose energy through radiation when it gets closer to the BH. To get an rough idea of the order of magnitude of energy which is liberated, one can do a simple back-of-the-envelope calculation and assume $E_{BH} = \epsilon M_{BH} c^2$, where ϵ is the efficiency (10% as mentioned before). If one takes the Andromeda galaxy as an example, which carries a SMBH of $\sim 1.8 \times 10^8 M_\odot$ ([16]), one finds that $E_{BH} \sim 2 \times 10^{62}\,erg\,s^{-1}$ is released through the growth of the SMBH. The binding energy of matter to its host galaxy can me approximated with $E_{gal} \sim M_{gal}\sigma^2$, where σ stand for the stellar velocity dispersion. The mass of the Andromeda galaxy is $\sim 1.5 \times 10^{12}$ ([133]) and $\sigma \sim 160\,km\,s^{-1}$ ([82]). Using this simple calculation, one finds that $E_{BH}/E_{gal} > 40$. Thus the energy produced is enough to heat and blow away the entire gas content of the galaxy and prevent cooling. However, since Andromedas SMBH is not accreting at the moment, this is not happening.
Fortunately accretion energy does not significantly affect the stars already existing in the host galaxy, or there would not be any galaxies as we know them. Albeit it can have a profound impact on e.g. the star formation rate (SFR) in the galaxy. To what extent AGN feedback influences the fate of it's host galaxy or the cluster in which the host galaxy resides is one of the largest controversies in extragalactic physics. On one side is the claim of little to no interaction, meaning that a SMBH is at the centre of a big galaxies simply because they grew simultaneously On the other side is the believe of a close correlation between the central engine (SMBH) and the environment, with a feedback process regulating AGN growth and starburst activity in the host. Indeed there is a plethora of observational and theoretical studies that suggest that several different channels for interaction of BHs with their surroundings exist.

In low mass galaxies where stellar feedback is important, there is little or no evidence at the present time for AGN feedback operating or that it significantly affects galaxy disks, or pseudobulges. The clearest observational evidence for AGN feedback is found in the most massive galaxies known, brightest cluster galaxies (BCGs) in cool core clusters of galaxies.
The uncertainty of the importance of AGN feedback will hopefully be resolved, when the James Webb Space Telescope (JWST) will be launched in October 2018.
In the previous subsection two accretion modes of AGNs were mentioned, which correlate with the emission properties of AGNs according to the unified model. This suggests a rather simple, yet attractive scenario for distinguishing between different modes of BH feedback in models for the cosmological evolution of AGNs: at high accretion rates, a 'quasar-like' feedback occurs. also called radiative-mode, while for states of low accretion, mechanical bubble feedback applies, also called radio-/kinetic-mode. It is clear that the simplicity of this model will not allow it to explain all kinds of AGN feedback phenomena, e.g. powerful radio galaxies that accrete at very high rates, as found in some protocluster environments, are not well represented in this simple scheme.

2.4.1 *The Radiative and Wind Feedback*

There is a large variety of radiative processes triggered by AGNs, which dominate the AGN feedback if the SMBH accretes close to the Eddington limit, thus in the quasar-mode. These processes take mainly place in the accretion disk, the extended clumpy disk, the BLRG, and the inner parts of the central torus. Furthermore they are responsible for the $M - \sigma$ relation on a galactic scale [67] as is explained below. The simplest radiative feedback is achieved by a strong radiation field, ionizing a large fraction of the surrounding gas, hence increasing its temperature and preventing it from forming stars. In this case, the efficiency depends on the level of ionization and the opacity of the absorbing gas, including its dust content. Simulations show that the interstellar medium can be heated up to $10^6\ K$ by the AGN activity through photo-ionization and Compton heating (e.g., Kim et al.[109])
But photons can also directly push material out through radiation pressure. The effect on ionized gas is low though, because of the lower cross-section, thus the effect is limited in the vicinity of the AGN, where the photon flux is strongest. Radiation pressure on dust particles is more efficient and the transfer of momentum from the photons to the dust can be close to 100%, if the dust occupies a large solid angle.
The coupling of photons and particles through radiation pressure can cause quasi-spherical high velocity winds from the outskirts of the accretion disc. They have been theoretically hypothesized (e.g. Silk and Rees [160]; [66]) and observationally confirmation has been achieved in a number of cases (e.g. Chartas, Brandt, and Gallagher [31], Crenshaw, Kraemer, and George [41]). AGN winds can reach velocities from $10^3 - 10^4\ km\, s^{-1}$ (Crenshaw, Kraemer, and George [41], Reeves et al. [143], Tombesi et al. [178]), which hits and shocks against the ambient ISM. The shock temperature can be up to a few times $10^{11}\ K$, which is much greater

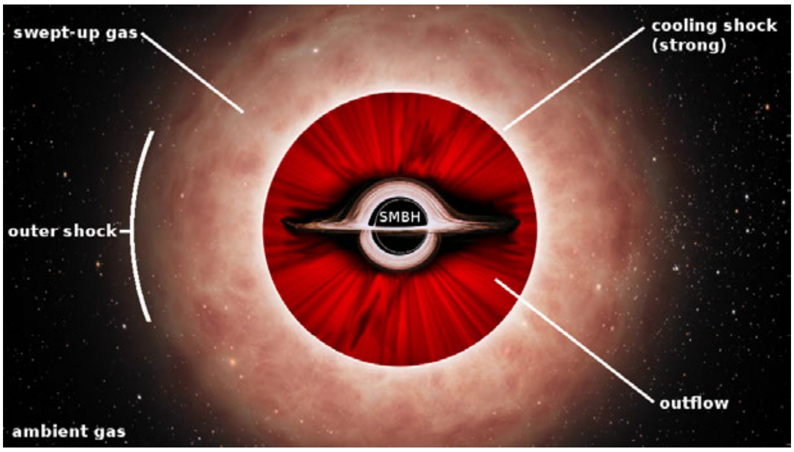

Figure 2.2: Schematic view of the shock pattern resulting from the impact of an Eddington wind on the ISM of the host galaxy. A SMBH accreting at just above the Eddington rate drives a fast wind ($10^3 - 10^4\ km\ s^{-1}$), whose ionization state makes it observable in X-ray absorption lines.

than the Compton equilibrium temperature ($T_C \sim 2 \times 10^7\ K$). The shocked wind therefore cools via the inverse Compton process against the photons of the AGN radiation field. A momentum-driven outflow is created, if the interaction between the wind and the ISM happens within a critical cooling radius. Inside this cooling radius the wind loses most of its original energy and only communicates its ram pressure to the ISM. A energy-driven outflow appears outside the cooling radius, because the wind cannot cool efficiently and most of its energy rate $\dot{E}_w \simeq \eta L_{Edd}/2$, where η is the radiative accretion efficiency, is communicated to the ISM. King [111] estimated the cooling radius R_C by comparing the wind cooling timescale:

$$t_C = \frac{2}{3}\frac{cR^2}{GM_{BH}}\left(\frac{m_e}{m_p}\right)^2\left(\frac{c}{u_w}\right)^2 \simeq 10^7 R_{kpc}^2 \frac{10^8 M_\odot}{M_{BH}}\ yr\,, \tag{2.16}$$

with the ISM flow timescale,

$$t_{flow} \sim \frac{R}{u_{out,m}} \simeq 7 \times 10^6 R_{kpc} \frac{\sigma}{200km/s}\left(\frac{10^8 M_\odot}{M_{BH}}\right)^{1/2}\left(\frac{f_g}{f_c}\right)^{1/2}\ yr, \tag{2.17}$$

where f_g is the gas fraction ($f_g = \Omega_b/\Omega_m$), f_c is the cosmological value of the baryon-to-dark-matter density fraction, and $u_{out,m}$ is the momentum-driven outflow velocity:

$$u_{out,m}^2 = \frac{GL_{Edd}}{2f_g\sigma^2 c}\,. \tag{2.18}$$

Setting both timescales equal, the cooling radius is found to be:

$$\begin{aligned} R_C &\simeq \frac{3GM_{BH}}{2c}\left(\frac{m_p}{m_e}\right)^2\left(\frac{u_w}{c}\right)^2\left(\frac{f_g\kappa\sigma^2}{2\pi G^2 M_{BH}}\right)^2 \\ &\sim 520\frac{\sigma}{200km/s}\left(\frac{10^8 M_\odot}{M_{BH}}\right)^{1/2}\left(\frac{v}{0.1c}\right)^2\left(\frac{f_g}{f_c}\right)^{1/2}\ pc\,. \end{aligned} \tag{2.19}$$

Hence the radius in which the outflow is momentum-driven depends on the SMBH mass. The critical mass threshold at which the outflow becomes totally energy-driven was derived by King [111], assuming a isothermal potential:

$$M_\sigma = \frac{f_g \eta}{\pi G^2}\sigma^4 \simeq 3.7 \cdot 10^8 \frac{f_g}{f_c}\sigma_{200}^4 M_\odot \,. \tag{2.20}$$

Once a SMBH mass reaches this value, the outflow can propagate to large scales as the SMBH continues to grow. This value is matching the observed $M_{BH} - \sigma$ relation (e.g Tremaine et al. [181]; Gültekin et al. [85]; McConnell and Ma [121]), provided that $f_g \simeq f_c$. This however is not a reasonable assumption when a galaxy cluster is studied. On one side, a galaxy in a cluster can be striped of gas from its outskirts through ram pressure and tidal forces.On the other side, the galaxy will be replenished with gas by cooling flows from the IGM. Zubovas and King [195] have found different approximations for the following galaxies:

(i) spiral galaxies with evolved bulges residing in gas-rich cluster environments have $M_{BH} \sim 3.7 \times 19^8 \sigma_{200}^4 M_\odot$ (such galaxies are however rare due to high merger probability in clusters)

(ii) elliptical galaxies close to cluster centres have $M_{BH} \sim 28 \times 10^8 \sigma_{200}^4 M_\odot$.

The outflow of ISM content leads to an self-regulation mechanism: if gas is abundant in the vicinity of the AGN core, there will be a high accretion rate, leading to enhanced emission which will drive out the gas, causing the starvation of the AGN.
This mode of feedback was probably most efficient at $z \sim 2-3$, when quasar activity peaked and galaxies were most gas rich. Observational evidence is patchy at that time due to obscuration of the active nucleus, making observations of this mode a very difficult task.

2.4.2 *The Mechanical/Kinetic Feedback*

Relativistic jets consist of ionized matter extending bi-conically from the galactic centre in the innermost 0.01 pc. They can appear in a variety of shapes, from long or short and stubby, nearly straight or sharply curved, and relatively smooth or dominated by knots (find images in App. A.3). Furthermore can radio jets exhibit a large range of apparent velocities, from mildly relativistic to highly relativistic motion.
The are classified into Fanaroff-Riley (FR) classes. FR-I sources have a low luminosity, with a power at 14 Ghz of $P_{14} < 10^{25}\ W\ Hz^{-1}$ and a brightness that fades gradually with increasing distance aways from the central object ('limb darkened'). FR-II sources have $P_{14} > 10^{25}\ W\ Hz^{-1}$ and are limb-brightened often show hot spots a few kpc across.
These hot spots are created by a series of shocks through which the relativistic jet terminates into non-relativistic speeds and causes a back-flow which inflates the radio lobe. Since these hot spots emit X-ray synchrotron radiation, the plasma inside must still posses relativistic speeds. At least at early times, the radio lobe can

have a significantly higher pressure than the surrounding intra-cluster medium (ICM). Consequently, the radio lobe undergoes a pressure-driven expansion into the surrounding ICM which is supersonic with respect to the sound speed in the ICM. This expansion drives a shockwave which sweeps up a shell of shocked matter into the ICM.

It can be assumed that with time the hot spot grows, expansion slows down, and

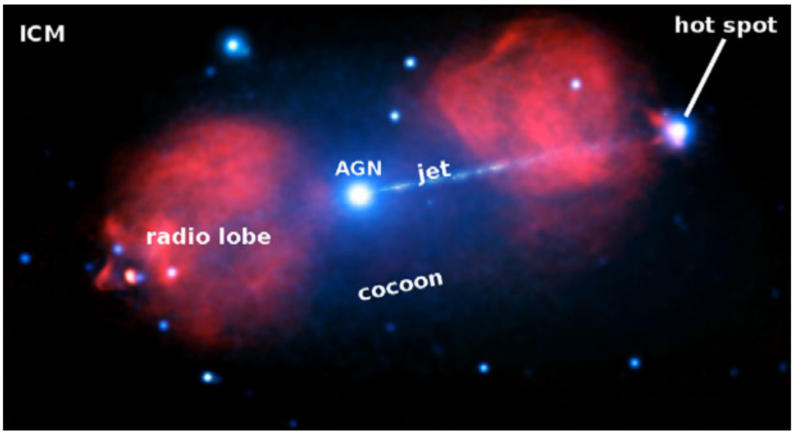

Figure 2.3: The Chandra X-ray image of the radio galaxy Pictor A shows nicely a jet that emanates from a AGN in the centre and extends across 300,000 years toward a brilliant hotspot and a counter jet pointing in the opposite direction. The radio lob (red) extends at both ends from the jet and the cocoon (blue) encompasses the whole radio galaxy with jets and radio lobes.
Credits: X-ray: NASA/CXC/Univ. of Hertfordshire/M. Hardcastle et al.

the pressure decreases. At some point the contact discontinuity between the hot spot and ICM will vanish due to Kelvin–Helmholtz and Rayleigh-Tayler instabilities. This leads to a mixing of the relativistic plasma with the shocked ICM as well as back-to-back buoyantly rising 'bubbles' of low-density mixed jet-plasma/ICM material ([35]; [123]). The jet energy is thermalized in the ICM through a combination of strong shock heating, dissipation of weak shocks/sound waves, and radio lobe-ICMs mixing.

How AGN jets form and the nature of their composition and mechanical configuration is uncertain. Three general categories of jet models are usually considered. The first is a thermal pressure model of the jet. Such models assume two anti-parallel channels that propagate adiabatically from the vicinity of the AGN. The second involves strong AGN radiation that can overcome gravity along certain directions and produce radiative pressure-driven jets.

The third model is the most generally accepted one. It uses hydromagnetic stresses exerted by magnetized accretion disks to explain the origin of the jet. Such flows would be centrifugally driven and magnetically confined. It is possible to show that under very general conditions, magnetohydrodynamical (MHD) winds will always be collimated asymptotically, even in relativistic flows.

The conventional picture involves magnetic fields threading roughly parallel to the accretion disk axis, as schematically shown in Fig. 2.4. The magnetic field is caused by the ionized content in the accretion disk. The combination of MHD and spinning BHs seems to be a promising model for explaining the jet creation pro-

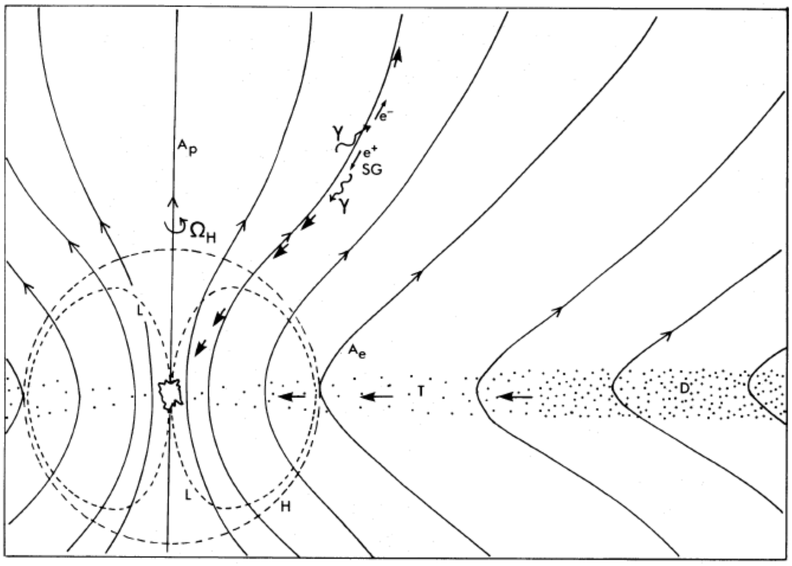

Figure 2.4: Schematic cross-section of AGN magnetosphere, using r and θ coordinates. H is the event horizon. The poloidal field surfaces (i.e. surfaces of constant A_ϕ) are shown as solid lines, with the polar, A_p, and equatorial, A_e surfaces specifically labeled. Projections of typical particle velocities are shown by arrows. Particles can remain on the hypersurfaces of constant A_ϕ only as long as the normals to these surfaces are space-like.
Graphic from Blandford and Znajek [19].

cess. For this scenario the frame dragging [5] potential of a rotating BH geometry (described by the Kerr spacetime) is responsible for driving the jet. Two important processes which make use of frame dragging are the Penrose effect Penrose [134] and the Blandford–Znajek effect [19].

The Penrose effect describes the extraction of rotational energy from a rotating BH. This is made possible, since the rotational BH energy lies outside the event horizon in the ergosphere. Inside the ergosphere a particle is necessarily propelled in locomotive concurrence with the rotating spacetime. Due to frame dragging, objects are split in two, of which one receives a momentum which sends it to infinity, whilst the other falls past the event horizon. The escaping piece of matter can possibly have greater mass-energy than the original infalling object, whereas the infalling piece has negative mass-energy, hence slowing down the rotation of the BH.

In the Blandford–Znajek effect, the magnetic field lines which are threading the accretion disk have to rotate with the matter inside the ergosphere. This will induce a force on the coupled charged plasma (Lorentz force) which will lead to acceleration of material at relativistic speeds along the rotation axis of the BH. This creates via magnetic confinement a well collimated jet, Fig. 2.5.

Further advances in the understanding of the basic problem of launching and powering the jets are likely to involve increasingly large and detailed numerical

5 Frame dragging can shortly be described by the shift of spacetime in the direction of the BH spin, thereby imparting energy to an orbiting particle.

simulations. Advances in computing capabilities as well as in the codes applied have led to slow, but consistent progress.

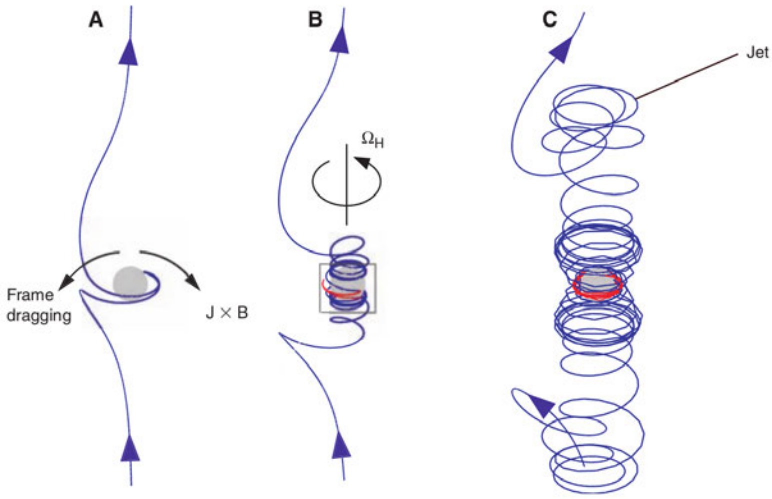

Figure 2.5: Illustration of how a spinning BH with a magnetic field around it may produce jets. Shown are computer calculations of the evolution of single magnetic field lines. A: The dragging of frames by the BH causes the field lines in the equatorial region to be pulled forward in the direction of the BH's spin. B & C: The field line becomes progressively more twisted with time, and the twist propagates outward relativistically to form twin jets.
Graphic from Narayan and Quataert [129].

2.5 AGN IN GALAXY CLUSTERS

Clusters of galaxies are the largest gravitationally bound systems in the Universe. Their mass can exceed $10^{15}\,M_\odot$, that is 3 orders of magnitude more than the mass of our own Galaxy with $M_{MW} \simeq 10^{12}\,M_\odot$ ([10]). AGN activity plays an important role in clusters of galaxies. First of all they are part of the evolution of cluster members, where they take part in AGN galaxy feedback mechanisms, driving gas out of the galaxy in large scale outflows, depleting gas reservoirs required for star formation ([151]; [120]). Depending on the geometry and energy, outflows from AGN can also trigger star burst events by compressing the IGM in the outflow to densities required for gravitational collapse ([101], [161]). Star bursts from AGN feedback, and gas removal by AGN outflows, both have the effect of depleting the IGM in cluster galaxies. In time, this will drive the cluster members towards early types in the Hubble sequence, consistent with the observation that clusters contain mostly early type galaxies.

Besides taking part in galaxy evolution, AGN may play a role in determining the structure of the cluster as a whole, by providing a mechanism for transferring energy to the ICM ([137]). The X-ray emission from the ICM in clusters enables the gas to cool efficiently. If no energy is added to the gas it will cool rapidly, and fall to the cluster centre. This is seemingly incompatible with the fact that cool X-ray emission is not observed from clusters of galaxies. This inconsistency is called the cooling flow problem ([68]). One of the possible explanations is that AGN activity in the central regions of the cluster deposit energy back into the ICM, pointing to a direct connection between supermassive black holes and clusters of galaxies ([192], and references therein). Dunn and Fabian [58] showed that 70% of the clusters with short cooling times (< 3 Gyr) show bubbles, and another 20% have a central radio source, indicating the potential for creating bubbles through jet emission.

An AGN in the core of a galaxy cluster will have further impact on its surroundings in addition to the heating of the ICM. AGN jets will transport heavy elements from the centre into the ICM. As cool, metal-poor gas can flow to the cluster centre, the AGN outflows will therefore lead to an efficient mixing. In simulations of bubbles created by AGN in galaxy clusters, Sijacki and Springel[159] showed that the cavities can alter the cluster properties. This effect is more important for cases involving relaxed, massive clusters in which the gas morphology is otherwise undisturbed. Because of the AGN heating, the cold baryon content is significantly reduced in the central galaxy and thus inhibiting its star formation.

Studying how AGN activity can be stimulated by increased availability of fuel, and how AGN outflows affect the host galaxy, is important in understanding how galaxies evolve in general, and in cluster environments in particular.

3 SIMULATION OF AGN IN GALACTIC CLUSTERS

According to the prevailing cosmological model, which says that our universe started from a singularity (commonly known as the 'Big Bang'), the 'age' of our universe is estimated to be 13.8×10^9 billion years (Ade et al. [3]). The thin disk of the Milky Way, in which our solar system is located in the Orion arm, has an approximated age of 8.8×10^9 years (Del Peloso et al. [51]). Our sun, which is defining our daily 10^{-4} year rhythm through it's motion on the sky, is 4.6×10^9 years old (Connelly et al. [39]). Considering the human life span, we have to realize that it is just a quant compared to the time scales in which cosmology functions. Thus astronomer's are forced to find other ways to study the evolution of our universe and how structure forms within it. With the rise of powerful computers, simulations proofed to be of ever more importance.
The first evolutional study was performed by Holmberg [96] in 1941, who had the brilliant idea to imitate the gravitational interaction of 74 bodies with light, send of light bulbs. This was long before first computational simulations were able to give relevant results. The arguably most important simulations, which started the era of computational astrophysics, are by Toomre & Toomre (1972) [180] and Toomre (1974) [179]. The authors presented simulations of two merging disk galaxies performed with a few hundred particles to understand the origin of what is known today as tidal tails and bridges, caused by the gravitational interaction of systems in the process of merging.

3.1 THE TREE-SPH CODE GADGET

The formation and growth of cosmic structures is a highly non-linear phenomenon that needs to be investigated with suitable numerical simulations. Since we can describe the motion of dark and baryonic matter as a fluid flow (non-collisional and collisional respectively), there are two main strategies to solve the hydrodynamical equations: Eulerian and Lagrangian techniques.
The former are methods that adopt a mesh to discretize the simulation volume, and all physical processes are treated as fluxes between the cells. In those codes, mixing between gas phases of different temperatures happens implicitly, but at high Mach numbers there exist problems with the Galilean invariance. In addition, adding gravity to the codes is somewhat cumbersome since no direct particle interactions can be calculated. This is especially problematic in simulations of dark matter and stars, since those components are collisionless.
The latter method in contrast, which uses smoothed particle hydrodynamics (SPH) codes treat all physics as particle-particle interactions, sampling the hydrodynamical properties and using hydrodynamic equations in their Lagrangian form to calculate the dynamical interactions. In order to avoid diverging forces if the dis-

tances between two particles become very small, the gravitational interactions are (gradually) suppressed on small scales. This scale is called the softening length. SPH codes are Galilean invariant, and the self-gravity of the gas is treated naturally with the same accuracy as for the stars and dark matter which interact directly through gravity. Furthermore do SPH codes have excellent conservation properties, are numerically very robust, and inherently adaptive. However, the mixing of gas phases with different temperatures is completely suppressed, and leads to 'Kaufmann-blobs'. This causes numerical artifacts in, inter alia, accretion rates, star formation rates (SFRs), disc sizes, and gas fractions. To improve the description of the gas physics and to accurately follow shocks, a artificial viscosity needs to be added at the particle level.

In this thesis, all simulations were performed using a extended version of the parallel TreePM-SPH-code GADGET-2 [163], called GADGET-3. TreePM-SPH codes determine the hydrodynamic properties using SPH, and the gravitational interactions are calculated using a Tree walk algorithm (see Hernquist and Katz [89] for more detail on Tree-SPH). GADGET-3 is based on an entropy-conserving formulation of SPH (Springel and Hernquist [165]).

To model the physics of the gas from which the stars are formed, additional processes and gas properties must be considered. In its standard version, GADGET-3 includes radiative cooling for a primordial mixture of hydrogen and helium (Katz, Weinberg, and Hernquist [105]), and star formation as well as the associated supernova feedback are included as sub-grid models according to Springel and Hernquist [166], assuming a Salpeter initial mass function (IMF) (Salpeter [150]). In case of cosmological simulations, additional heating due to the time dependent UV background is included (Haardt and Madau [86]). The interstellar medium is treated as a two-phase medium (McKee and Ostriker [122]; Efstathiou [60]; Johansson and Efstathiou [104]), where dense cold clouds are in pressure equilibrium with the thin hot gas they are embedded in.

To solve the issues of the phase-mixing problem, artificial conductivity schemes (Price [139]) can be implemented, for example those presented by Dolag et al. [55], as well as thermal conduction (Dolag et al. [56]). A more recent approach to this matter is presented by Beck et al. [11].

3.2 COSMOLOGICAL ZOOM-IN SIMULATIONS

To study the detailed structure of galaxy clusters and the impact of AGNs on them with appropriate resolution, it is essential to create zoomed initial conditions. This is done by first running a large dark-matter-only cosmological simulation, which will take long range gravitational forces with the surrounding cosmological structures of the galaxy cluster into account.

To model the initial conditions (ICs) for the cosmological simulation, at first all particles are placed on a cubic grid for the entire box (an alternatively is to use glass ICs). All particles have the same mass, and are homogeneously distributed. In the second step, a power-spectrum is applied to all particles. The power-spectrum specifies how likely each wavelength is present in the simulation, and it determines the initial displacements of the particles. Thus, after applying the power-spectrum to the particle grid, there are density fluctuations in the particle distribution of the initial conditions which lead to the filamentary growth of structures in the box during the simulation. With this set of initial conditions that is determined by the choice of the cosmological parameters, the box is evolved until $z = 0$. This box is called the parent simulation.

From this parent simulation, the galaxy cluster is selected at $z = 0$. All particles which are at any given time of the simulation part of the structure that should be simulated with higher resolution, are identified and traced back in time. The volume containing these particles from the selected galaxy cluster, and the regions around it since hydrodynamic simulations are sensitive to boundary conditions, are then re-simulated with higher resolution. This volume can either be restricted to those particles directly, causing the high- resolution region to have an amorphous shape, or be a box or a sphere containing all selected particles plus additional particles within the region. The latter is used to prevent low resolution particles from the surrounding areas to intrude into the high resolution volume, as those low-resolution particles have much higher masses and cause artificial dynamical friction when it drags the lower-mass particles in its wake. However, this procedure can become very computationally costly if the volumes are large due to the increasing amount of particles included in the high-resolution volume.

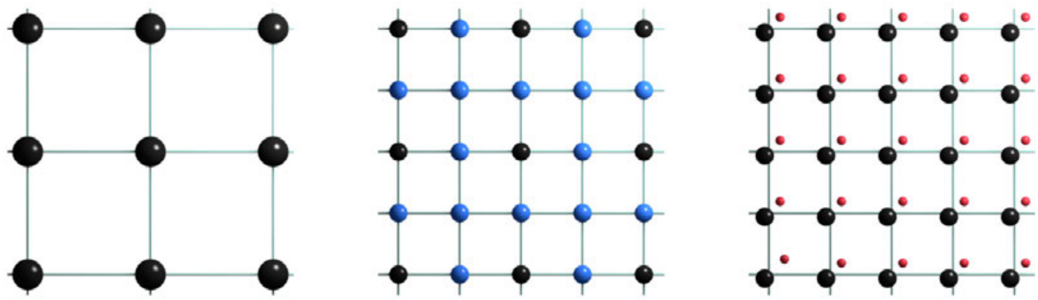

Figure 3.1: Two-dimensional illustration of the construction of the initial conditions of zoom-simulations from a parent cosmological simulation. Left panel: Example grid of the parent simulation for 9 dark matter particles (black spheres). Middle panel: Same as left panel but with twice the spacial resolution. Each dark matter particle (black spheres) has spawned three new dark matter particles (blue spheres), placed of the intersections of the new, spatially enhanced grid. The mass of the particles has been reduced by a factor 4. Right panel: Same as middle panel, but now all dark matter particles are shown in black. Each dark matter particle has spawned a gas particles with the gas particles mass according to the assumed baryon fraction split from the original mass of the dark matter particle, effectively lowering the mass of the dark matter particle. Each gas and dark matter particle pair is placed on the grid such that their center of mass is on the intersection point of the grid, and momentum is conserved.
Graphic from Remus [144].

In the next step, the particles inside the volume where a higher resolution should be achieved, are split into multiple particles, while the individual particle

mass is lowered accordingly. For example, to double the spatial resolution, each particle is split up in 2^3 particles with a mass of $\frac{1}{2^3} = \frac{1}{8}$ the mass of the parent particle. A two-dimensional representation of this process is shown in Fig. 3.1. In the left panel, the original grid is shown for 9 particles. The particles, illustrated as black spheres, are placed on the intersections of the gridlines. The resolution is increased by increasing the number of particles, as shown in the middle panel: The original particles are still at the same positions (black spheres), but their masses are reduced (i.e., in the figure the radii of the spheres are smaller). Within the grid of old particles, each particle has spawned three more particles (blue spheres) placed on the new intersections of the new grid lines. Since one particle has split up into four, the mass of each particle is $\frac{1}{4}$ of the original particle mass. In three dimensions, the process is the same but each particle is split up into 8 particles instead of 4. If the resolution should be n-times higher, the particles are split up into n^3 particles with each $\frac{1}{n}$ of the original mass.
In the high-resolution volume, baryons are often added as well. Since at the initial redshifts there are no stars formed yet, those new particles are all gas particles, and they all have the same mass, however, their mass is smaller than the mass of the dark matter particles. The gas particles are split from the dark matter particles, effectively lowering the dark matter mass of each particle. Hereby, the mass of the gas particles is usually calculated from the baryon fraction of the Universe. This baryon fraction can be calculated from observations of the cosmic microwave background (CMB). According to the newest survey of the CMB, the Planck Survey, the baryon fraction of the universe is $\frac{\Omega_b}{\Omega_m} = f_{bar} \approx 15.6\%$ [3]. Both particles together still have the same mass as the dark matter particle had before the introduction of the baryons. Also, both particles are still close to the same points of the grid where the parent particle was placed, but now their common center of mass is at the intersection while the particles themselves are slightly displaced such that their distance is the mean inter-particle distance and their momentum is conserved. This splitting is shown in the right panel of Fig. 3.1 for the two-dimensional case. The black balls mark the dark matter particles, the red balls illustrate the gas particles. Both are placed slightly off the grid, but since the dark matter particles are much heavier than the gas particles their displacement is much smaller.

The high-resolution volume is surrounded by a lower resolution volume, where the particle mass is higher but the number of particles is lower. Often, the same resolution is used as in the original parent simulation, and sometimes more than one low-resolution volume is used. Those low resolution particles are important to calculate the gravitational long-range forces on the high-resolution volume, however, if they intrude they can cause unphysical distortions. Thus, a careful selection of the high-resolution volume is important for a successful zoom-simulation.

With the new grid and the baryons in place, the power-spectrum is again applied to all particles. The power-spectrum is the same as for the parent simulation, however, for the high-resolution volume, the smaller modes of the power spectrum that have not been used for the parent simulation since the resolution was not high enough to include those small modes, are included down to the Nyquist frequency which corresponds to the mean particle separation in the high-resolution volume (Springel et al. [167]). Once the particles have been displaced, the initial conditions are set up and the simulation can be run until the desired redshift.

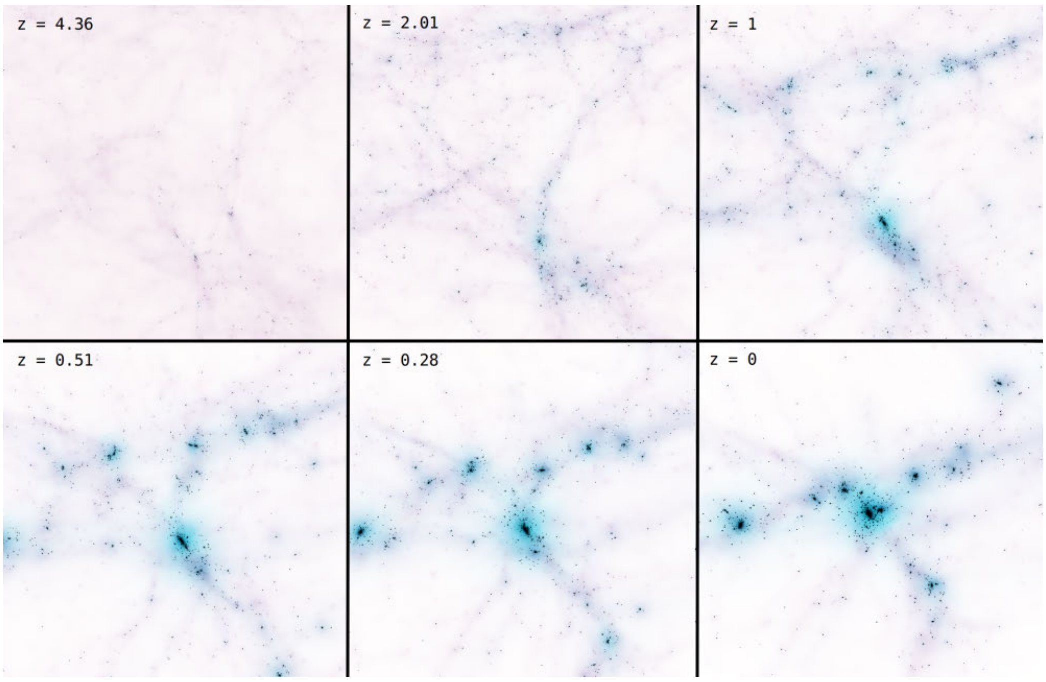

Figure 3.2: Visualisation of the Cosmological Zoom-In simulation on the studied cluster, showing six different redshifts. Gas is shown in as a gradient from white to blue, dependent on the entropy (white: low entropy, blue: high entropy). Stars are shown as black spots. All stars in the Cosmological Zoom-in simulations are formed from the gas. Upper left: z = 4.46. The filaments of gas from which the final galaxies are built up are visible, while there are only very few stars formed yet. Upper middle: z = 2.01. Structures of gas form inside the most dense gas regions. Upper right: z = 1.. While there is less and less gas, more and more stellar clumps are formed, which start to merge and build up larger structures. Lower left: z = 0.51. Lower middle: z = 0.28. A small group of medium sized galaxies has formed. Lower right: z = 0. A major merger of three halos, of which the lowest is the most massive in the simulated cluster.

One example of such a zoom-simulation is shown in Fig. 3.2, where the upper left panel shows the distribution of the baryons in the high resolution volume, and the amoeba-shape of the high-resolution area is still visible. Only gas particles (as vague lines) can be seen since there are no stars formed yet, however, the filamentary structure of the particle distribution caused by the power-spectrum is visible. Five more different redshifts are shown, with more stars visible each time (black points) and less gas. In the final stage, at z = 0, a major merger is seen of three very massive halos (name approx. mass).

For more detailed descriptions of the zoom-in re-simulation technique, see for example Borgani et al. [27]; Springel et al. [167]; Oser et al. [131].

3.2.1 *Cosmological Zoom-In Simulation Used in this Work*

The generation of the zoomed-in simulation of our analyzed galaxy cluster is described in Bonafede et al. [21]. The large cosmological DM only parent simulation was performed according to a flat ΛCDM cosmological model ($\Omega_\Lambda = 0.76$, $\Omega_0 = 0.24$, $h = 0.72$ and $\sigma_8 = 0.8$). The power spectrum for the primordial density fluctuations $P(k) \propto k^n$ is characterized by $n_s = 0.96$. The parent cosmological box of $1Gpch^{-1}$ was simulated with a comoving gravitational DM softening length of $2.52kpch^{-1}$. The subsequent cluster identification was performed by using a standard *Friend of Friends* (FoF) algorithm with a linking length of 0.16, which is the mean inter-particle separation between DM particles, corresponding to the virial overdensity in the adopted cosmological model.
Once the initial conditions for the DM components were obtained, gas particles were added. The mass of a DM and a gas particle is $0.84 \times 10^9\, M_\odot\, h^{-1}$ and $0.16 \times 10^9\, M_\odot\, h^{-1}$, respectively. The gravitational softening length used is $5kpch^{-1}$, which corresponds to the smallest SPH smoothing length reached in the dense cluster centres.
From the final output of the DM only run, a large region of $\approx 5 - 7\, R_{vir}$ around the cluster centers, which is free from of boundary effects, was selected and the particles within traced back to their initial positions. The Lagrangian region corresponding to the positions of these particles was enclosed in a box of side $L_{HR} \sim 62.5Mpc$, that forms the high resolution (HR) region. Since the volume occupied by the HR particles, V_{HR}, is usually only a fraction of the volume of the box (L_{HR}^3), the box is sampled with 64^3 cells, and cells which are occupied by the particles are marked. In order to obtain a volume with a concave shape and no holes in it, some more cells were marked around/within V_{HR}. This can be seen in Fig. 3.3, where the blue cells trace the V_{HR} region, while the additional cells marked to obtain a concave volume are marked in green and red. To minimize any changes in the tidal forces acting on to the high-resolution region, buffer around the HR region is created, and sampled with the same mass resolution as the parent cosmological simulation. The particles that occupy the marked cells are then traced back to the initial redshift of the simulation. This volume was re-sampled with a higher number of particles in order to obtain a higher mass resolution ($8.43 \times 10^8 M_\odot h^{-1}$ for DM particles of the simulations studied here). The HR particles were perturbed using the same power spectrum of the parent simulation, keeping the same amplitudes and phases. New fluctuations at smaller spatial scales were added, since smaller frequencies are now sampled by the higher resolution particles.
The remaining volume of the simulation was cultivated with low resolution (LR) and their density and velocity fields were re-sampled on to a spherical grid having constant angular resolution $d\theta$. The size of each cell $dr = rd\theta$ was chosen to obtain approximately cubic cells through the sphere. The interpolation on to a spherical grid reduces the number of LR particles to the minimum necessary to

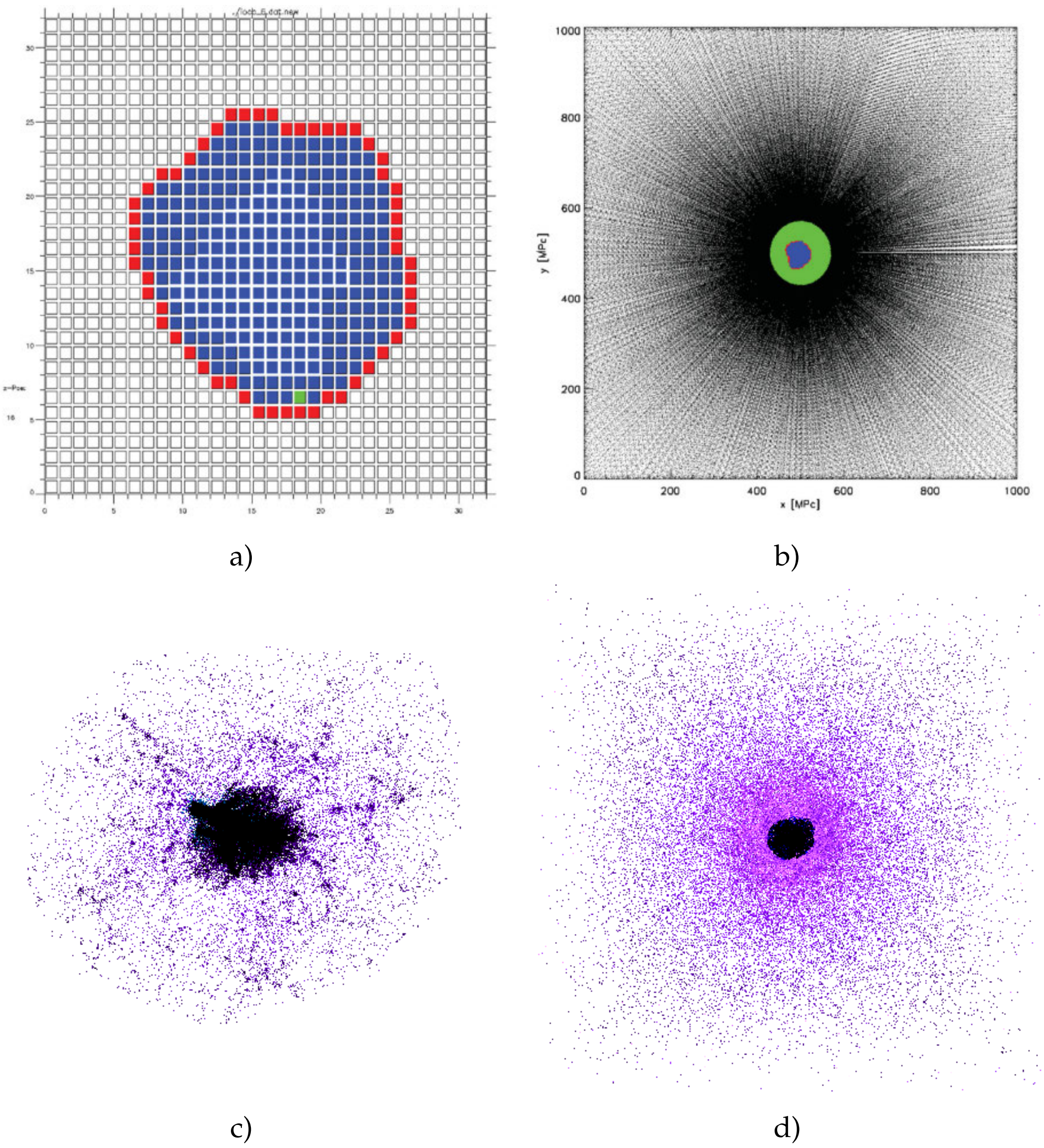

Figure 3.3: Figure a): Schematics of the Lagrangian region sampled with 64^3 cells. Blue: region where high-resolution DM particles have been split into gas and DM particles. Green and Red: added cells to achieve a concave HR region. Figure b): Schematics of the initial conditions for a zoomed-in simulation. The colour mean the same as in a) except: Black: DM particles with degraded mass resolution outside the HR region with increasing mass towards the outer regions. Green: DM particles outside the HR region with the same mass resolution than the parent simulation. This represents a 'safety region' where a normal grid is used and particles have the same mass that of the parent simulation. Figure c): Visible in violet are HR boundary particles which act as a 'safety region' for the cluster, which is the black nucleus. Figure d): Visible in violet are LR boundary particles spanning the whole parent cosmological box.
Graphics a) and b) from Bonafede et al. [21]

preserve the large-scale tidal field of the original simulation. By construction, as the distance from the HR region increases, dr increases too, and the mass of the LR particles increases accordingly. The overall volume simulated for each cluster is the same as the parent simulation, ensuring that the forming structures correspond to the same that formed within the original cosmological simulation. This initial condition were finally traced back to a higher redshift (e.g. $z = 70$) to ensure that the rms of the particle displacement in the HR region is still small enough to guarantee the validity of the Zeldovich approximation.

The finalized IC is then run from $z = 60$ to test the impact of the new kinetic AGN feedback models implemented into GADGET-3 on the single galaxy cluster. The cosmological parameters stay the same as they were used for the parent simulation. The properties of the selected galaxy cluster are listed in Tab. 3.1.

$M_{DM,tot}$ $10^{15} M_{\odot} h^{-1}$	M_{DM} $10^{8} M_{\odot} h^{-1}$	M_{Gas} $10^{8} M_{\odot} h^{-1}$	$Number_{DM}$	$Number_{Gas}$
2.57	8.43	1.56	3.046.818	2.319.183

Table 3.1

It is certain, that the resolution in our simulations cannot represent the full complexity of AGN feedback processes in detail. Smaller spatial scales would be required to obtain an accurate description of the impact of SMBH growth and feedback on galactic scales. The simulations which are analyzed in this study are listed in Tab. 3.2, together with the AGN feedback parameters. The parameter f_{kin}

Simulation ID	f_{kin}	ϵ_{kin}	ϵ_f	ϵ_r	v_{Wind} [km/s]	Wake-Up
Fiducial	0	Variable	0.05	Variable	-	-
KF000	0	Variable	0.05	Variable	-	3
KF005	0.05	Variable	0.05	Variable	10^4	4.1
KF050	0.5	Variable	0.05	Variable	10^4	4.1
KF100	1	Variable	0.05	Variable	10^4	4.1
KF100v5e3	5	Variable	0.05	Variable	5×10^3	4.1
KF100v2e4	5	Variable	0.05	Variable	2×10^4	4.1
KF500	5	Variable	0.05	Variable	10^4	4.1

Table 3.2: General AGN feedback settings of the simulations performed in this study. Variable values of are calculated with equations (19) and (20).

determines the energy which is made available for the kinetic AGN feedback (see equ 3.20). The values for ϵ_{kin} and ϵ_r are calculated on the run and determine the kinetic and radiative feedback efficiencies. The percentage of the radiative energy that couples with the gas is set by ϵ_f.The velocity increment a gas particle receives during the kinetic AGN feedback is fixed throught v_{Wind}. The last column of Tab.

3.2 the parameter for the Wake-up call routine which is explained in detail in App. A.4.

3.3 STARS AND SUPERNOVAE

At $z = 60$, the beginning of our simulations, no stars are included and have yet to be formed

It is assumed that the dark matter and newly-formed star can be treated in the collisionless limit and hence evolve according to the collisionless Boltzmann equation (CBE)

$$\frac{\partial f}{\partial t} + \dot{\vec{x}}\nabla_x f + am\vec{g}\nabla_p f = 0 \tag{3.1}$$

where $\vec{g}$ is the peculiar acceleration and $f(\vec{x}, \vec{g}, t)$ is the distribution function. Star formation (SF) is implemented following the multiphase effective sub-resolution model by Springel and Hernquist [166]. This model accounts for the impact of sub-grid physics, by adopting a statistical formulation on scales that are resolved. Since cold molecular clouds (represented by cold gas particles) and stars cannot be resolved, their densities, ρ_{cc} and ρ_* respectively, represent averages over a small region of the ISM.

It is assumed that cold gas clouds form stars on a characteristic time-scale t_*, and that a mass fraction β of these stars are short-lived and instantly die as supernovae. This is described by

$$\frac{d\rho_*}{dt} = (1-\beta)\frac{\rho_{cc}}{t_*}. \tag{3.2}$$

Hence, if the time-scale t_* is long the SF is slower and if the cold cloud density is high, more stars will form. The SF therefore depletes the reservoir of cold gas clouds at a rate of $\frac{\rho_c}{t_*}$, which is returned as hot gas through SN at a rate of $\beta\frac{\rho_c}{t_*}$ (so as to counteract the cooling catastrophe). The parameter β can also be described as the mass fraction of massive stars ($> 8M_\odot$) formed for each initial population of stars and hence depends on the adopted stellar initial mass function.

Next to the output of metal enriched hot gas, supernovae also release energy. The amount of energy feedback depends on the IMF, and is calculated as

$$\frac{d}{dt}(\rho_h u_h)|_{SN} = \epsilon_{SN}\frac{d\rho_*}{dt} = \beta u_{SN}\frac{d\rho_*}{dt}, \tag{3.3}$$

where ϵ_{SN} is the expected average energy returned by a SN ($= 4 \times 10^{48}\, ergs\, M_\odot$), and $u_{SN} \equiv (1-\beta)\beta^{-1}\epsilon_{SN}$ can be expressed in terms of an equivalent 'supernova temperature' $T_{SN} = 2\mu u_{SN}/(3k) \simeq 10^8\, K$.

Star formation is strictly confined to the regions where $\rho > \rho_{th}$. The density threshold ρ_{th} is calculated on-the-run according to

$$\rho_{th} = \frac{x_{th}}{(1-x_{th})^2}\frac{\beta u_{usn} - (1-\beta)u_c}{t_*^0\Lambda(u_{usn}/A_0)}, \tag{3.4}$$

where t_*^0 and A_0 are parameters that regulate the multi-phase medium due to SF. In the simulations studied here these parameters are set to $t_*^0 = 1.5$ and $A_0 = 1000$.

Λ is the cooling rate. The temperature threshold T_{th} below which a gas particle need to be to form a star is $5 \times 10^5\,K$. Gas particles which fulfill these two criteria, do not have to spawn into a star immediately. Star formation is based on the stochastic scheme by Springel and Hernquist [166] and can be done on a single gas particle up to four times.
Furthermore is the metal content of gas and stellar components determined. This accounts for, whether a star generates a Type II or Type Ia supernova (SN) and how long the SN lifetimes are.
The SPH technique uses sink-particles Bate, Bonnell, and Price[9] to follow the formation of stars and any continuing gas accretion on to them by adding the mass (and linear/angular momentum) of accreted particles to that of the sink-particle. It is therefore straightforward to track the evolution of the gas before it was accreted. In this way, one can determine the physical properties of the gas that formed a given star at all stages before it is accreted.
Since the internal evolution of the protostars is not of interest in determining where material from the cloud ends up, a protostar is replaced by a single, non-gaseous, massive particle with the combined mass, linear momentum and 'spin' of the particles it replaces. This massive particle then accretes any infalling gas particles and avoids the problem of high-density regions controlling the time required for the simulation. The spin is the angular momentum of the replaced particles about their centre of mass and is kept as a check that global angular momentum is being conserved, although it has no effect on the dynamics of the calculation.

3.4 BLACK HOLES

There exists a number of studies discussing large cosmological simulations that include BHs (e.g. Di Matteo, Springel, and Hernquist [53]; Robertson et al. [145]; Di Matteo et al. [54]; Booth and Schaye [24]; Schaye et al. [152]). The most common BH model used in those simulations derives from the model implemented by Springel, Di Matteo, and Hernquist [164]. This model describes BHs as sink particles which have fundamental properties like mass and accretion rate, which can be linked directly to observables. Thus, one can study BH growth and the co-evolution between BHs and their host galaxies to constrain and improve the parametrization of the underlying model.
In the following subsections, BH-seeding, -accretion and -feedback modes are explained in detail.

3.4.1 *Black Hole Creation*

In the universe we live in, BHs are currently thought to exist in four major subgroups with respect to thair mass range. Mirco BHs (MBH) encompass the most light-weight BHs with masses down to $10^{-8}\,M_\odot$, but can also create BHs with masses equivalent to the moon. MBHs are as of yet a hypothetical and thought to have formed in the very early universe (less than one second after the Big-Bang) due density fluctuations with a density contrast of $\delta\rho/\rho \sim 0.1$ (Harada, Yoo, and

Kohri [88]). However, since we only begin to find observational constrains on this type of BH and we can't resolve them with current simulation, they are neglect them in our simulations. The best studied type are the stellar BHs, which can have masses from five up to several tens of solar masses. However, a subresolution model with BHs linked to stellar evolution in star particles is not so easy to implement. Forming a very low mass BH particle from a star particle would increase by a huge amount the particles to follow and the computation time. Within cosmological (or galaxy-sized) numerical simulations, it is presently not feasible to follow the physics of star formation and black hole accretion from first principles down to scales of individual stars or black holes. Any numerical model of galaxy formation therefore needs to make substantial approximations for some of the relevant physics on unresolved scales (Di Matteo et al. [54]). Intermediate-mass BHs (IMBH) with masses in the order of $\sim 10^2 - 10^4\ M_\odot$, are thought to reside in dense stellar systems (Maccarone et al. [116]). However, evidence has been hard to come by, with roughly a half-dozen candidates described so far, and their formation process is therefore unknown, which is why together with the resolution-limit of our simulations we omit them. With masses ranging between $\sim 10^5 - 10^{10}\ M_\odot$, supermassive BHs (SMBH) form the higher end of BH masses and is found in the centre of galaxies. Together with SBHs they are the most studied BHs. Since their properties are constrained through multiple relations to their host galaxy and their possible masses can be resolved with our simulaions, we can effectively study them. Since this kind of BH is the only kind in the herein discussed simulations, they will be referred to as SMBH accordingly.
To create SMBHs, a *Friend of Friends* algorithm is deployed to identify dark matter subhalos. When the mass of a FoF group is above $10^{10}\ M_\odot$, a BH of $4.4 \times 10^5\ M_\odot$ is seeded at the potential minimum. Therefore, all our BHs in our simulations are mimicking a SMBH in the center of a halo from the beginning. In Fig. 3.4, shows the growth of BHs in our fiducial simulation. It shows how our BHs have a seeding mass which is lower than the observed relation (e.g McConnell and Ma [121]) between BH and stellar bulge mass (M_{BU}) of a galaxy.

$$log_{10}(M_\bullet/M_\odot) = 8.46 + 1.05 log_{10}(M_\star/10^{11} M_\odot)\,. \tag{3.5}$$

The reason is that in the simulations a galaxy evolves without a black hole until it is seeded. In reality, the black holes do not appear immediately. Thus, they have already accreted matter and influenced the surrounding medium. This can be compensated with a low seeding mass. After the seeding, a black hole grows until it reaches the $M_{BH} - M_{BU}$-relation.
To compensate the fact that a black hole is too light during this process, it has two masses: the real mass and the dynamical mass. The real mass is used for the accretion process, whereas the dynamical mass is used to calculate the gravitational forces as long as it is larger than the real mass.
The black holes are treated as collision-less sink particles like in other hydrodynamical simulations including black holes (e.g. Springel et al. 2005 or Di Matteo et al. 2008). BHs are repositioned in the potential minimum of their host galaxy once they are seeded, to keep them centered.

3.4.2 *Black Hole Growth*

The BH seeding mass of our simulation is $10^5\,M_\odot$, whereas SMBHs in the local Universe have masses of up to $10^9\,M_\odot$. To understand the origin of the redshift zero SMBHs population, one needs to model how BHs can grow to the sizes observed in present-day galaxies. In our simulations, BHs can grow by either accreting gas or by merging with other BHs.

The exact properties of accretion flow around BHs cannot be resolved in current numerical simulations. To elucidate this, consider a BH of mass M_{BH} accreting spherically from a stationary, uniform distribution of gas whose sound speed at infinity is c_∞. The gravitational radius of influence of the BH is then

$$r_B = \frac{GM_{BH}}{c_\infty^2}\,. \tag{3.6}$$

For a BH of mass $M_{BH} = 10^7\,M_\odot$, as are most BHs in our simulations at $z = 0$, in a gas with a sound speed $c_\infty = 30\,km\,s^{-1}$, this is numerically

$$r_B = 50pc\,(\frac{M_{BH}}{10^7\,M_\odot})(\frac{c_\infty}{30\,km\,s^{-1}})^{-2}\,. \tag{3.7}$$

The Schwarzschild radius of a BH of this mass is then

$$r_s \equiv \frac{2GM_{BH}}{c^2} = 10^{-6}pc(\frac{M_{BH}}{10^7\,M_\odot})\,. \tag{3.8}$$

Due to our poor understanding of the nature of accretion onto SMBHs, it is not clear what range in spatial scales would be required to obtain an accurate description of the impact of BH growth and feedback on galactic scales. It is certain however, that the resolution in our simulations cannot represent the full complexity of this process in any detail.
Therefore the accretion has to be approximated, which is often done using the Bondi parametrization (Bondi [22]), which was introduced in Sec. 2.3. Since this model assumes an isotropic and isothermal sphere of gas, it is not straightforward to adopt this Bondi accretion model for hydrodynamic, cosmological simulations aiming to follow a self-consistent accretion history of BHs.
Our simulations adopt the BH accretion model as implemented by Springel, Di Matteo, and Hernquist [164], where the accretion rate of the BH is estimated by

$$\dot{M}_B = \frac{4\pi\alpha G^2 M_\bullet^2 \langle\rho\rangle}{(\langle u\rangle^2 + \langle c_s\rangle^2)^{3/2}}\,. \tag{3.9}$$

The density $\langle\rho\rangle$, velocity $\langle u\rangle$, and sound speed $\langle c_s\rangle$ are computed using a sixth-order Wendland C^4 kernel function (Dehnen and Aly [49]) with 200 neighbours. The functional form of the interpolating function reads:

$$w(q) = \frac{495}{32\pi}(1-q)^6(1+6q+\frac{35}{3}q^2)\,. \tag{3.10}$$

Here, $q = x_{ij}/h_i$ is the ratio of the module of the distance between two particles $x_{ij} =\mid \mathbf{x}_i - \mathbf{x}_j \mid$ and the smoothing length h_i assigned to the position of the i-th particle. The use of this kernel function is motivated by it's avoidance of pairing instabilities and a gain in accuracy in quantity estimates over e.g. the standard cubic spline is achieved.

Due to limited numerical resolution in cosmological simulations, Springel, Di Matteo, and Hernquist [164] multiplied the original equ. 2.12 by a dimensionless boost factor α. Through the boost factor, the accretion of hot ($\alpha = 10$) and cold gas ($\alpha = 100$) becomes distinguishable. The choice of the α's derive from Gaspari, Ruszkowski, and Oh [81], who found that cooling and turbulence lead to a approximately 100 times larger accretion rate than the Bondi accretion. But for adiabatic accretion, the difference is about one order of magnitude smaller. Furthermore, Gaspari, Ruszkowski, and Oh [81] considered gas as hot if it has a temperature above $T \approx 10^6\ K$, whereas cold gas has a temperature below $T \approx 10^5\ K$. Since a third warm phase is not taken into account, $T = 5 \times 10^5\ K$ is chosen as threshold between hot and cold gas.

The BH accretion rate $\dot{M}_{BH}$ is limited to the Eddington accretion rate

$$\dot{M}_{Edd} = \frac{4\pi G M_{BH} m_p}{\eta_{Edd} \sigma_T c}, \tag{3.11}$$

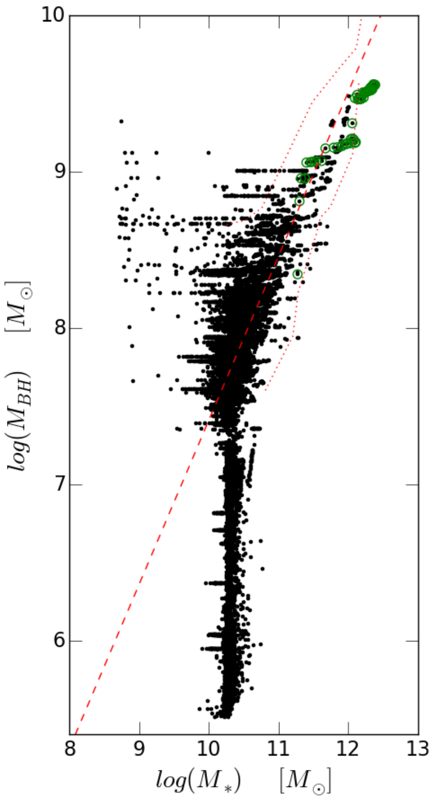

Figure 3.4: Margorrian relation of the fiducial simulation in which the green circles indicated the BCG. SMBH outliers are due to temporary attributions to different subhalos.

where m_p is the proton mass, σ_T the Thompson scattering cross-section, and η_{Edd} the feedback efficiency if the BH would accrete with $\dot{M}_{Edd}$. In our simulations η_{Edd} is dependent on M_{BH}, as was found by Davis and Laor [48],

$$\eta_{Edd} = 0.089 \left(\frac{M_{BH}}{10^8 M_\odot} \right)^{0.52}, \tag{3.12}$$

but limited by the value 0.42, which is the theoretical maximum efficiency of a rotating BH. In duing so, one can account for the observed spin of SMBHs.

The final accretion rate is given by

$$\dot{M}_{BH} = min(\dot{M}_{B,hot} + \dot{M}_{B,cold}, \dot{M}_{Edd}). \tag{3.13}$$

The separate treatment of hot and cold gas leads to a faster BH growth in the quasar-mode, because when calculating the mean value of the sound speed $\langle c_s \rangle$

and gas velocity $\langle u \rangle$ only for cold gas, the accretion rate estimated with equation 3.9 is higher than calculating the mean values of both cold and hot gas together. Depending on $\dot{M}_{BH}$, a certain amount of gas particles will be swallowed by the BH in a time step Δt. Whether or not a gas particle will be accreted depends on the probability

$$P_i = \frac{\omega_k (M_{BH} - M_{Gas}) \Delta t}{\rho} \, . \tag{3.14}$$

described in appendix This probability is then compared to a random number $\omega_i \in [0, 1]$. If $\omega_i < P_i$, the gas particle will be swallowed.

Finally, formation of 'heavy' BHs from the mergers of lower-mass BHs in globular clusters is unlikely because most dynamically formed merging BHs are ejected from the host cluster before merger (Rodriguez et al. [146], see their Figure 2). In the case of BH binary mergers, the original implementation by Springel, Di Matteo, and Hernquist [164] force BHs to remain within the host galaxy by pinning them to the position of the particle found having the minimum value of the potential among all the particles lying within the SPH smoothing length computed at the BH position. This 'pinning' can lead to BHs 'jumping' from the less massive galaxy to the more massive one during merger events. To avoid that the BH particles are wandering away from the centre of galaxies by numerical effects, our simulations use momentum conservation and place the resulting BH from a merger event in the centre of mass of the predecessor. Only when any two BHs pass within a distance h_{BH} of each other with a relative velocity smaller than the local sound speed, are they allowed to merge. The smoothing length h_{BH} is taken from the more massive BH and is determined in every time step by implicit solution of the equation,

$$\frac{4}{3} \pi h_{BH}^3 \rho_{BH} = M_{ngb} \, . \tag{3.15}$$

Here ρ_{BH} is the kernel estimate of the gas density at the position of the BH, and M_{ngb} is the mass of $\sim 4 \times 64$ neighbouring gas particles. The BH particle has 4 times more neighbours (e.g. Fabjan et al. [69]) than an SPH gas particle, order to have more particles for computing the physical properties of the BH subresolution model.
The simulation takes care, that only the more massive BH swallows the lighter one.
This velocity criterion is necessary in order to prevent BHs from merging during a fly-through encounter of two galaxies, as this could lead to BHs being quickly removed from their host galaxies due to momentum conservation.

3.4.3 *Black Hole Feedback*

An important consequence of gas accretion onto a BH is the release a huge amount of energy, which strongly influences the formation and cosmological evolution of galaxy clusters. So far, only few simulations include a detailed AGN

feedback models for galaxy cluster simulations. Most are implemented on galactic scales or as pure thermal feedback in galaxy clusters. Choi et al. [32], [33], [34] studied mechanical AGN feedback (in thermal & kinetic form) in isolated and merging galaxies. Steinborn et al. [171] and Rasia et al. [141] studied high resolution galaxy clusters with radiative and mechanical AGN feedback implemented as thermal feedback. Weinberger et al. [189], [188] studied cosmological box of $30Mpch^{-1}$ with AGN feedback in thermal and kinetic form.
As outlined in Sec. 2.4, there exist two major AGN feedback modes: radiative and mechanical. In this study, simulations account for both AGN feedback modes by adopting the scheme based on Churazov et al. [36] and Steinborn et al. [171]. Churazov's model is confirmed observationally (e.g. Russell et al. [147]) through measuring luminosities and cavity powers of a large sample of unresolved nuclear X-ray sources.

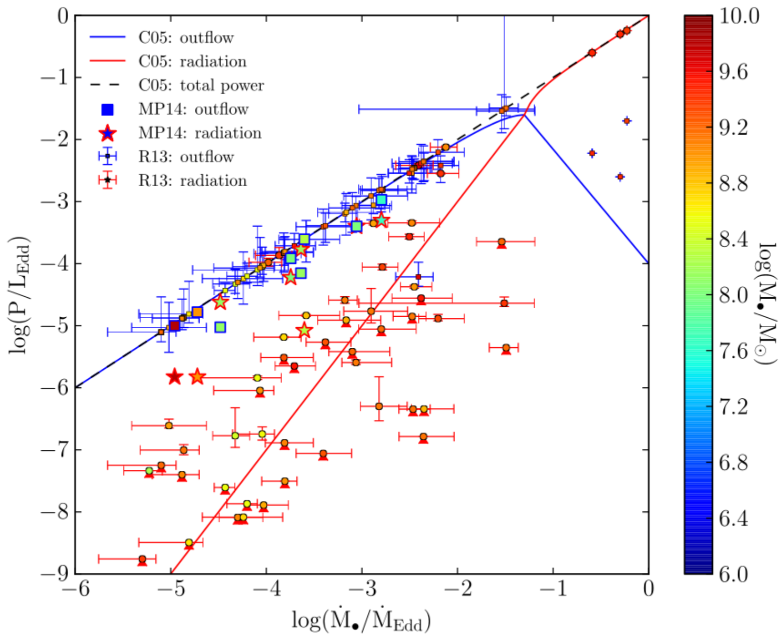

Figure 3.5: The lines show the predictions by Churazov et al. [36] for the power of the radiation (red line), the mechanical outflow (blue line) and the sum of both (black dashed line). Observations of jet powers (blue error bars and edges) and luminosities (red error bars and edges) constrain the difference between both components.
Graphic from Steinborn et al. [171].

The herein studied BH model calculates the feedback energy per unit time as the sum of kinetic (P_m) and thermal ($\epsilon_f L_r$) feedback:

$$\dot{E} = E_m + E_r = (\epsilon_m + \epsilon_f \epsilon_r)\dot{M}_\bullet c^2. \tag{3.16}$$

The radiative component dominates near the Eddington limit ($f_{Edd} > 0.1$) as can be seen in Fig. 3.5. The radiative AGN energy equals,

$$L = \epsilon_r \dot{M}_{BH} c^2, \tag{3.17}$$

with ϵ_r being the radiative efficiency which is calculated during the simulation run. To account for the observed transition between the two feedback modes, $\dot{M}_{BH}/\dot{M}_{Edd} = 0.05$ is taken as the threshold. Accretion below this value become dominated by the radio-mode, and above by the quasar-mode. This leads to an radiative efficiency of the form

$$\epsilon_r = \begin{cases} A\eta_{Edd}(M_{BH})(\frac{\dot{M}_{BH}}{\dot{M}_{Edd}})^{\beta} & \text{if } \frac{\dot{M}_{BH}}{\dot{M}_{Edd}} < 0.05\,, \\ \eta_{Edd}(M_{BH} - 10^{-4}\eta_{Edd}(\frac{\dot{M}_{BH}}{\dot{M}_{Edd}})^{-2.8431} & \text{otherwise.} \end{cases} \tag{3.18}$$

, where β is the slope which defines the correlation between accretion rate and energy feedback. In all our simulations $\beta = 0.5$ was used.
A fraction ϵ_f of the luminosity L is eventually fed back to the neighbouring gas as thermal feedback:

$$E_r = \epsilon_f L = \epsilon_f \epsilon_r \dot{M}_{BH} c^2\,. \tag{3.19}$$

From previous GADGET-2 simulations, $\epsilon_f = 0.05$ yielded an $M_{BH} - \sigma$ relation normalization consistent with observations Di Matteo, Springel, and Hernquist [53]. The radiative feedback is distributed to the gas isotropically around the SMBH. The temperature of the neighbouring gas particles are incremented by an amount scaled by their SPH kernel weights.

The mechanical component dominates at accretion rates $f_{Edd} < 0.01$ and diminished at rates $f_{Edd} > 0.1$. The available energy per unit time that can be fed back in kinetic form is calculated as

$$E_{avail,kin} = \dot{M}_{BH} f_{kin} \epsilon_r c^2, \tag{3.20}$$

which is different to the model by Steinborn et al. [171]. The outflow efficiency ϵ_{kin} depends on the accretion rate and mode, just as ϵ_r does:

$$\epsilon_m = \begin{cases} 0.1 - A0.1(\frac{\dot{M}_{BH}}{\dot{M}_{Edd}})^{\beta} & \text{if } \frac{\dot{M}_{BH}}{\dot{M}_{Edd}} < 0.05\,, \\ 10^{-5}(\frac{\dot{M}_{BH}}{\dot{M}_{Edd}})^{-2.8431} & \text{otherwise.} \end{cases} \tag{3.21}$$

In contrast to ϵ_r it is currently difficult to estimate ϵ_{kin} with observations, which is why $\eta_{Edd} = 0.1$ was assumed in this case. $E_{avail,kin}$ is then set equal to the energy of total mass of gas particles which can be kinetically exited:

$$E_{Wind} = \frac{1}{2}\dot{M}_{Wind} v_{Wind}^2\,, \tag{3.22}$$

so that dependency between $\dot{M}_{Wind}$ and $\dot{M}_{BH}$ becomes

$$\dot{M}_{Wind} = 2\dot{M}_{BH} f_{kin} \epsilon_{kin} \left(\frac{c}{v_{Wind}}\right)^2\,. \tag{3.23}$$

The kinetic AGN feedback energy is distributed to gas lying inside a bi-conical volume, with the SMBH at its apex and two cones on opposite sides of the BH (as described in Barai et al. [7]), which is schematically shown in Fig. 3.6.

The slant height of each cone is h_{BH}, and the total opening angle of a single cone is 60°. The cone axis directions are considered as fixed along the $\pm z - axis$ for the first duty cycle and change randomly thereafter, for the BH located at the origin of our coordinate system. The gas particles lying within this bi-cone volume around the BH are tracked, and their total mass M_{gas}^{cone} is computed.

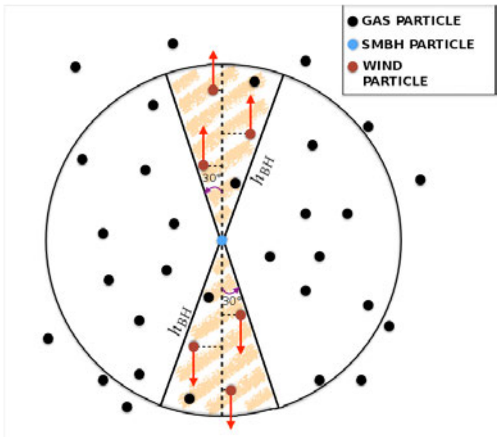

Figure 3.6: Schematic representation of kinetic AGN feedback mechanism.

The feedback energy is distributed to gas within a distance h_{BH} from the SMBH. Gas particles inside the bi-cone are stochastically selected and kicked into AGN wind, by imparting a one-time v_{Wind} velocity boost. We use a probabilistic criterion (similar to other sub-resolution prescriptions in GADGET-3) for the implementation. A probability for being kicked is calculated depending on whether the ith gas particle is in the upper or lower cone at timestep ∂t:

$$p_i = 2\dot{M}_{Wind} \frac{\dot{M}_{gas}^{cone-up,-down} \partial t}{(\dot{M}_{gas}^{cone-up} + \dot{M}_{gas}^{cone-down})^2} \, . \tag{3.24}$$

At a given timestep, all the gas particles within the bi-cone have the same probability to be ejected. A random number x_i, uniformly distributed in the interval $[0, 1]$, is drawn and compared with p_i. For $x_i < p_i$, the particle is given a wind velocity kick.

The inverse proportionality of p_i with $\dot{M}_{gas}^{cone}$ ensures that the number of particles kicked does not depend on the geometry of the volume, but depends on $\dot{M}_{Wind}$ only. The quantity $\dot{M}_{Wind}\partial t$ is the mass of gas to be kicked. The probability is constructed such that the available particles (total mass $\dot{M}_{gas}^{cone}$ within bi-cone) are sampled to reproduce kicking at the rate given by $\dot{M}_{Wind}$, on average. During a simulation, it is always ensure that $p_i < 1$.

After receiving AGN wind kick, a gas particle's velocity becomes:

$$\vec{u}_{new} = \vec{u}_{old} \pm v_{Wind}\hat{z} \, , \tag{3.25}$$

where the $+$ or $-$ is chosen, depending on the location of the gas particle w.r.t. the SMBH. This approach is chosen for its numerical simplicity and has to be improved in future simulations.

4 RESULTS

4.1 SUPERMASSIVE BLACK HOLES

4.1.1 *Eddington-Ratio Evolution*

Figure 4.1 shows the redshift evolution of the Eddington-ratio, f_{edd}, distribution of all BHs in the simulations. The vertical bar with a grey gradient visualises the adopted smooth division between the radio- (diminishing when $f_{edd} > 0.05$) and quasar-mode (dominant above $f_{edd} > 0.05$) in the simulation code (as explained in Section 3.4.3). The simulated fraction of AGN which are accreting at small Eddington-ratios ($f_{edd} < 0.1$) increases visibly with decreasing redshift. The simulation confirm that the quasar-mode dominates at $z \sim 2 - 3$, as mentioned earlier in Sec. 2.4.1. This illustrates a downsizing trend, in which the SMBHs at later times mainly reside in a decline dominated 'blow-out' accretion phase. In addition it made visible, that the fiducial simulation (Fid.)is shifting to a lower f_{edd} earlier than the SMBHs in the other simulations. At $z = 0$ however, the f_{edd} distribution is almost equal for all simulations. This predicted BH accretion history is in qualitative agreement with several observational studies (Vestergaard [185]; Kollmeier et al. [112]; Kelly et al. [107]; Schulze and Wisotzki [155]; Steinhardt and Elvis [172]; Kelly and Shen [106]).

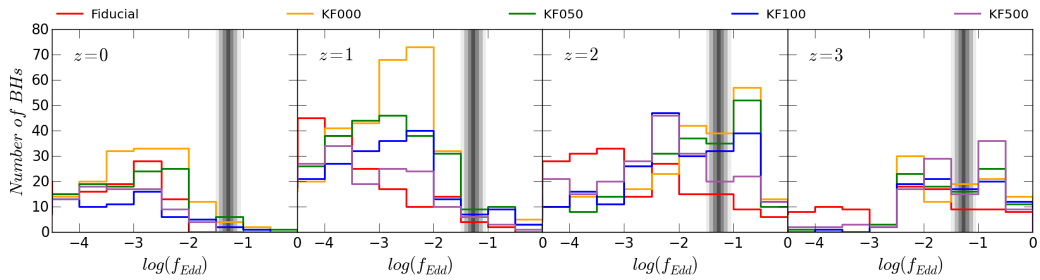

Figure 4.1: Eddington ratio distributions for different redshifts $z = 0, 1, 2, 3$. The vertical grey colour gradient visualises the smooth distinction between radio- and quasar-mode adopted in the model. A larger version is shown in Fig. B.1

Furthermore can be deduced from Fig. 4.1, that many SMBH mergers took place between $z = 1 - 2$ as a consequence of the growth of density fluctuations ($\delta \propto exp(Ht)$ for a dark energy-dominated era), leading to culmination of matter and hence SMBHs mergers, reducing the total number of SMBHs in the simulation.

How well the redshift evolutions of the simulated Eddington-ratios with observations agree is shown in Fig.4.2. Since the observational data set by Shen and Kelly [158] (black filled circles in the figure) includes only broad-line quasars with magnitudes above $M_i < -22$ (which equals a luminosity of $\approx 10^{44}\, erg\, s^{-1}$), only those SMBHs fulfilling this criterium are considered and averaged. In both simulations and observations, the Eddington-ratios are decreasing with decreasing redshift. The higher fluctuations at small redshifts originate from the higher snapshot number due to $log(a)$ spacing in time for comoving integration. Additionally, valuable information can be found when separating the AGN sample into different AGN luminosity bins (Fig. 4.3a) and different BH mass bins (Fig. 4.3b). Fig. 4.3a illustrates that on average for the entire redshift range since $z \sim 4$, the most luminous AGN (most left panel) accrete at the highest Eddington-ratios ($0.1 < log(f_{edd}) < -1.3$). This is simply due to that equation used to derive the AGN luminosity, as was discussed in 3.4.3. The highest f_{edd} for the mass bins are found for the lightest SMBHs in redshifts $z < 2$, since they haven't ejected much energy yet in their surrounding, quenching their own growth rate. The diagram of the most massive SMBHs starts at a lower redshift, since SMBHs have first to form through mergers. Interestingly, for the first three most luminous bins, the fiducial has a larger or equal f_{edd} than the other simulations, whereas for the first three most massive bins, it has a lower f_{edd}. This derives from the different kinetic AGN feedback models used. While the fiducial simulation uses the kinetic feedback thermally, the other impart a velocity on random gas particles, therefore they heat less the SMBHs environment and can accrete more. From Fig. 4.1 we know that at redshifts < 1 most SMBHs are in the radio-mode where the kinetic AGN feedback becomes dominant. Since the difference between the fiducial and the other simulations is mainly at redshifts > 1, one suspects a different feedback efficiency of the quasar-mode in the simulations. The simulated interplay between SMBH mass, luminosity and Eddington-ratio is in good qualitative agreement with the semi-analytic model by Hirschmann et al. [91]. This confirms that a con-

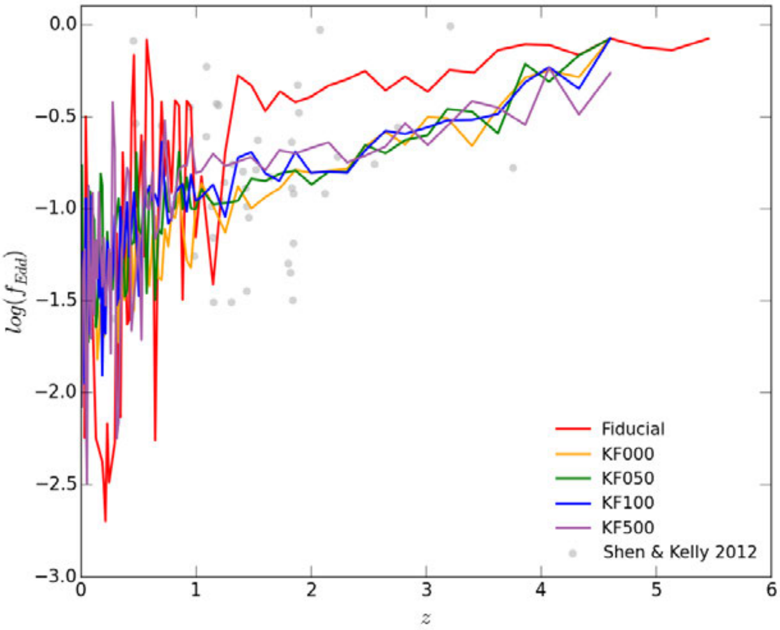

Figure 4.2: Redshift evolution of the mean Eddington ratios for SMBHs with $L_{bol} > 10^{44}\ erg\, s^{-1}$. The grey dots represent observational data by Shen and Kelly [158].

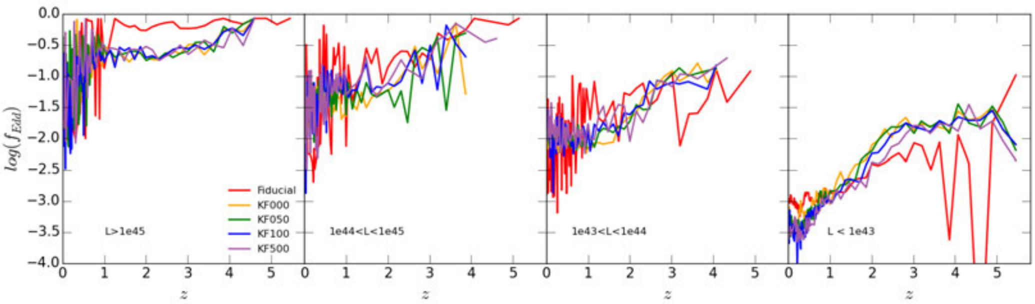

(a) Luminosity bins

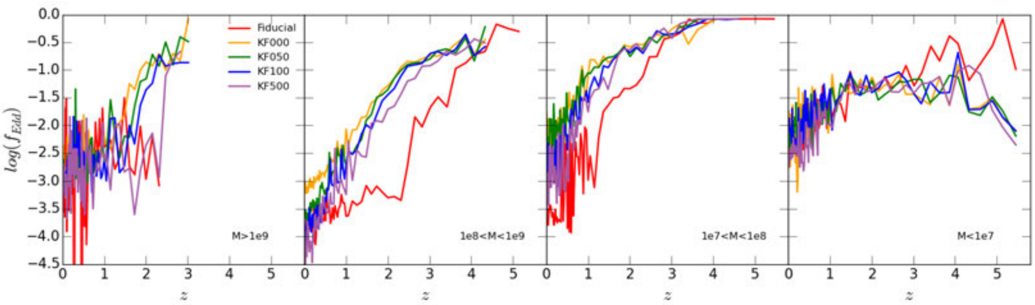

(b) Mass bins

Figure 4.3: Luminosity and mass binned redshift evolution of the mean Eddington-ratios. The upper Fig. shows the luminosity bins: $L > 10^{45}\ erg\, s^{-1}$ (left), $10^{44} < L < 10^{45}\ erg\, s^{-1}$ (2nd from left), $10^{44} < L < 10^{44}\ erg\, s^{-1}$ (2nd from left), and $L < 10^{43}\ erg\, s^{-1}$ (right). The lower Fig. shows the mass bins: $M > 10^{9}\ M_{\odot}$ (left), $10^{8} < M < 10^{9}\ M_{\odot}$ (2nd from left), $10^{7} < M < 10^{8}\ M_{\odot}$ (2nd from left), and $M < 10^{7}\ M_{\odot}$ (right).

nection between SMBH masses and AGN luminosities seems to be a necessary condition for reproducing a downsizing trend in SMBH growth.
In Fig. 4.1 the growth in total SMBH mass of the BCG is shown.

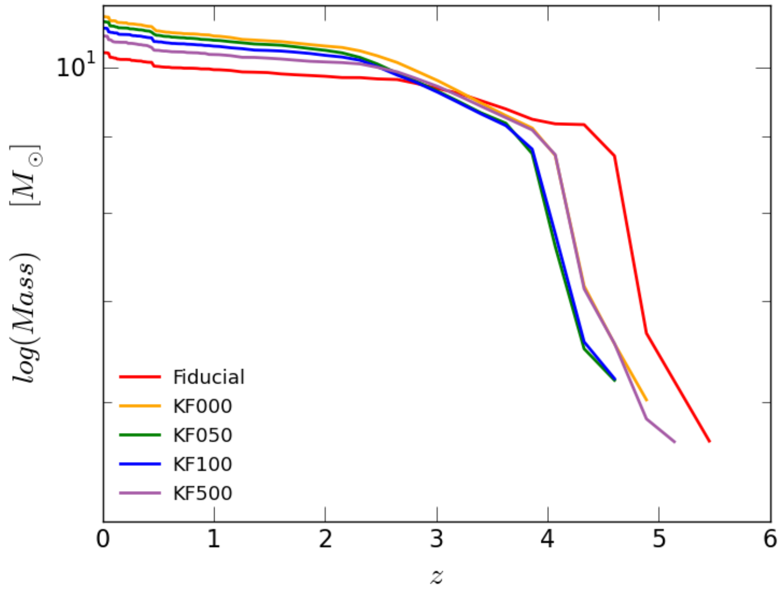

Figure 4.4: Redshift evolution of the total mass of SMBHs in a sphere with a radius of $2000\,kpc\,h^{-1}$ around the BCG.

4.1.2 *BH-Galaxy Mass Scaling Relations*

The fundamental relation between the central galactic SMBH mass M_{BH} and the stellar galactic bulge mass M_* (also called the Margorrian relation) is shown in Figure 4.5 for all subhalos in the simulated galaxy cluster at the last five snapshots. Since our simulations do not have a high enough resolution to provide sufficient morphological information of the galaxies, the stellar mass of the bulge is approximated by taking the total stellar mass. Hence, all our galaxies consist mainly of a spheroidal component. The dashed green lines in Fig. 4.5 indicate the observations of McConnell and Ma [121] and the dotted lines enclose the region containing the data.
As mentioned in Section 3.4.1, a SMBH with mass $M_{seed} = 4.4 \times 10^5\,M_\odot$ is placed into a halo whenever the on-the-fly *Friend of Friends* halo finder identifies a structure that is more massive than a threshold mass $M_{FoF} = 10^{10}\,M_\odot$ and does not yet contain a SMBH. At seeding, the surrounding gas is usually dilute and the SMBH accretes at low rates with a long Bondi growth time-scale. This means that the growth is slower than the growth in stellar mass and therefore, the corresponding galaxy evolves horizontally in the $M_{BH} - M_*$ diagram. This phase is not visible in Fig. 4.5 because of the resolution limitations. After some time, enough gas piles up around the SMBH and produces higher accretion rates, allowing the it to eventually grow more rapidly, aided also by the runaway character of Bondi growth due to its $\dot{M} \propto M_{BH}^2$ dependency (3.9). Consequently, the slope in the $M_{BH} - M_*$

diagram steepens. This steep increase in BH mass continues until the feedback injection of the BH into its surrounding becomes self-regulated. In this final stage, the SMBHs grow less rapidly and are mostly in the low accretion state, as indicated by the face-colour of the dots. Furthermore, the scatter along the $M_{BH} - M_{*}$ relation at higher masses decreases. This is most likely a consequence of statistical merging (e.g. Jahnke and Macciò [103]) and is also visibly in other simulation (e.g Hirschmann et al. [90]; Steinborn et al. [171]). Compared with the observational

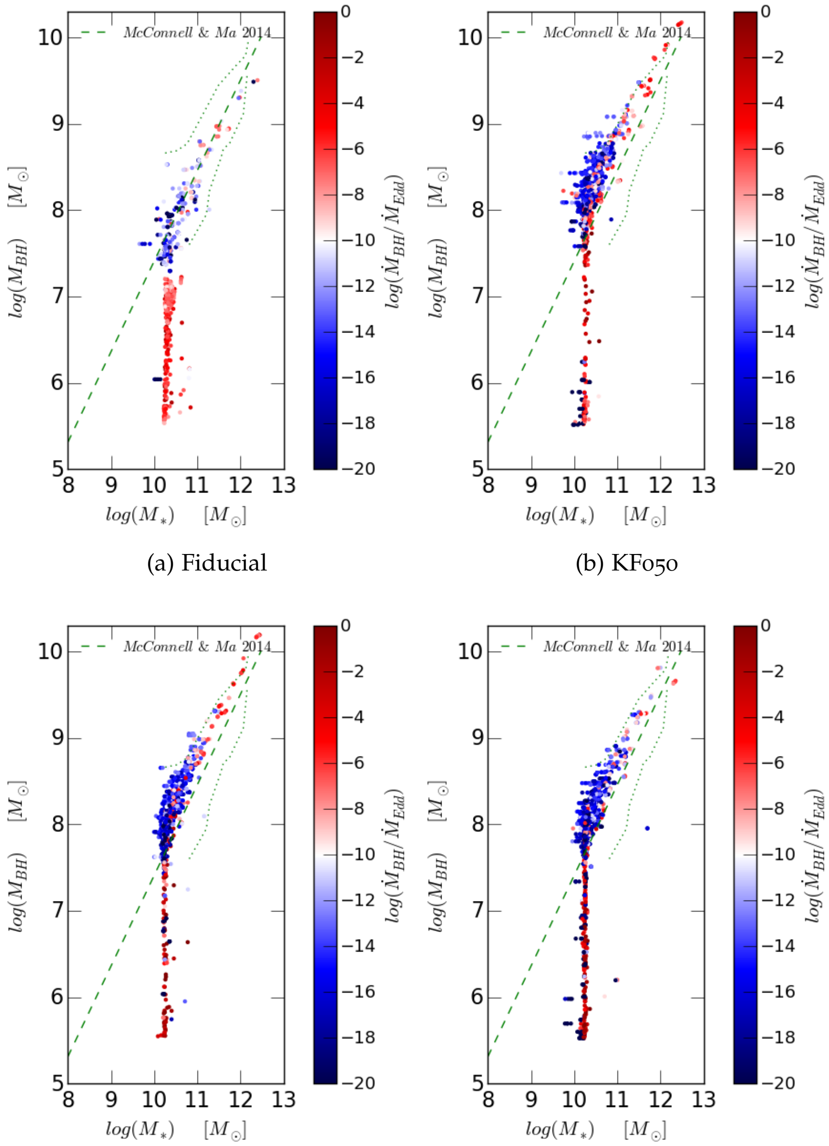

(a) Fiducial (b) KF050

(c) KF100 (d) KF500

Figure 4.5: Margorrian relation for the last five snapshots. The green dashed- and dotted-lines symbolize the best fit to the observations of McConnell and Ma [121] and their enclosed region containing the data respectively.

results, SMBHs in the simulation with the new kinetic feedback scheme implemented have slightly overly massive SMBHs, which indicates a too high accretion rate in the quasar-mode. This was already noticed and explained at Fig. 4.3b. Fig. 4.6 shows the best linear fit for SMBHs with $M_{BH} > 10^8$, which is the approximate mass at which the SMBHs in all simulations reach the Margorrian relation. Compared to the observations, the simulations Fiducial and KF500 can be considered to have the best agreement. This is a direct consequence of the choice of the feedback efficiency, which in counter-play to the cooling, sets the self regulated state of the late time evolution. The other simulation run almost parallel to the observed best-fit. Tab. 4.1 shows the best-fitting parameters a and b corresponding

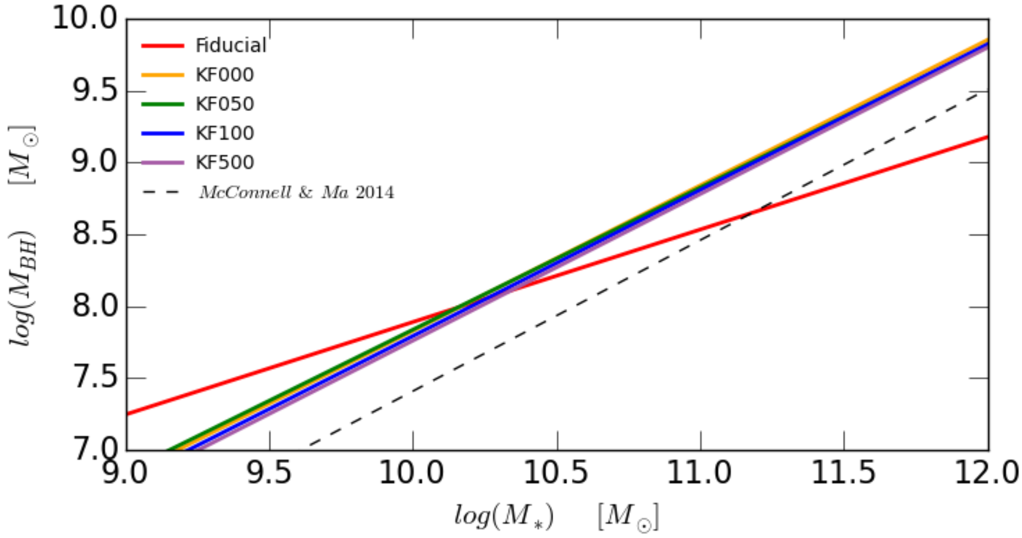

Figure 4.6: Comparison of the linear fit of simulated SMBHs and observations.

to the fit function $log(M_{BH}/M_\odot) = a + b \cdot log(M_*/10^{11}\ M_\odot)$ for all simulations. The slope of the $M_{BH} - M_*$ relation is relatively insensitive to the chosen value of ϵ_f [1], not however the normalization due to $M_{BH} \propto (\epsilon_f \epsilon_r)^{-1}$. Hence, many recent simulations which include BHs (e.g. Hirschmann et al. [93]) tuned these parameters in order to reproduce the normalization of the observed $M_{BH} - M_*$ relation. The reason for the different slopes in the simulations compared to observations comes from the fact, that ϵ_r is not a constant parameter in our AGN feedback model, but calculated for every time-step. Nevertheless, the relative role of AGN feedback and statistical merging in establishing the $M_{BH} - M_*$ relation and producing the observed slope still remains a matter of debate.

4.1.3 *M-sigma Relation*

Another fundamental correlation between SMBHs and their host galaxies are between the SMBH mass and the velocity dispersion of galaxy bulge, which was

1 The choice of ϵ_f depends on the resolution, because at lower resolutions the feedback energy is spread further away from the BH.

Simulation ID	a	b	σ
McConnell and Ma [121]	8.46 ± 0.08	1.05 ± 0.11	0.45
Fiducial	8.53	0.64	0.14
KF050	8.82	0.99	0.16
KF100	8.81	1.01	0.16
KF500	8.78	1.02	0.18

Table 4.1: Best-fitting parameters and standard deviation for our runs in comparison to the observations by McConnell and Ma [121]. All SMBHs with masses smaller than $M_{BH} > 10^8$ have been excluded to avoid seeding effects.

first found by Combes, Mamon, and Charmandaris [37] and Ferrarese and Merritt [72]. This relation usually takes the form of

$$\frac{M_{BH}}{M_\odot} = A\left(\frac{\sigma}{200\,km/s}\right)^\alpha, \tag{4.1}$$

where A is a constant, σ is the stellar velocity dispersion of the galaxy bulge, and α is a constant representing the slope of the $M_{BH} - \sigma_*$ relation.
For each SUBFIND-identified subhalo, the radius $R_{1/2}$ containing $1/2$ of the total stellar mass is found. All SMBHs and stars within this radius are considered to analyze this relation in the simulations.
To obtain the galactic stellar velocity dispersion σ_*, one hundred random line-of-sight (LOS) directions are chosen around the subhalo center. All stars lying within $R_{1/2}$ from the center are picked, and the LOS velocity v_{LOS} component of each is found. The stellar velocity dispersion along each LOS direction is computed by summing over all selected stars:

$$\sigma_* = (\langle v_{LOS}^2 \rangle - \langle v_{LOS} \rangle^2)^{1/2}. \tag{4.2}$$

This is repeated 100 times to obtain the median and standard deviations.
Fig. 4.7 shows the redshift evolution of $M_{BH} - \sigma_*$ relation for Fiducial, KF050, KF100, and KF500. The figure includes the observational results by Tremaine et al. [181]; Gültekin et al. [85]; Binney and Tremaine [18]; McConnell and Ma [121] as dashed-lines with the shaded region displaying the measurement error for the first two references. The observations all in good agreement with each other. The results of the simulations are shown as a scatter plot with a colour gradient indicating at which redshift the galaxies were analyzed. The solid lines with same colour are the mean of the scatter for each analyzed redshift. It appears that at high redshifts $z > 2.3$, σ_* is almost constant for the M_{BH}-range (especially for KF100 and KF500). As time progresses, a clear between M_{BH} and σ_* becomes visible, which likens the Margorrian relation. Albeit, when the SMBHs reach the relation they have a too high mass for their σ_* with respect to the observational study.
If the simulations are compared to the theoretically derived $M_{BH} - \sigma_*$ relation of elliptical galaxies close to the cluster centre by Zubovas and King [195], which were discussed in Sec. 2.4.1, a better agreement can be seen. Only the theoretical model for ellipticals is taken as comparison, since most galaxies in clusters

are ellipticals and it is very unlikely to find spiral galaxies in the here analyzed simulations. The simulations can be seen as supporting the theoretical model by Zubovas and King [195]. However this relation has to be better analyzed in higher resolution cluster simulations. It must also be mentioned, that the observational

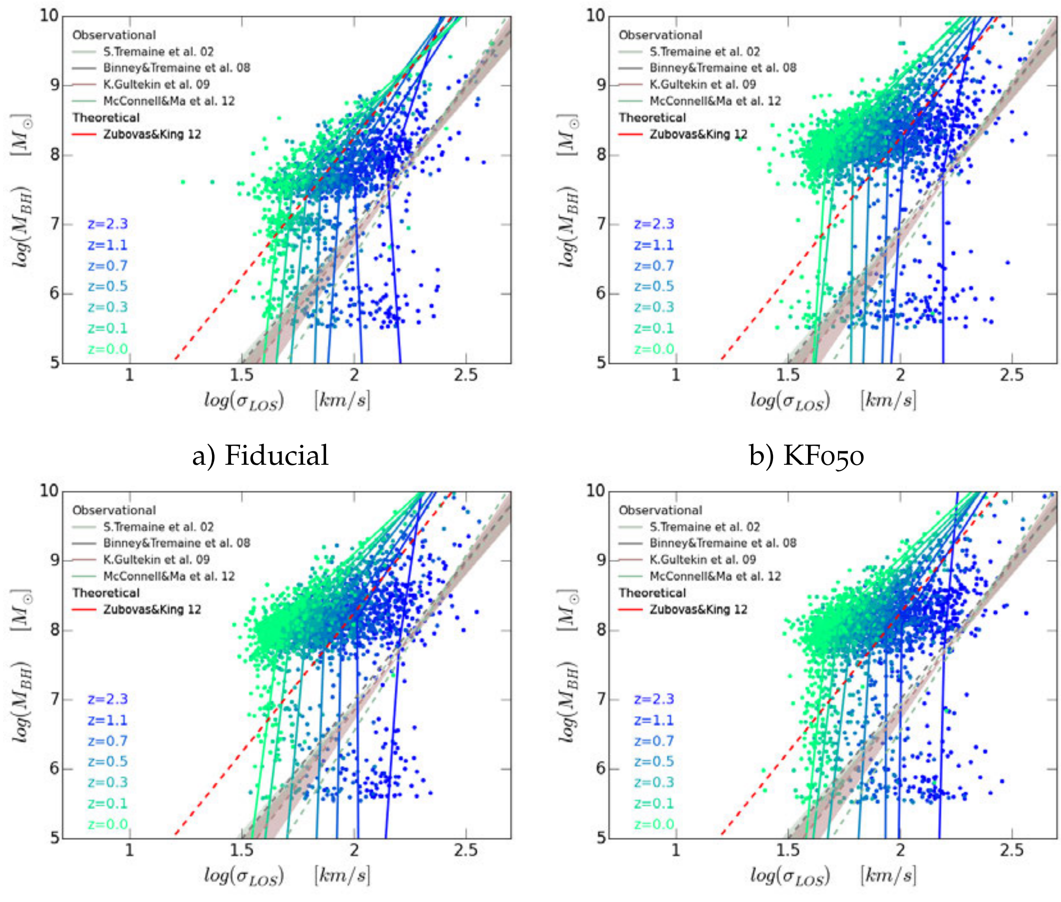

a) Fiducial b) KF050

c) KF100 d) KF500

Figure 4.7: Redshift evolution of the fundamental $M_{BH} - \sigma_*$ relation for redshifts $z = 2.3, 1.1, 0.7, 0.5, 0.3, 0.1, 0$ for the simulations: Fiducial (top-left), KF050 (top-right), KF100 (bottom-left), KF500 (bottom-right).

trends are often derived from data sets that do not make a distinction between ellipticals and spirals, or the galaxy environment (inside a cluster or in the field). McConnell and Ma [121] made distinctions between spiral and ellipticals, not however of the environment. Thus, Fig. 4.7 shows the slope for ellipticals of the data set McConnell and Ma [121] used.) Since spiral galaxies have a lower velocity dispersion than elliptical galaxies, it will lower the general trend and bring it further apart from the results of the galaxies inside the simulated cluster.
Fig. 4.8 shows the resulting diagram obtained from the simulations for $z = 0$. The median σ_* is depicted by the plotting symbol and the same coloured lines their linear fit. The same observational derived relations come from the same publications as the ones use for Fig. 4.7 and the same colouring is used.

The tight relation could also be used to tune the feedback model, however most groups focus on the ratio between black hole mass and stellar/bulge mass.

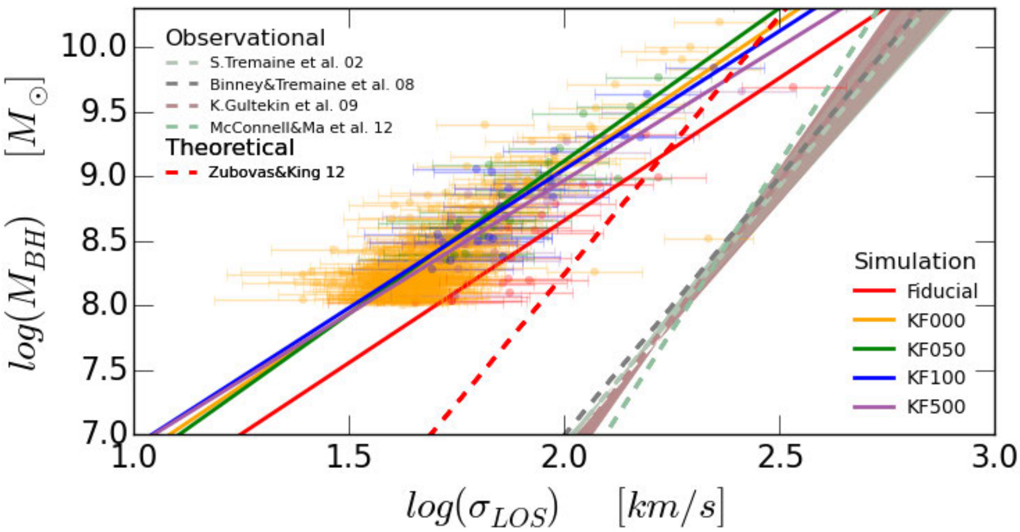

Figure 4.8: Redshift evolution of the fundamental $M_{BH} - \sigma_*$ relation for redshifts $z = 0$. The line elements of the simulations show the best fit to the scatter of the median, which is shown with the errorbars of the 70th percentiles around the median.

4.1.4 *Bivariate Distribution Function*

In this section the SMBH distribution of the low resolution simulations in the $M_{BH} - f_{Edd}$ plane is put into juxtaposition with the observational derived bivariate distribution function composed of the black hole mass function (BHMF) and the Eddington ratio distribution function (ERDF) (Schulze et al. [154]). Observational data of Type-I AGNs from three optical surveys (VVDS, zCOSMOS and SDSS) was utilized and the BHMF and ERDF were calculated using modified Schechter functions. The bivariate distribution function is then taken as a composition:

$$\Psi(M_{BH}, f_{Edd}) = \phi_{f_{Edd}}(f_{Edd}, M_{BH})\phi_{M_{BH}}(M_{BH})\,. \tag{4.3}$$

Since the distribution functions of Schulze et al. [154] were obtained in intervals of $-2 < log(f_{Edd}) < 1$ and $7 < log(M_{BH}) < 11$, the SMBHs of the simulations were selected accordingly. To obtain a best fit of the modified Schechter functions to the data, a maximum likelihood approach was used over the full redshift range $1.1 < z < 2.1$. The cosmological sample of simulated SMBHs is too small for a

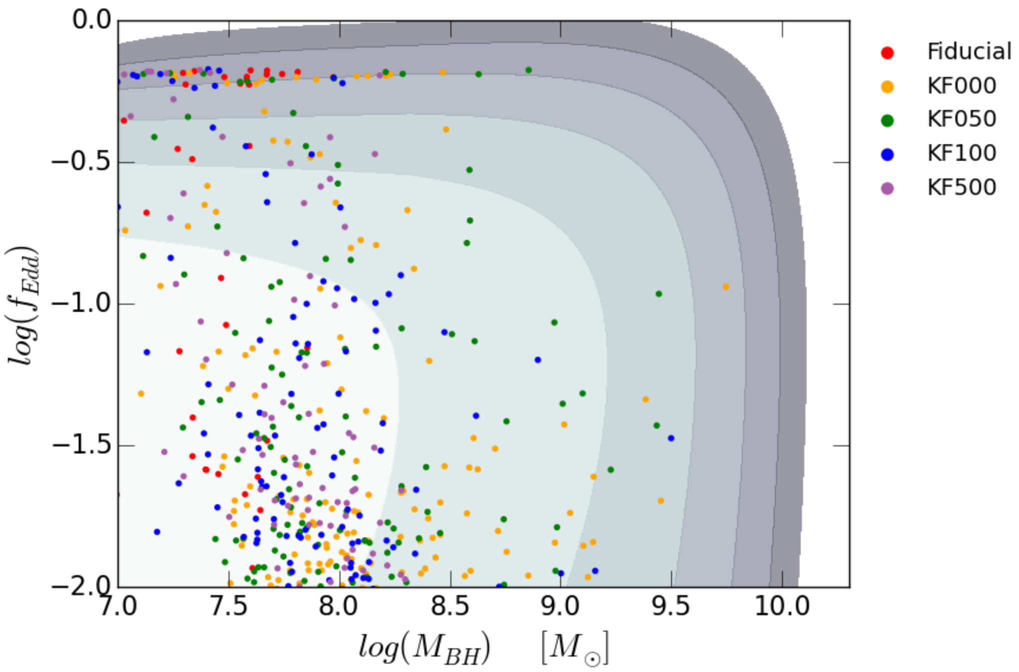

Figure 4.9: Bivariate distribution function of SMBH mass and Eddington ratio $\Psi(M_{BH}, f_{Edd})$ for our best-fitting modified Schechter function BHMF model at two redshifts. The contours show lines of constant space density, from 10^{-10} to 10^{-5} , separated by a factor of 10 each.

qualitative comparison between observed and simulated distribution functions. However, it still serves as an illustration of the diversity in the AGN population and a sanity check. One can see that KF000 and KF050 tend to have too high SMBH masses, and that all simulations produce too many SMBHs with high Eddington ratios ($f_{Edd} > -0.25$). The latter can be explained by the fact, that the simulation only focus on a galaxy cluster, where SMBHs tend to have more gas which can be accreted. The surveys also cover galaxies which are in voids or filaments, which contain less baryons, and therefore less accretion matter for the SMBHs.

4.2 STARS

4.2.1 *Star Formation Rate*

A parameter study of v_w and f_{kin} with respect to the total SFR for simulation runs is shown in Fig. 4.10 and Fig. 4.11 respectively. By comparing the simulations which use the same feedback model but different kinetic feedback velocities, it becomes clear that changing this parameter has no impact on the star formation rate. The fact that the kinetic feedback model imparts a velocity kick on gas particles seems to be of bigger importance than the magnitude of the velocity itself. Comparison of other properties between simulations the fiducial run and simulations with varying wind velocity are shown in App. B.4. Since there is little difference between those runs, the wind velocity parameter has not been studied further and a closer look on the effect of f_{kin} was taken. In Fig. 4.11, four different

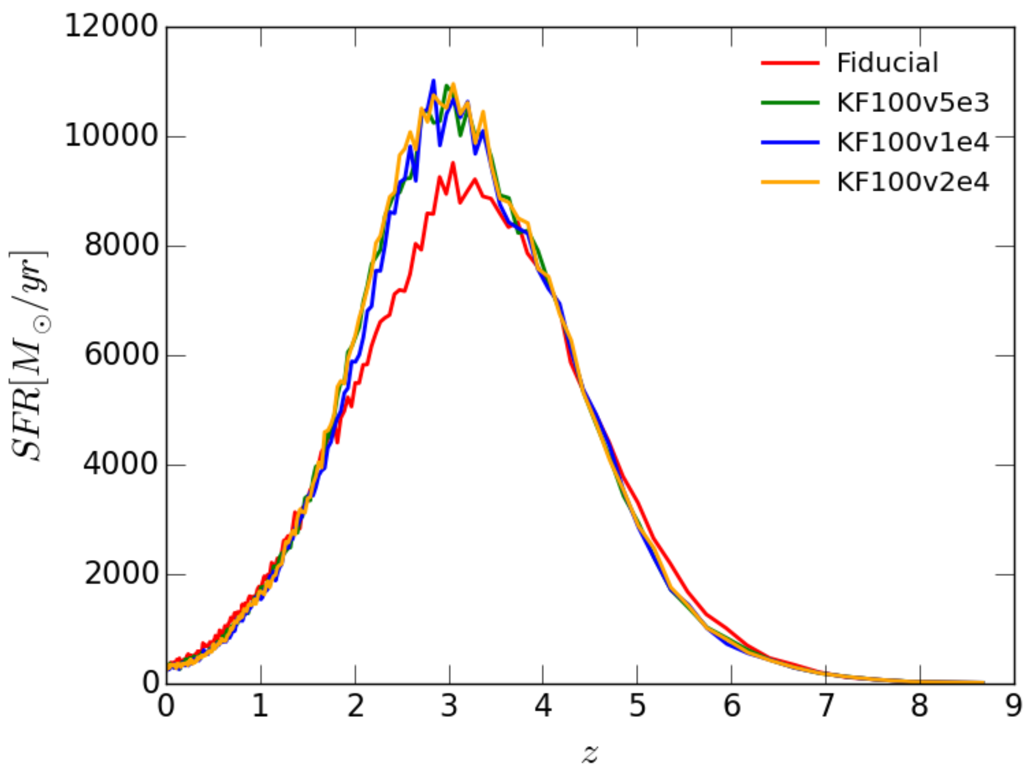

Figure 4.10: Redshift evolution comparison of the star formation rate in the entire galaxy cluster of simulations with different wind velocities (v_w).

values $f_{kin} = 0, 0.5, 1, 5$ are compared with the fiducial simulation. The fiducial run has a slightly higher SFR starting at a redshift ~ 6.3 and continues to have until $z \sim 4.7$ for all simulation except KF500, which achieves a higher SFR at $z \sim 5$.

For redshifts between $z \sim 1.7 - 3.7$ the fiducial simulation is up to $2 \times 10^3\, M_{\odot}\, yr^{-1}$ lower in star formation. The simulations KF000, KF050, and KF100 have their SFR maximum right-shifted with respect to Fiducial and KF500. In the low redshift regime fiducial simulation starts to have again a slightly higher SFR, which can be explained through the exhaustion of gas particles in an environment capable of forming stars in the simulations with new kinetic AGN feedback. The redshift

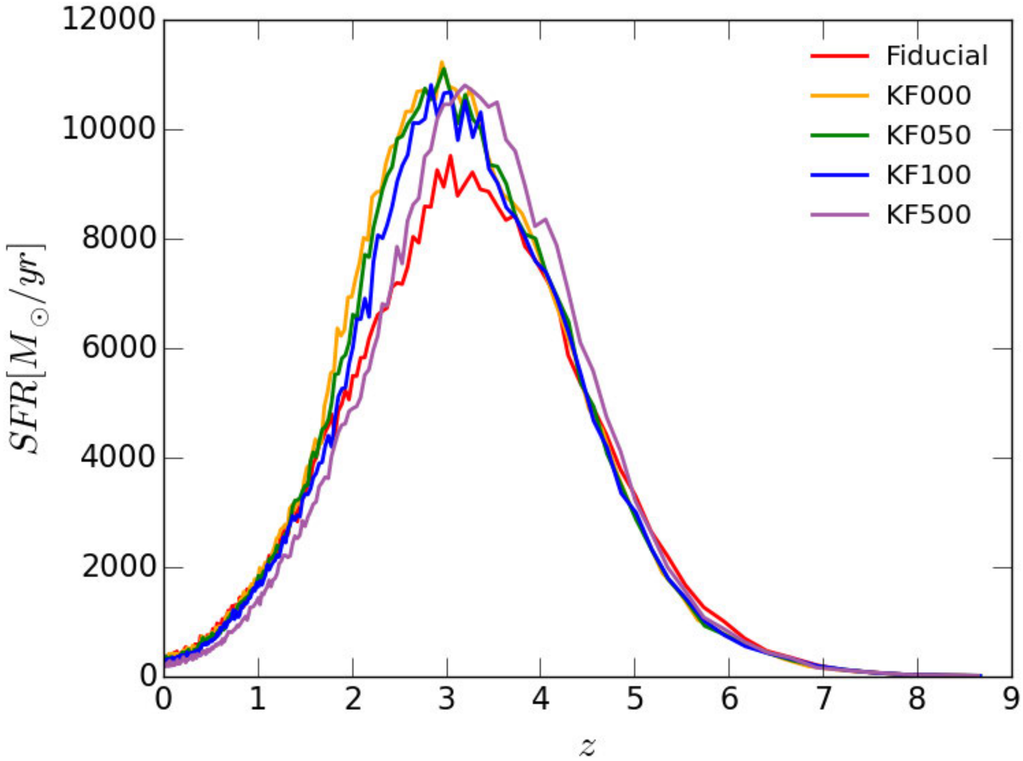

Figure 4.11: Redshift evolution comparison of the star formation rate in the entire galaxy cluster of simulations with different kinetic feedback efficiency, f_{kin}.

evolution of SFR accounts for the different amount of gas particles found in the fast-cooling zone observed in Fig. 4.17. At redshifts $z = 3.2$, 2.32 KF050 has the highest SFR and KF500 the lowest of the simulations with the new AGN feedback model, which explain the appearance of the phase diagram.

4.2.2 *Specific Star Foramtion Rate*

Fig. 4.12 depicts the redshift evolution of the mean specific SFR of the analyzed simulations compared to observational data (i.e. Feulner et al. [74], Dunne et al. [59], Stark et al. [169], Schiminovich et al. [153], Elbaz et al. [62], González et al. [84], and Stark et al. [170]). It demonstrates that our new implementations have no effect on the specific SFR. Hence, the changes in the SFR and in the stellar mass are the same.

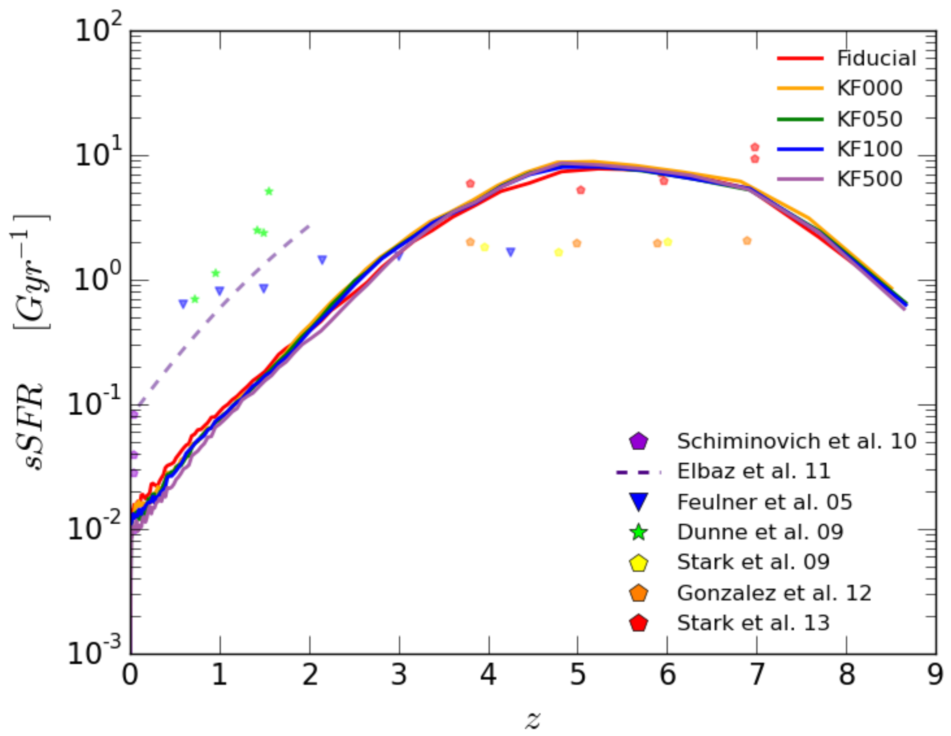

Figure 4.12: History of the specific star formation rate in simulations in comparison to different observations and other theoretical predictions.

Fig. 4.13 shows the SFR–stellar mass plane at different redshifts $z = 0, 1, 2$. The panels illustrate all galaxies in the cluster classified as subhalos using SUBFIND algorithm. For comparison with observations, results fro different surveys (SDSS, GOODS, and GALEX: Elbaz et al. [61], Daddi et al. [44], Salim et al. [148]) are shown (solid and grey dashed-lines). The yellow symbols illustrate the observational results from studies by Tacconi et al. [176]. For a accurate comparison with observations, the simulated galaxies are separated into quiescent (light coloured) and star-forming (dark coloured) using the definition by Franx et al. [78]: galaxies are quiescent for sSFR $< 0.3/t_{Hubble}$. While at high redshift ($z = 2$) the simulations show an almost identical result, for lower redshifts they become more dispersed, reflecting the SFR history shown in Fig. 4.11.

A less efficient AGN feedback in small galaxies is causing the slightly higher result at $z = 0$ for KF100 compared to Fiducial and KF050. The simulations have a better agreement with the observational results by Salim et al. [148] at $z = 0$, which supports the simulation predictions for higher redshifts. The decreasing number of subhalos reflects the merging events of galaxies.

Furthermore demonstrates the redshift evolution of the SFR–stellar mass plane nicely that the most massive galaxies become more and more quiescent with cosmic time. At $z = 0$ there are only very few star-forming galaxies above $log(M_*/M_\odot) = 10.5$, which is the mass at which AGN feedback becomes important.

4.2.3 *Stellar Mass Fraction*

Observational determinations of the fraction of baryons locked up in stars in galaxy clusters, f_*, is consistently found to be a small value. The work by Gonzalez et al. [83] indicates a mass dependency for clusters of masses $M_{500} \sim 10^{14} - 10^{15}\, M_\odot$ having a stellar baryon fraction of $f_* \sim 4\% - 1\%$ respectively. The results of earlier hydrodynamical simulations have shown a lack of feedback processes which are counteracting radiative cooling. With the implementations of the AGN feedback models used in this study, f_* seems to be too small compared to the observational results by Lin, Mohr, and Stanford [115], shown in Fig. 4.14. To obtain their results they used data from the Two Micron All Sky Survey (2MASS) of galaxy clusters with masses of $10^{14} - 10^{15}\, M_\odot$.
The emission-weighted temperature, T_{ew}, of a cluster is defined as

$$T_{ew} = \frac{\sum_i^{N_{gas}} m_{h,i}\rho_{h,i}\Lambda(T_i)T_i}{\sum_i^{N_{gas}} m_{h,i}\rho_{h,i}\Lambda(T_i)}. \tag{4.4}$$

The sum in this equation runs over all N_{gas} gas particles, μ is the mean molecular weight ($\approx 4/(5X_H + 3) \approx 0.6$, for a gas of primordial composition), m_p is the proton mass, $m_{h,i}$ and $\rho_{h,i}$ are the mass and the density associated with the hot phase of the ith gas particle respectively. The cooling function is taken to be $\Lambda(T_i) \propto \sqrt{T_i}$, assuming bremsstrahlung emission. The mean temperature of the hot phase is $\langle T_h \rangle = 1.2 \pm 0.02\, keV$ for the simulated cluster, making it obsolete to use other definitions of T_{ew} which give a better w.r.t. T_{spec} of observed clusters. The result depicts a too efficient SFR quenching.

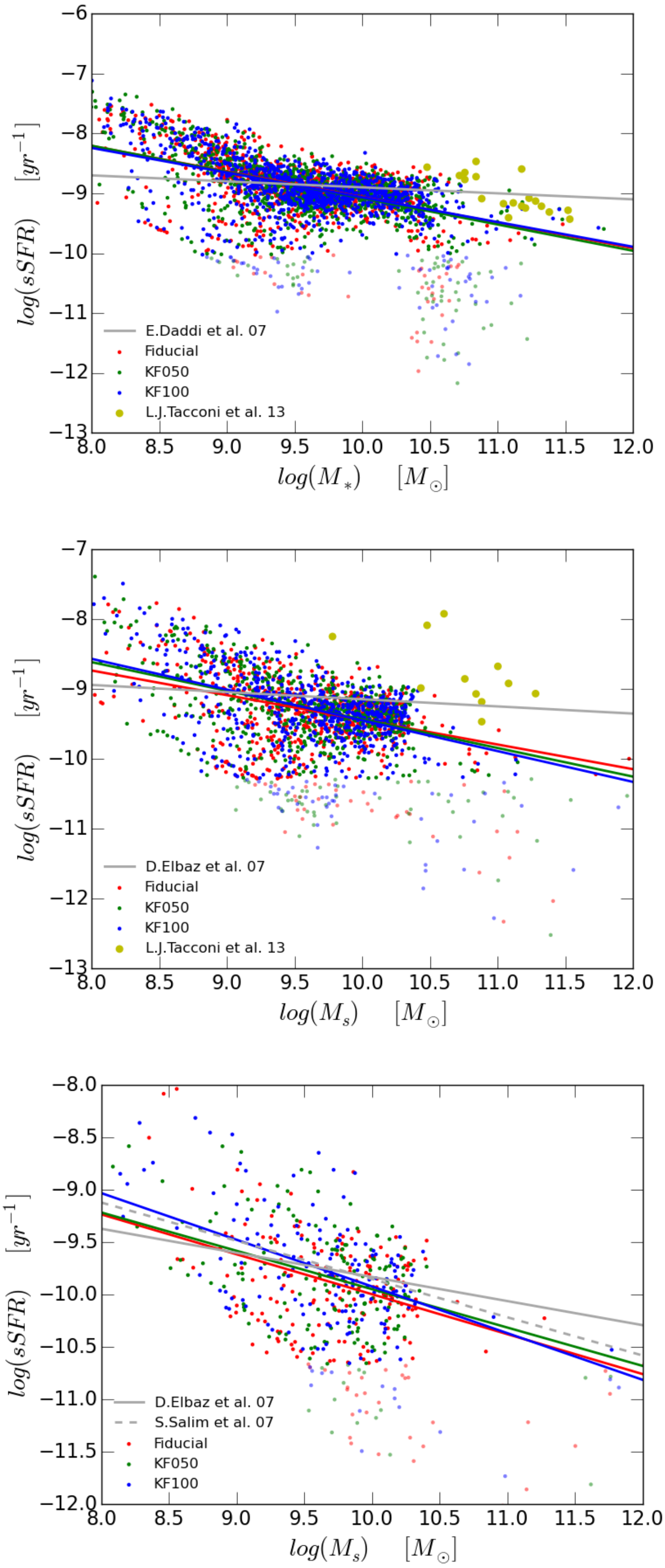

Figure 4.13: sSFRs versus galaxy masses at $z = 0, 1, 2$ (upper, middle and lower panels) for the three models for star-forming central/satellite galaxies (with $sSFR > 0.3/t_{Hubble}$, bright circles/stars) and quiescent central/satellite galaxies (with $sSFR < 0.3/t_{Hubble}$, light circles/stars), respectively. The simulation results are compared to the observed star-forming sequence of galaxies from SDSS and GOODS (black solid lines, Daddi et al. [44]; Elbaz et al. [61]) and to recent observational data from Tacconi et al. [175] and Tacconi et al. [176] (yellow symbols). MW runs reproduce the observed relation fairly well at all redshifts.

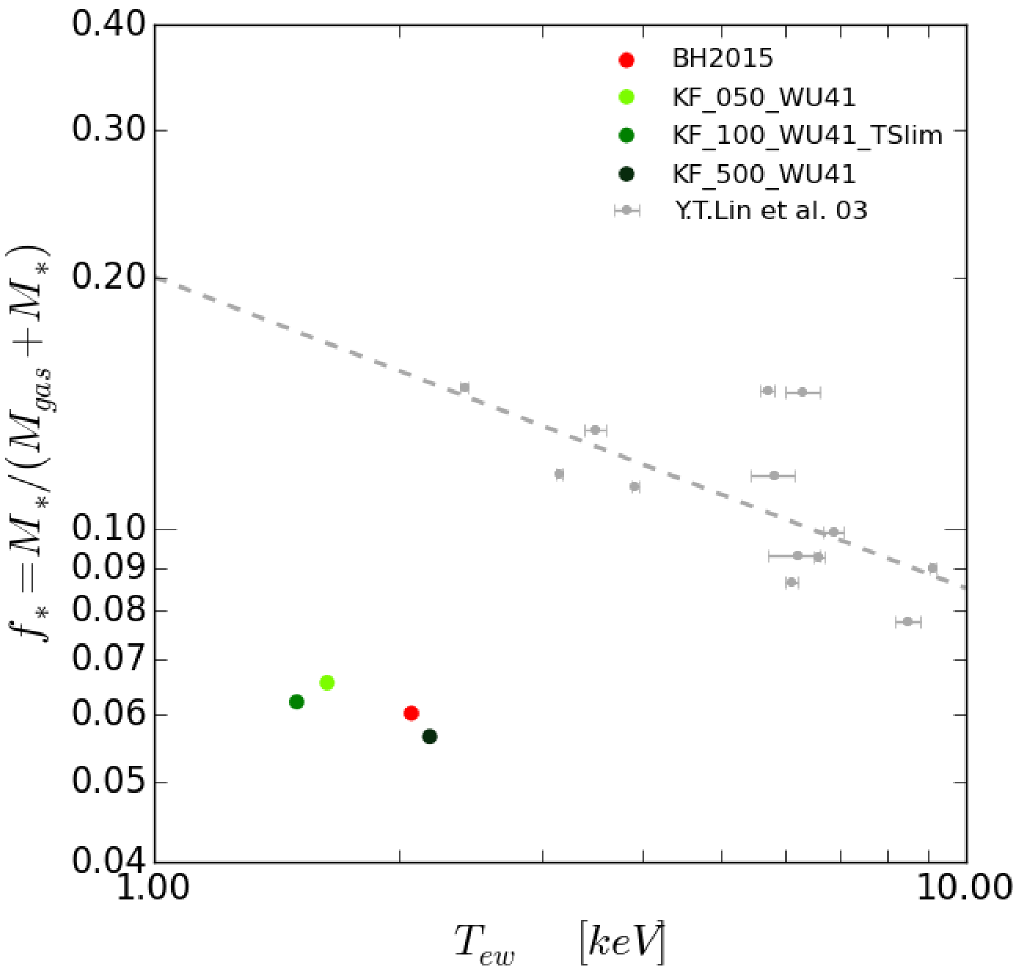

Figure 4.14: The fraction of gas locked into stars, estimated at the virial radius from simulations (small circles) and from observational data (big squares with errorbars; from Lin et al. 2003). The horizontal dashed-line indicates the cosmic value of f_* found in the simulation.

4.3 correlation between black holes and stars

Observations by Zheng et al. [194] (and references therein) have revealed that the SFR and BH accretion rate densities ($\dot{\rho}_{stellar}$ and $\dot{\rho}_{BH}$, respectively) trace each other over cosmic time with $\dot{\rho}_{stellar} \sim 2 \times 10^3 \times \dot{\rho}_{BH}$. Fig. 4.15 shows the predicted cosmic evolution of the SFR (solid lines) and SMBH accretion rate densities (dashed-lines) of the simulations. At very high redshifts > 4 Fiducial has larger $\dot{\rho}_{BH}$ with respect to the other simulations.

In both runs, SFR and BH accretion rates densities peak between $z = 2 - 3$ followed by a steady decline. This is qualitatively consistent with the observational compilation for the star formation rate densities derived from different wavebands (grey scatter: Hopkins and Beacom [97]). Beginning at high redshifts $z \sim 5$ however, the predicted $\dot{\rho}_{stellar}$ is constantly too high compared with the observations, which is due to the fact that the simulations are zoom-in on a galaxy cluster, which have naturally a higher stellar density than filaments or voids. At high redshifts $z > 4$, $\dot{\rho}_{BH}$ is too low compared to the observed star formation rate densities, which is a consequence of resolution.

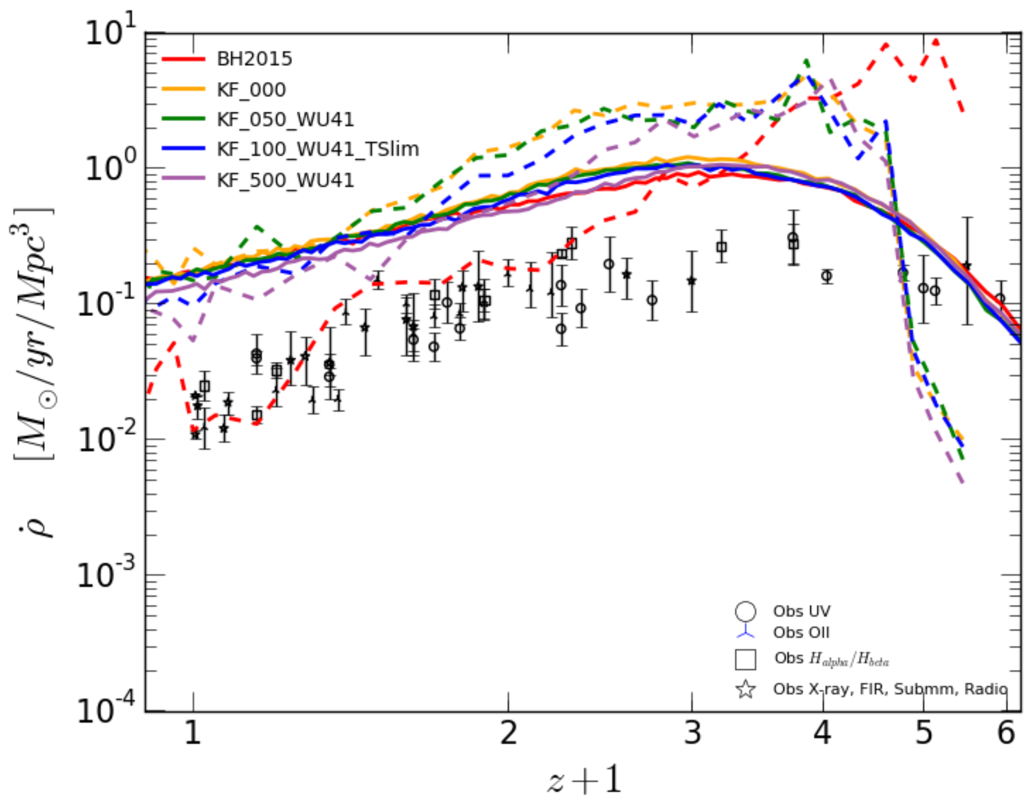

Figure 4.15: Cosmic evolution of mean star formation (solid lines) and BH accretion rate densities (dashed lines). Both, star formation and BH accretion rate densities peak between $z \approx 3 - 4$ followed by a decline towards lower redshifts. They are compared to observed cosmic star formation rate densities derived from different wavebands (black symbols, Hopkins and Beacom [97]).

4.4 PHASE DIAGRAM

With the help of the phase diagram, we can study the effects of a variety of numerical recipes, since the baryons are located within specific regions in the (ρ, T) plane which reflect various processes such as e.g. cooling, radiative heating, shock-heating, gravitational clustering. These processes put a strong constrain on the distribution of matter by the existence of some exclusion regions where rarely particles are found as explained in great detail by Valageas, Schaeffer, and Silk [182].
The first major constrain form the low-temperature region excluded by radiative heating due to the UV background flux, which heats the gas up to $T \sim 10^3\ K$. This constrain is indicated by the blue dashed-line in Fig. 4.16.
The second constrain is expressed by the cooling function $\Lambda(T)$. It lets high-density ionized hot gas ($T > 10^4\ K$) cools very rapidly, such that gas cannot remain for long in highly dens regions at high temperatures. This constrained region is indicated by the black dashed-line on the far right with an inclined "V-shape".

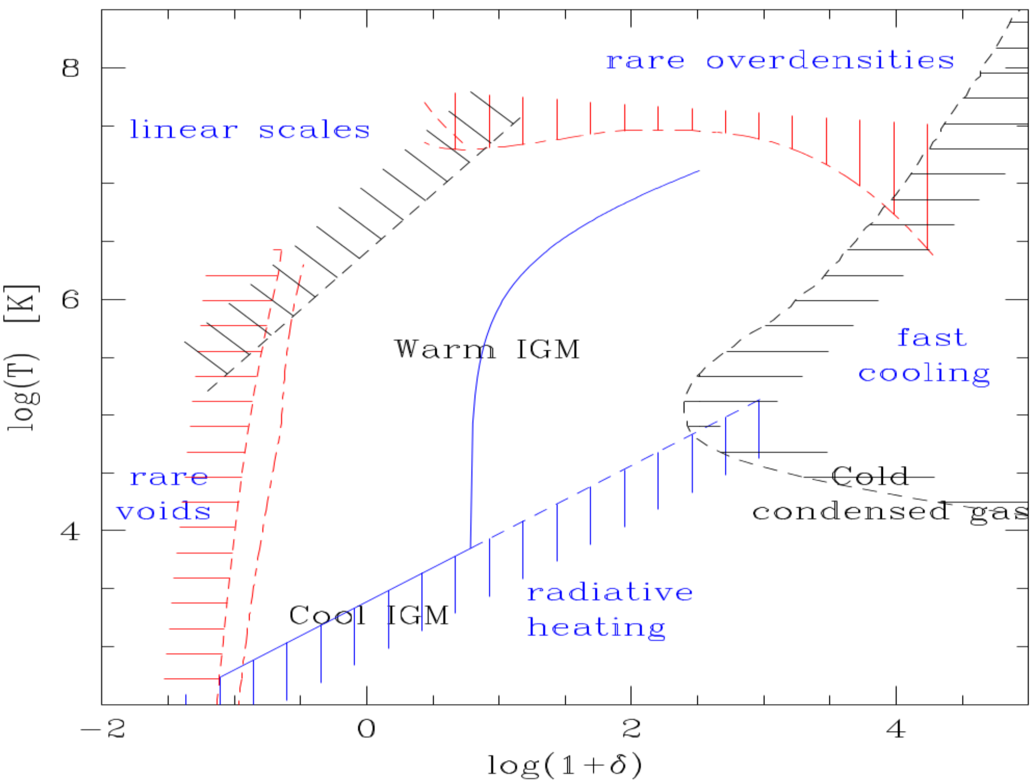

Figure 4.16: The phase-diagram of cosmological baryons at $z = 0$ in a ΛCDM universe. Two IGM phases are distinguishable: the 'cool' IGM (Lyman-α forest), which follows a well-defined equation of state, and the 'warm' IGM, which is constrained to lie within the central domain delimited by the exclusion regions represented by the hatching.
Graphic from Valageas, Schaeffer, and Silk [183].

The second constrain is set by the properties of the dark matter density field it-

self. Indeed, at a given scale R, overdensities ρ_+ above a certain threshold have a negligible probability and only involve a very small amount of matter. The constrain given by the high-density cutoff of the probability distribution function (pdf) $\mathcal{P}(\rho_R)$ in the phase diagram is quite robust and applies to all hierarchical scenarios of structure formation. For matter in such density fields are mainly heated by gravitational interaction (e.g. shock heating) with neighbouring structures. This constrain is located at the upper-right in the diagram, indicated by a red dashed-line. This constrain yields an upper bound $T \sim 10^{7.4}\,K$ at $z = 0$, albeit massive X-ray clusters can obtain higher temperatures.
The third constrain comes from the temperature limit for particles in the non-linear regime at low densities. For gas particles far away from dens regions, which can be heated by stars and SMBHs, there are no sources of external heating (as e.g. the UV background radiation) that can heat up the IGM to high temperatures. This limitation is shown by the black straight dashed-line ($T_{nl} \propto \rho$) to the upper-left.
The final constrain is dictated this time by the lower end of the pdf $\mathcal{P}(\rho_R)$ of the dark matter density field. This is the analog of the high-density cutoff and yields constrain indicated through the curves shown by the two steep parallel red dashed-lines on the very left. The left one stands for the limit set by external heating and the right line shows the effects of local heating.

To compare our simulated galaxy clusters with each other and the theoretical predictions presented by Valageas, Schaeffer, and Silk [182], the phase diagram of gas particles is shown in Fig. 4.17 at redshifts $z = 5.79, 3.2, 2.32, 1.61, 1.05, 0$ (from top to bottom). Note the overdensity $\rho/\rho_{crit} = 1 + \delta$ rather than the density ρ is used in the figures, where $\rho_{crit} = 3H^2/(8pG)$ is the critical density [2]. The number of gas particles per overdensity-temperature bin is encoded through the colour gradient (blue for few, red for many).
Changes in the phase diagram evolution for the fiducial run are not as dramatic as for KF500, and then gap between those two is filled by the gradient of increasing kinetic AGN feedback. For the fiducial simulation the lower temperature constrain is slightly falling for decreasing redshifts, since the density declines faster with ρ than the expansion of the universe which scales with $1/t_H$. For increasing f_{kin} however, the cool IGM seems to vanish almost entirely and instead is relocated to the warm-hot intergalactic medium (WHIM) with temperatures of $10^5 - 10^7\,K$. As it is argued by Cen and Ostriker [29] and Dave et al. [47], up to 50% of the baryons in the IGM could be in the WHIM and provide the explanation for the 'missing' baryonic matter, not found in current observations. To compare this statement with the simulations, Tab. 4.2 shows the ratio between the warm gas density and the total gas density. The best agreement is found for Fiducial, the simulations with higher f_{kin} have respectively more particles in the WHIM. Therefore the IGM gas of Fiducial can cool more efficiently than if relativistic jets are simulated through kinetic feedback, which can carry hot gas towards the IGM.
A feature that is found in all simulations is the disappearance of gas particles

2 The threshold density between a universe which has enough mass/volume to close the universe and too little mas/volume to stop expansion is called the critical density.

with overdensities > 4 and temperatures $< 10^4\,K$ due to star formation. The gas with density above the star formation threshold is placed in an effective equation of state developed by Springel and Hernquist [166] (Sec. 3.3), which appears to be a 'tail' in the phase diagram.

A prominent difference between the simulations is clearly visible for densities at $\rho \sim 3-4$ at redshifts $z = 3.2, 2.32$. At these periods KF050 has the most gas particles in the fast-cooling zone, followed by KF100 and KF500 respectively and Fiducial having the least. This difference becomes clearer when analyzing the star formation rate (SFR) evolution, as is done in Sec. 4.2.1. Gas is brought to this region through thermal energy feedback processes of stars, supernovae, and SMBHs.

Simulation ID	ρ_{warm}/ρ_{total}
Fiducial	0.499
KF050	0.529
KF100	0.530
KF500	0.544

Table 4.2: Ratios of the warm gas density and the total gas density.

Predominantly particles which experience thermal AGN feedback will populate the crossover region between dense hot and diffuse hot gas, which becomes noticeable at $z = 1.61$ as a small extension towards the left at temperatures of $\sim 10^{7.5}\,K$ and a overdensity of ~ 1. The extension grows further to the right until $z = 0$. This is consistent with a picture where the very dense cold gas in the vicinity of the AGN is heated by thermal AGN feedback and moved away from the effective equation of state. As thermal energy is converted to kinetic energy, this gas escapes to regions of lower density. The same feature is analyzed in the simulations presented in Costa et al. [40].

Furthermore, a high temperature bump at overdensity around ~ -2 starts to be visible at $z = 3.2$ for simulations with kinetic AGN feedback (becoming more distinct with higher f_{kin}). This feature is the combined effect of a predominant thermal AGN feedback and a minor kinetic AGN feedback, since most SMBHs are accreting at rates of $f_{Edd} > 0.1$ as shown in Fig. 4.2. The thermal AGN feedback increases the IGM temperature through gas particles which change part of their thermal to kinetic energy, and kinetic AGN feedback heats the IGM through shocks (e.g. at hot spots discussed in Sec. 2.4.2). When the average SMBH accretion rate (see App. B.1) starts at $z = 1.5$ to fall under $f_{Edd} \sim 0.05$ ($log(f_{Edd}) \sim -1.3$), the temperature bump clearly decreases until it has vanished at $z = 0$.

Another discrepancy between the simulation runs which grows with time is the extension to very low densities. For KF500 it begins at $z = 2.3$. This extension is clearly visible for the simulations with kinetic feedback, since it is the imparted wind velocity on gas particles, which carries them outside of galaxies into very thinly populated areas.

Growth of the upper temperature bound that takes place in all simulations with decreasing redshift, expresses the fact that the virial temperature associated with larger scales which turn non-linear later is higher. For instance, the velocity dispersion related with galaxies is of the order $\sim 200 km\,s^{-1}$ while for clusters it is $\sim 1000 km\,s^{-1}$.

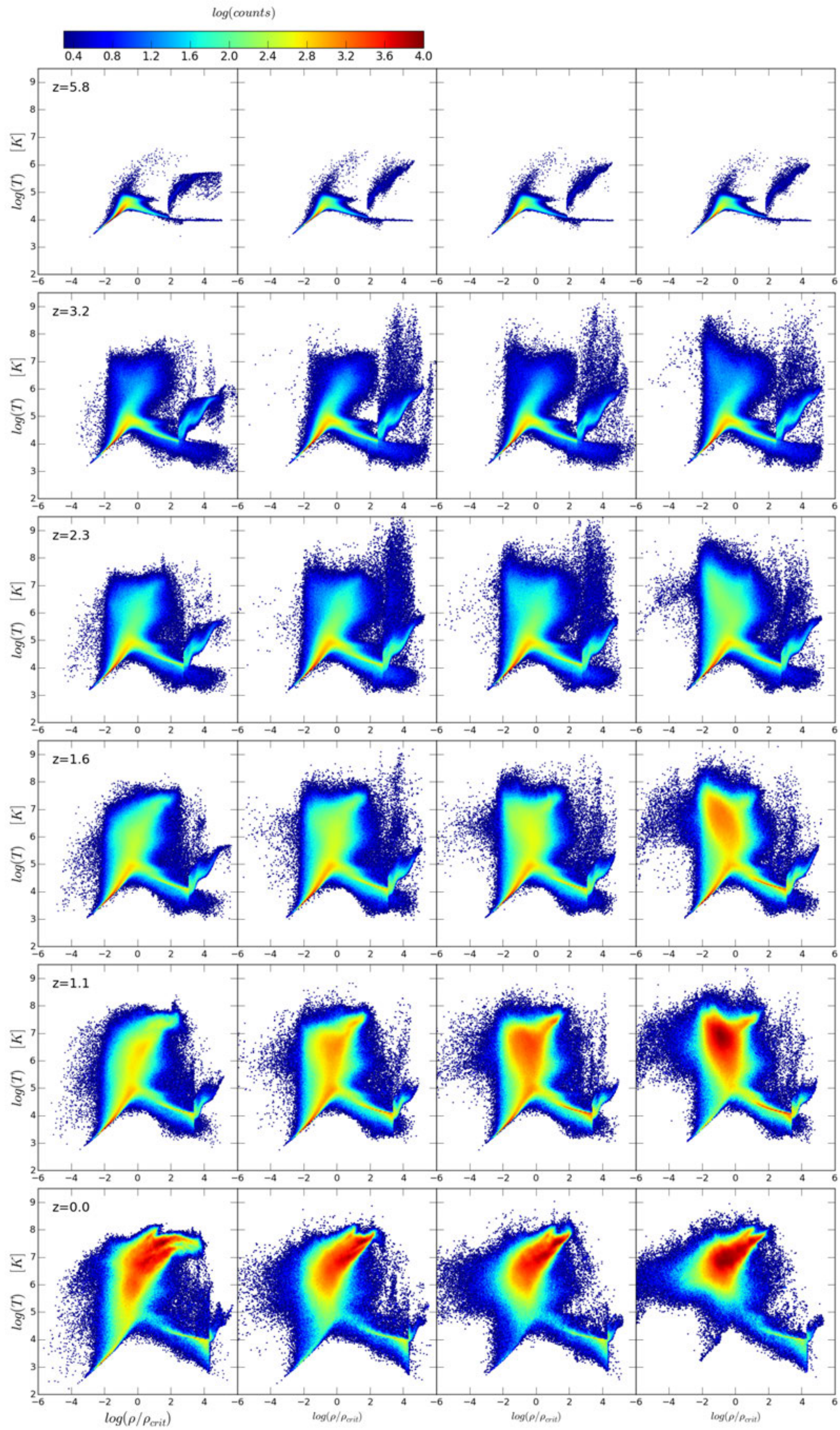

Figure 4.17: Number density of gas particles in the $\rho - T$ phase diagram at six different redshift eras: $z = 5.79$ (top), $z = 3.20$ (2nd from top), $z = 2.32$ (3rd from top), $z = 1.61$ (4th from top), $z = 1.05$ (5th from top), $z = 0$ (bottom).

Additional plots which visualize the environments of particle, which get into some of the characteristic regions discussed above are shown in App. B.4.
The phase diagram of particles which are subject to the kinetic AGN feedback is shown in Fig. 4.18. Here the condition of gas just before it is kicked is shown for the entire cosmological times. As expected, there are les particles kicked if the simulation has a lower f_{kin}. Furthermore are predominantly gas particles imparted with a wind velocity vector, which are either in region that are cold dense region directly around the SMBH, or less dense and hot. But only very few particles are kicked out of the phase diagram region due to kinetic AGN feedback as can be concluded by comparing the colour-bar ranges between Fig. 4.18 and Fig. 4.17.

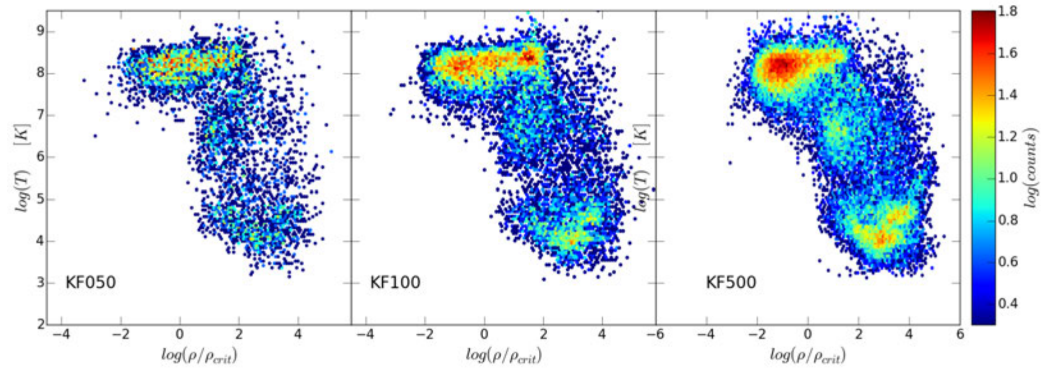

Figure 4.18: Number density of gas particles which receive kinetic AGN feedback energy in the $\rho - T$ phase diagram for KF050 (left), KF100 (middle), and KF500 (right).

4.5 BRIGHTEST GALAXY CLUSTER

4.5.1 *Maps*

The following three figures show the evolution of the density, temperature and entropy distribution in a box with a side-length of $4 Mpc\, h^{-1}$ centered on the BCG. Red crosses are indicating the positions of SMBHs. The relativistic jet, replicated through the kinetic feedback, is not visible since the map shows a too large region, even though the vertical axis of the map is aligned with the jet. However, zooming in on the central region would not make a difference, because the low resolution of our simulations forbids us to directly see the collimated outflow.
The effect of the kinetic feedback is clearly visible in all four shown redshifts of the density maps. At $z = 3$, the galaxy filaments [3] become more dispersed with higher kinetic feedback efficiency f_{kin} (increasing from left to right in Fig. 4.19). So far not many SMBHs have formed, and there seems to be not major difference in number and positions. With decreasing redshift, the difference in density distribution increases between the simulations. At $z = 1.48$, the ICM of KF500 is much denser with respect to our fiducial simulation Fiducial, but for the central region vice versa. This could cause a slower merging rate for the BCG in KF500 with satellite subhalos. This idea is further supported by the seemingly smaller satellite subhalos. Albeit, looking at the lower redshift maps at $z = 0.76$ and $z = 0$, the incoming satellite subhalos seem to at approximately the same positions in all simulations, indicating that the difference in the gravitational potential field is minor. At $z = 0$ the SMBHs in the fiducial simulation are more clustered in the center and higher in number. Whereas the fiducial run has 135 SMBHs in the cube centred on the BCG, KF050 has 119, KF100 has 109, and KF500 has 108.

3 Galaxy filaments are thread-like formations along which galaxies are pulled towars galaxy clusters. They give the universe the neural-network-like appearance.

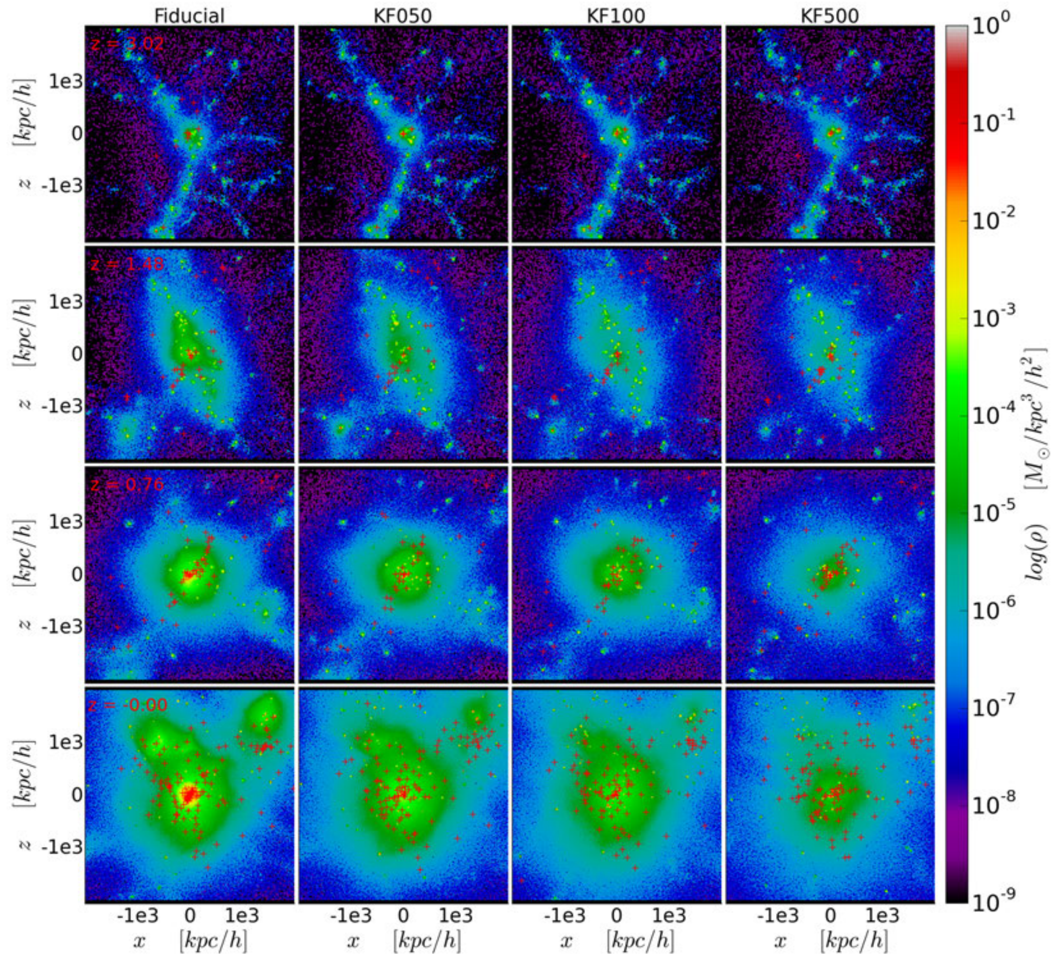

Figure 4.19: Projection in (x, z)-plane of gas density centered on the BCG. The columns show the maps for Fiducial, KF050, KF100, and KF500 (from left to right). The rows show each map at redshifts $3, 1.48, 0.76, 0$ (from top to bottom). The red crosses indicate the positions of SMBHs.

What we have seen in the density map repeats itself in the temperature and entropy map. That is, the contrast in gas properties is strongest in the fiducial simulation and becomes weaker as f_{kin} increases. In Fig. 4.20 the hotter regions around the BCGs centre are an evidence of the kinetic AGN feedback, since the gas which is kicked into wind with $v_w = 10.000 km\,s^{-1}$ thermalizes its kinetic energy in the form of shocks. At $z = 0.76$ thermal feedback of the SMBHs (of which the positions are indicated through blue crosses) visible through the white colour patches surrounding them. At $z = 0$ is a clear asymmetry, with gas above the centre at higher temperatures then the gas below. This is caused the subhalo which is merging with the BCG as can be seen more clearly in the density maps.

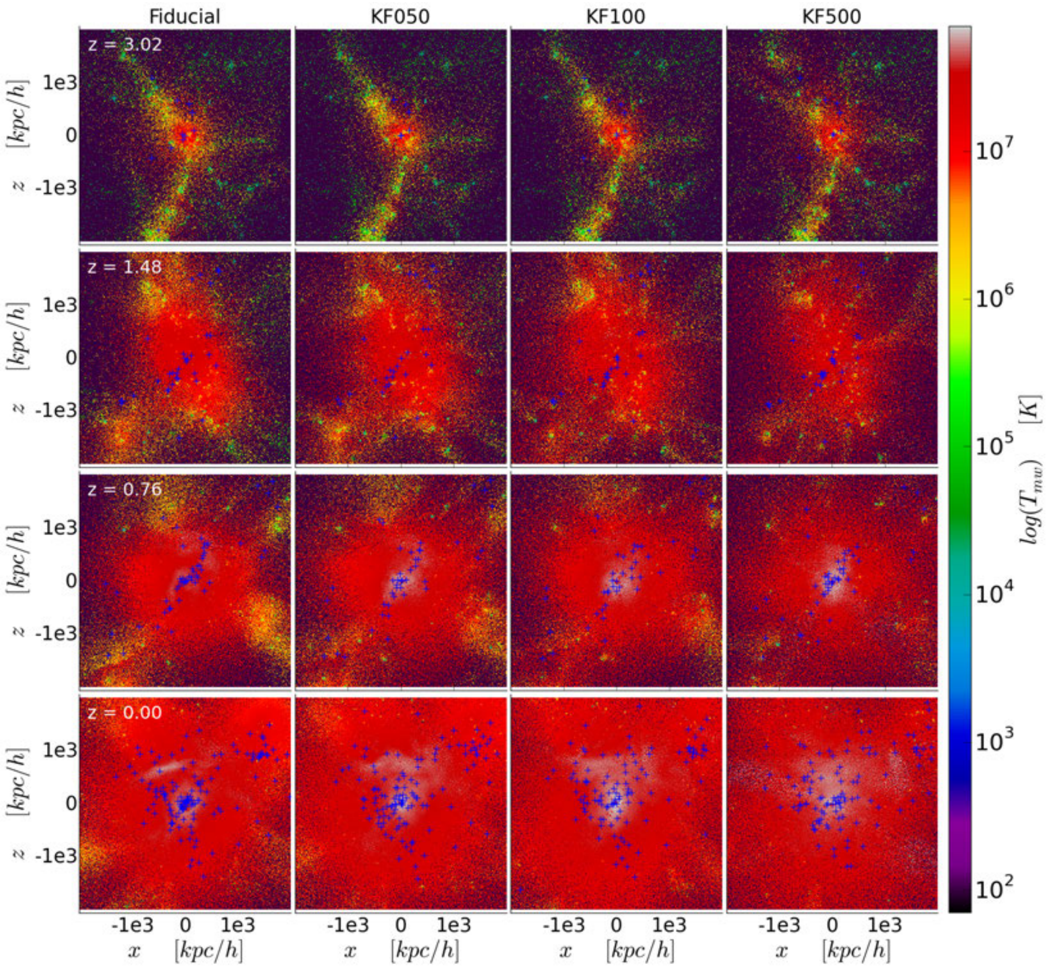

Figure 4.20: Projection in (x, z)-plane of gas mass-weighted temperature centered on the BCG. The columns show the maps for Fiducial, KF050, KF100, and KF500 (from left to right). The rows show each map at redshifts $3, 1.48, 0.76, 0$ (from top to bottom). The blue crosses indicate the positions of SMBHs.

In the entropy maps of Fig. 4.21 we see low-entropy gas, which together with metal-enriched gas is associated with merging substructures and filaments, sink toward the central regions of the BCG up until $z = 1.48$. The entropy maps at $z = 0$ indicate that the entropy gradient becomes shallower as from Fiducial until KF500. Since non-cool core (NCC) clusters are observed with nearly isentropic gas cores at a higher entropy level (Maughan et al. [119]), this could show the KF500 is indeed a NCC cluster.

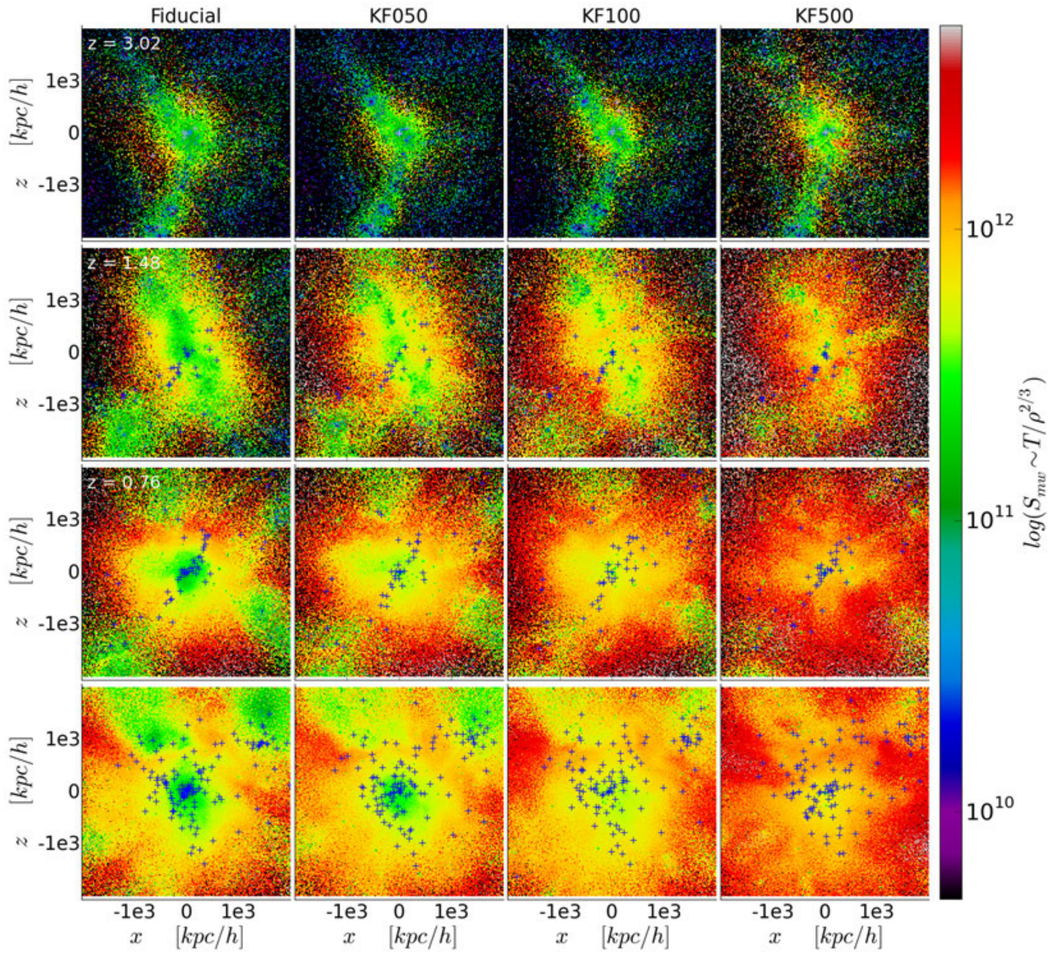

Figure 4.21: Projection in (x, z)-plane of gas mass-weighted entropy centered on the BCG. The columns show the maps for Fiducial, KF050, KF100, and KF500 (from left to right). The rows show each map at redshifts $3, 1.48, 0.76, 0$ (from top to bottom). The blue crosses indicate the positions of SMBHs.

The metallicity, which describes the abundance of all elements except hydrogen and helium, is shown in Fig. 4.22. Elements which are heavier than hydrogen and helium are produced in stars in distributed to the gaseous environment through supernovae explosions. Therefore the major part of the metallicity is found around the star forming regions in filaments and subhalos.

The 2D projection of physical properties of the BCG further show a hierarchical build up of the BCG, which is ubiquitous in the ΛCDM universe. This can partially be seen as a disprove of the monolithic collapse model.

4.5.2 *Radial Profiles*

For a clearer comparison between the simulations, the following figures show a direct comparison of radial profiles of gas properties at the same four time epochs

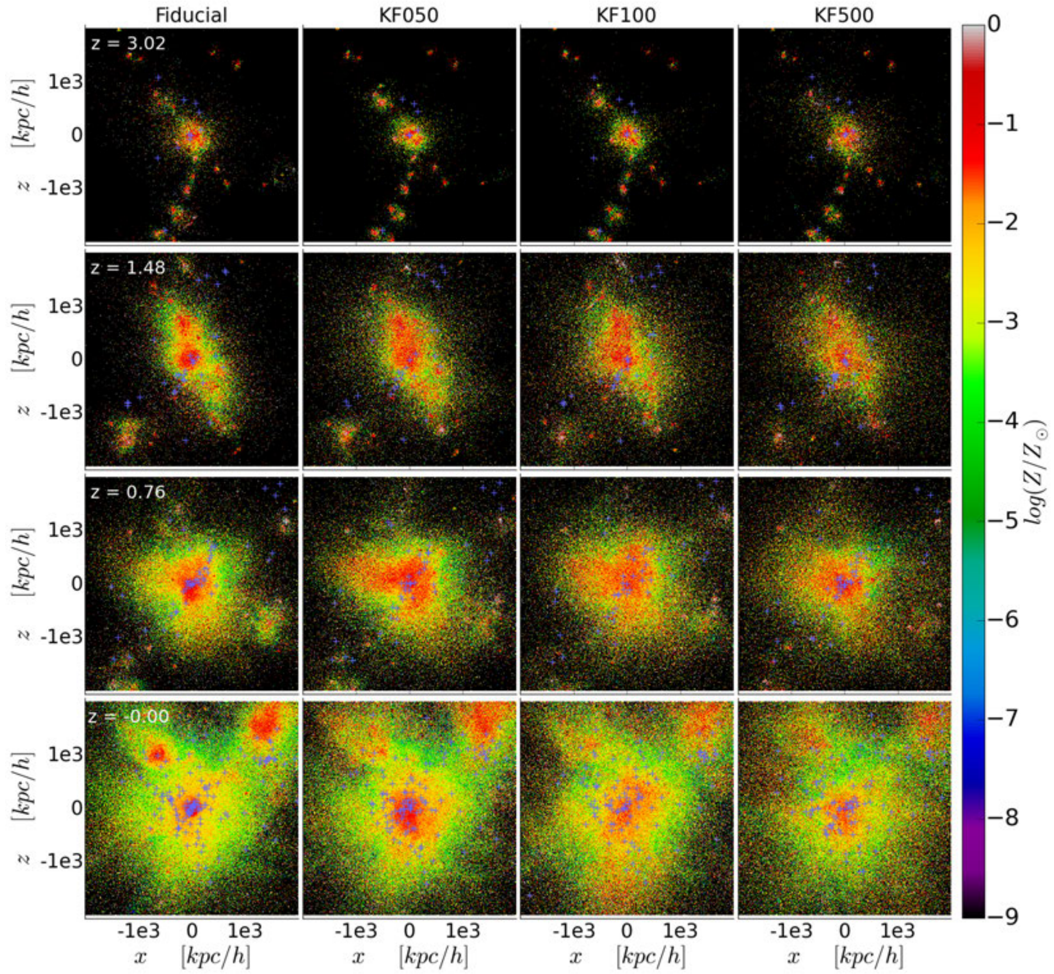

Figure 4.22: Projection in (x, z)-plane of the metallicity centered on the BCG. The columns show the maps for Fiducial, KF050, KF100, and KF500 (from left to right). The rows show each map at redshifts $3, 1.48, 0.76, 0$ (from top to bottom). The light blue crosses indicate the positions of SMBHs.

as they were used for the maps. Each property is shown as a function of distance from the location of BCG potential minimum. The curves denote the mean value of the relevant property in each radial bin.
The density profiles of gas shown in Fig. 4.23 show clear distinctions between the simulations. At $z = 3.03$ the fiducial simulation is less dense in the neighbourhood of the centre than the other simulations. Starting at $z = 1.49$, the fiducial simulation accumulates more gas and becomes therefore more dens than the other simulations. For the simulations with the new kinetic AGN feedback module, the density decreases for higher values of f_{kin}.

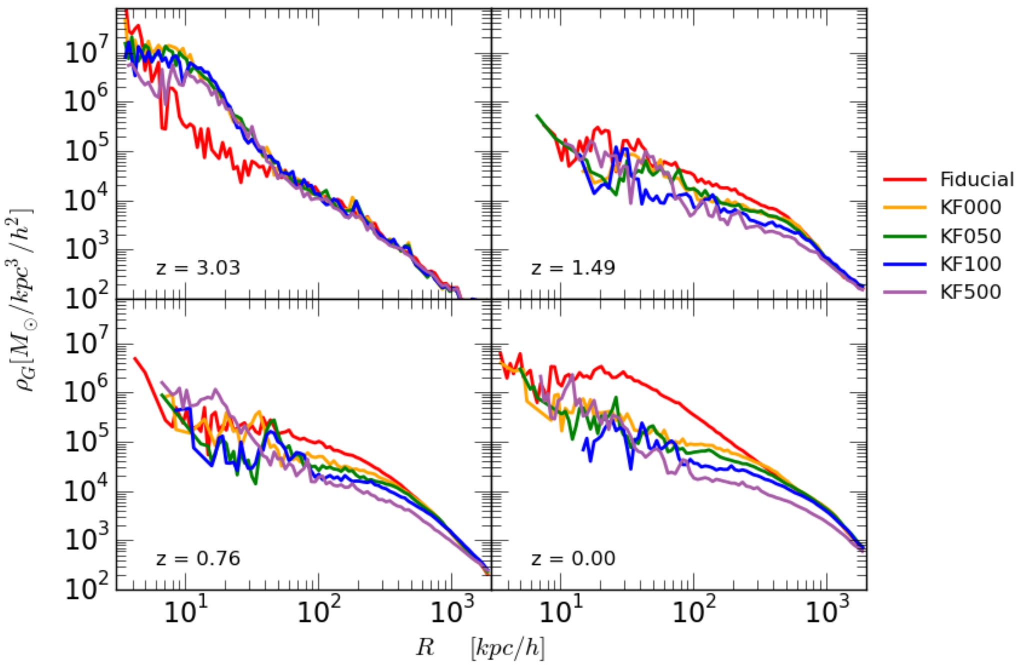

Figure 4.23: Radial profiles of gas density around the BCG centre at four different redshifts: $z = 3$ (top-left panel), $z = 1.49$ (top-right), $z = 0.76$ (bottom-left), and $z = 0$ (bottom-right).

Since the densities in the new kinetic AGN feedback simulations were lower with respect to Fiducial, their temperatures are expected to be higher. Yet, the temperature at the centre of KF500 is lower by more than one order of magnitude compared to the fiducial run. It appears to be caused by the kinetic AGN feedback which is especially active in lower redshift epochs. As outlined in the previous section, does the kinetic feedback tend to carry gas outwards which has high temperatures (see Fig. 4.18). KF000, KF050, and KF100 show a less drastic difference with regard to the fiducial simulation. For all runs with a mechanical AGN outflow the temperature is higher at $\sim 10^2\, kpc\, h^{-1}$ and becomes equal to the fiducial run at larger distances.

Because the entropy was calculated using the astrophysical interpretation for galaxy clusters $S \propto T/\rho^{2/3}$, the profiles derive straightforward from the two previous figures. Redial profiles for the redshift epoch $2 < z < 4$, where the SFR are

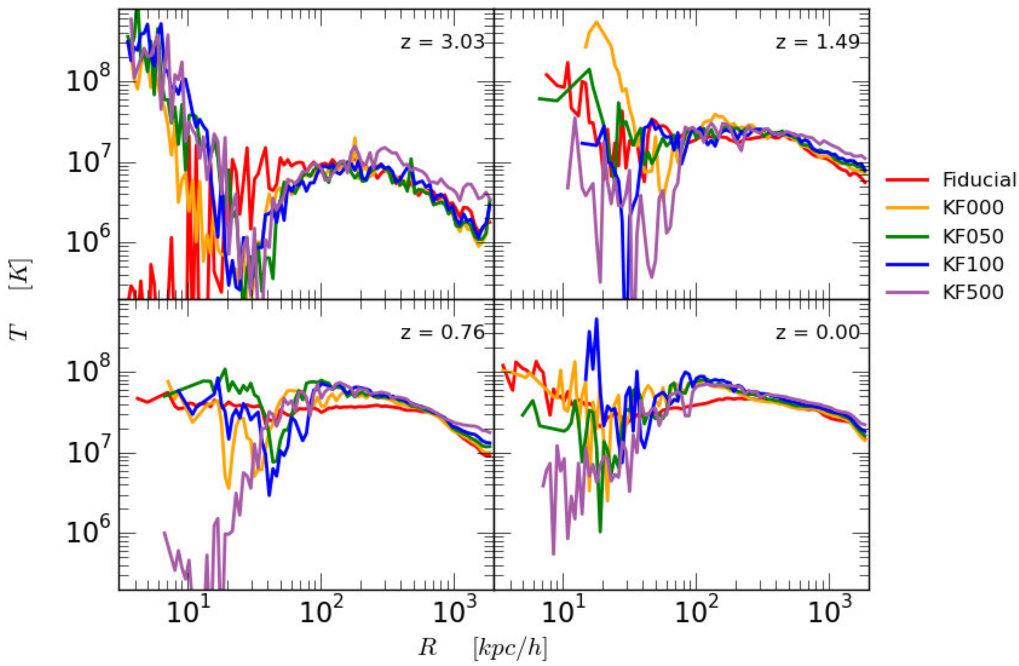

Figure 4.24: Radial profiles of gas temperature around the BCG centre at four different redshifts: $z = 3$ (top-left panel), $z = 1.49$ (top-right), $z = 0.76$ (bottom-left), and $z = 0$ (bottom-right).

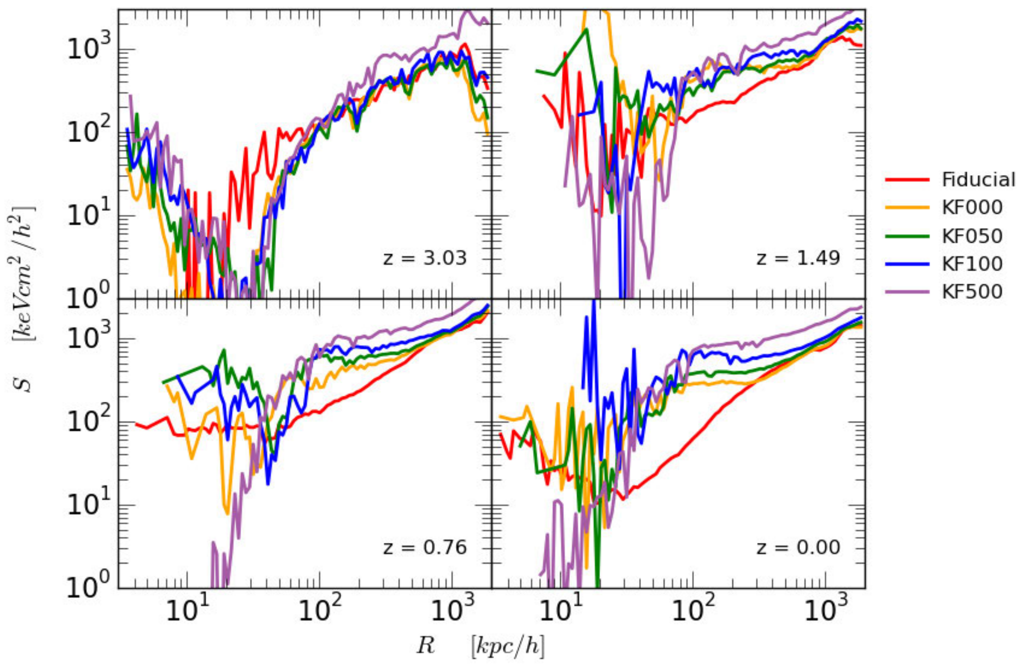

Figure 4.25: Radial profiles of gas entropy around the BCG centre at four different redshifts: $z = 3$ (top-left panel), $z = 1.49$ (top-right), $z = 0.76$ (bottom-left), and $z = 0$ (bottom-right).

quite distinguishable between the fiducial and the other simulations are shown in App. B.2.

To see how well the profiles of the simulated cluster agrees with observational data, the X-ray profile data from the ACCEPT sample (Cavagnolo et al. [28]) is used. The comparison requires to find the accurate location of the halo centre. In order to do so, the procedure presented by Power et al. [138] was used and is further explained in App. A.5. In Fig. 4.26, an good agreement between the simulated and observed clusters can be seen. With regard to the entropy profile in

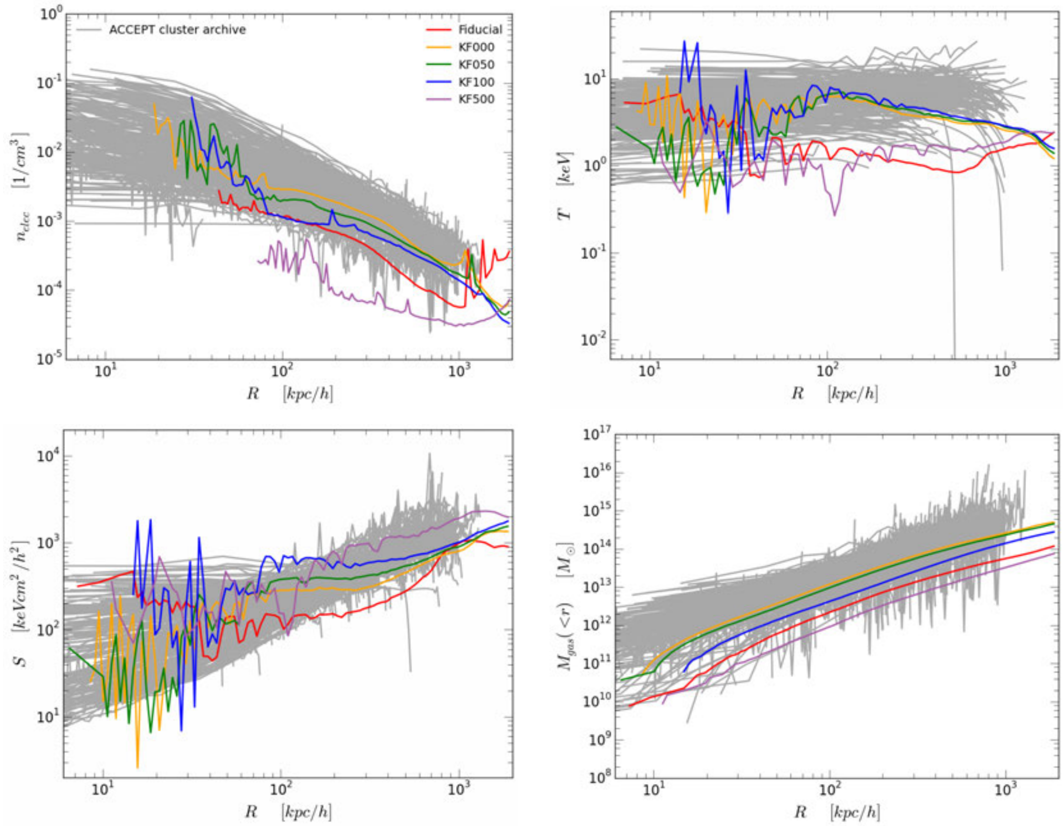

Figure 4.26: Comparison of ICM profiles from our simulations (coloured lines) with observational data from ACCEPT clusters (grey lines): electron density profiles (top-left panel), entropy profiles (top-right), temperature profiles (bottom-left), and total mass profiles (bottom-right).

Fig. 4.26, simulations with $f_{kin} = 0, 0.5$ (KF000 and KF050) show a lower entropy in the central region than the rest. Following Hahn et al. [87], who defines of a cool-core cluster as one with a decreasing profile and a central entropy of at most $40\,keV\,cm^2$ at $r = 10\,kpc$, KF000 has a cool-core (with $27\,keV\,cm^2$ in the central $r = 10\,kpc$).

4.6 IN- AND OUTFLOW

Since the new kinetic AGN feedback routine is kicking gas particles into the wind, instead of exciting them thermally as in the fiducial simulation, differences in the in- and outflow should exist. The following figure (Fig. 4.27) compares the velocity maps of the simulations at different redshifts. The velocity field is separated into gas which is falling onto the BCG (brown and white colour) and gas which is moving away from the BCG centre (green and blue colour). The colourbar shows the logarithm of the ratio between the velocity of the ith particle, u_i, with the maximum velocity attained by a particle ($log(u_{i,out}/mean(u_{out}))$ for the outflow). Hence, as the spread in the velocity distribution becomes larger, the higher and lower $log(u_i/mean(u))$ becomes for the in- an outflow respectively. Especially at

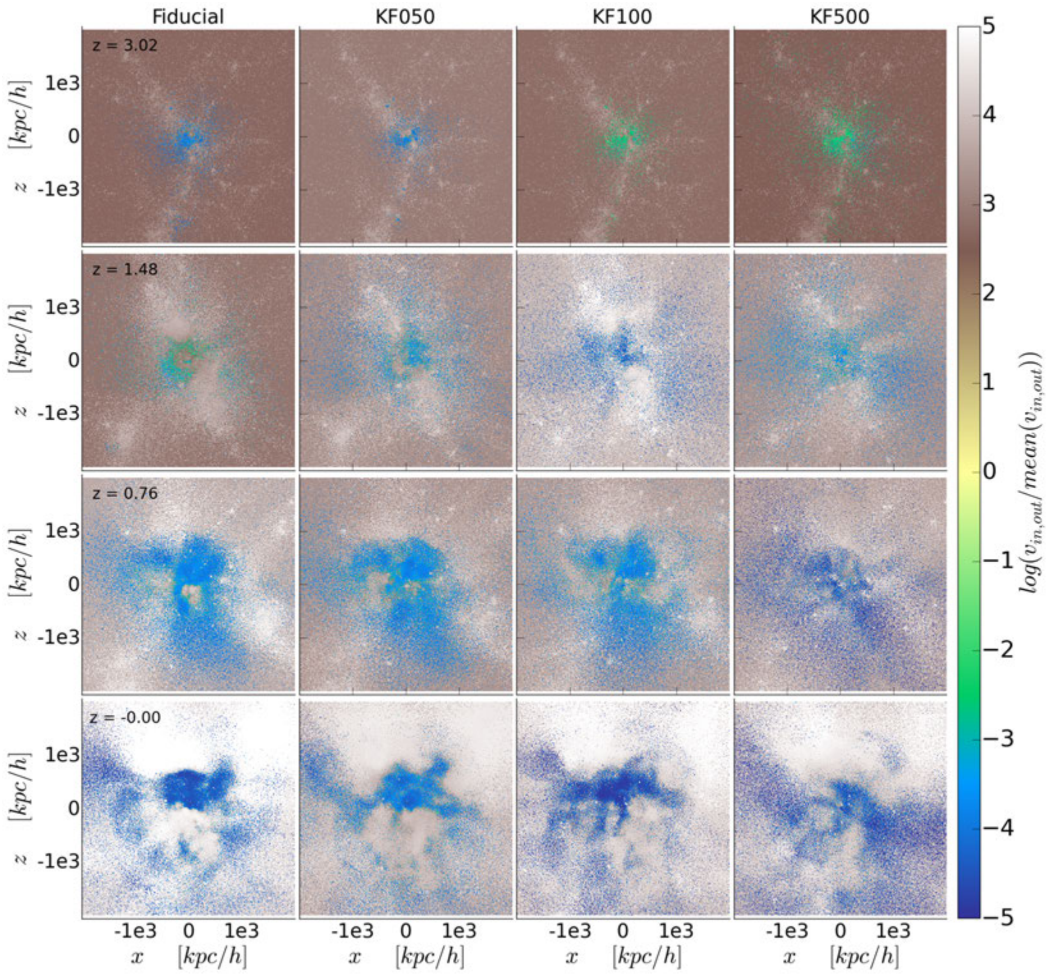

Figure 4.27: Projection in (x, z)-plane of the in- and out-flowing logarithmic velocity ratio u/u_{max} centered on the BCG. The columns show the maps for Fiducial, KF050, KF100, and KF500 (from left to right). The rows show each map at redshift $3, 1.48, 0.76, 0$ (from top to bottom).

$z = 3.02$ one can see around the BCG centre a discrepancy of the outflow between the two simulation on the left (Fiducial and KF050) and right (KF100 and KF500). The outflow seems to posses a more uniform velocity in the latter two (whether it is faster or slower is shown in Fig. 4.28). Another interesting feature visible at $z = 3.02$ are the filaments which are pulled at a higher speed towards the BCG centre than the voids . As the redshift decreases below 1, more gas is flowing out due to the kinetic AGN feedback. The two white patches to the top of the BCG centre at $z = 0$ indicate the two subhalo satellites which will merge with the BCG (they are clearly seen in Fig. 4.19).

Turning now to the comparison of redshift evolution of the balance of gas inflow and outflow, Fig. 4.29 shows the mass ratio of the in- and outflow. The mass flow was measured through shells with radii $R_{shell} = 50, 100, 150, 200, 300$. All gas particles which are within 10% of R_{shell} were taken into accounted. The velocity and temperature of the outflow, shown in Fig. 4.28) and Fig. 4.30 respectively, are the mean value of the gas in a shell, as well as of the shells together. The shells are used to derive a approximate value of the escape velocity, which in turn is used to represent the velocity as a dimensionless quantity.

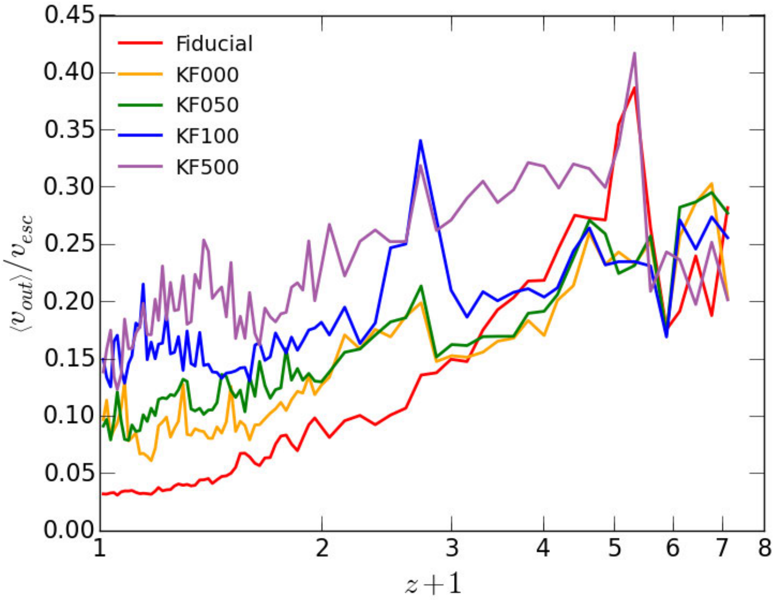

Figure 4.28: Redshift evolution of the ratio between the mean outflow velocity and the escape velocity.

It does not come as a surprise that mean velocity is highest for KF500 and lowest for the fiducial simulation. The reasons are the lower gas density for KF500 and the kinetic AGN feedback routine.
The ratio of the outflowing matter with respect to the combined in- and outflowing matter is shown in Fig. 4.29. Overall there is a good agreement between the simulations, with the only difference being between $3.1 < z < 4.6$. As expected does the inflow carry more matter at early times than the outflow. Only at low redshifts do the in- and outflow transport almost the same amount of matter. It is also interesting to notice that there is a decrease after every time there is a peak in outflowing mass. This indicates that the SMBHs is pushing away it's own accretion sources.

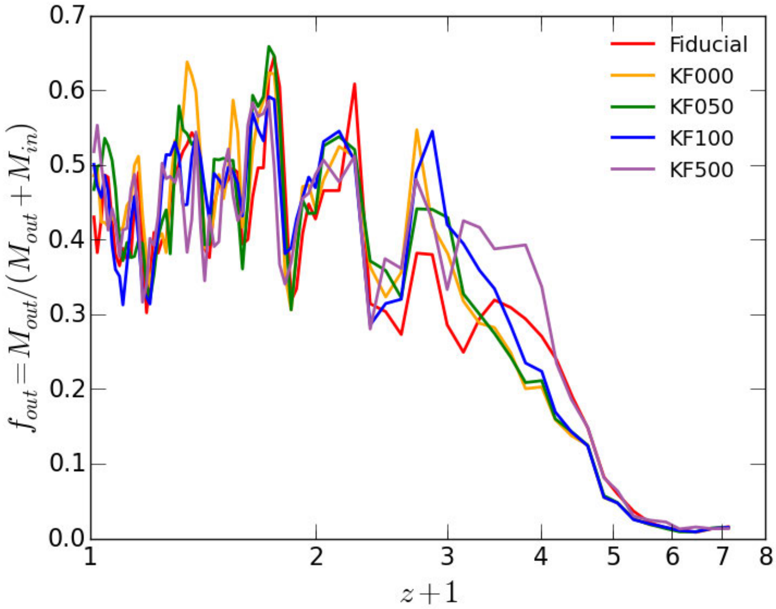

Figure 4.29: Redshift evolution of the mean outflow mass fraction.

The impact of the thermal AGN feedback, which is dominant at high redshifts (as seen in Sec. 4.1.1), can clearly be seen in Fig. 4.30. At redshifts $5 < z < 6$, the outflow experiences a huge temperature rise, which lasts longest for KF500. The fiducial simulation starts to have a lower temperature in the outflow than the

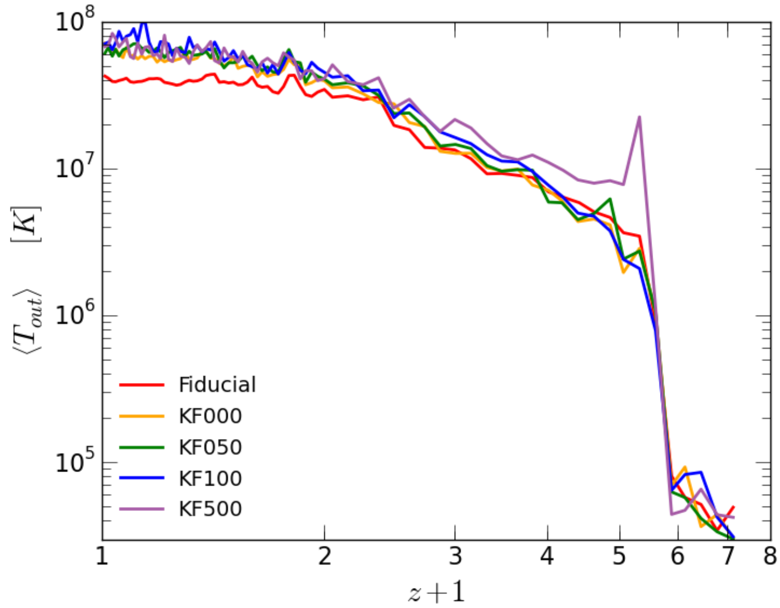

Figure 4.30: Redshift evolution of the mean outflowing gas temperature. The lines indicate the mean values.

other simulations at redshifts $z < 2.3$. Thus around the time when most SMBHs are in the radio-mode and kinetic AGN feedback starts to dominate. As discussed in Sec. 4.4, does the jet carry especially high temperature gas with it, which could explains the higher temperatures of the simulations with the new kinetic AGN feedback model.

Fig. 4.31 shows the inflow rates, which are higher at high redshift and become balanced when AGN feedback becomes important at $z < 5$. The lower inflow rates at $z > 5$ are a consequence of a later assembly of stellar structures due to galactic winds, as shown by Hirschmann et al. [92].

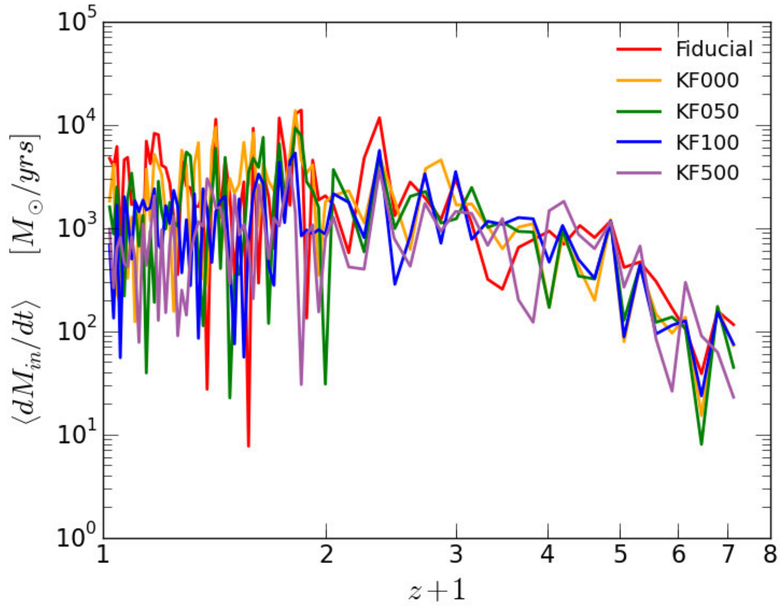

Figure 4.31: Cosmic evolution of the inflow rates. The lines indicate the mean values.

The mass loading $(M_{out} - M_{in})/SFR$, visualized in Fig. 4.32, shows how much gas is thrown out for each stellar mass formed. The strong oscillations dut to AGN feedback that have been visible in Fig. 4.29 appear again. At high redshifts $z > 5$, the SFR increases more than the net outflow rate, predicting a decrease in mass loading with decreasing redshift. This trend however quickly becomes more shallow through the dominating AGN feedback at $z < 5$.

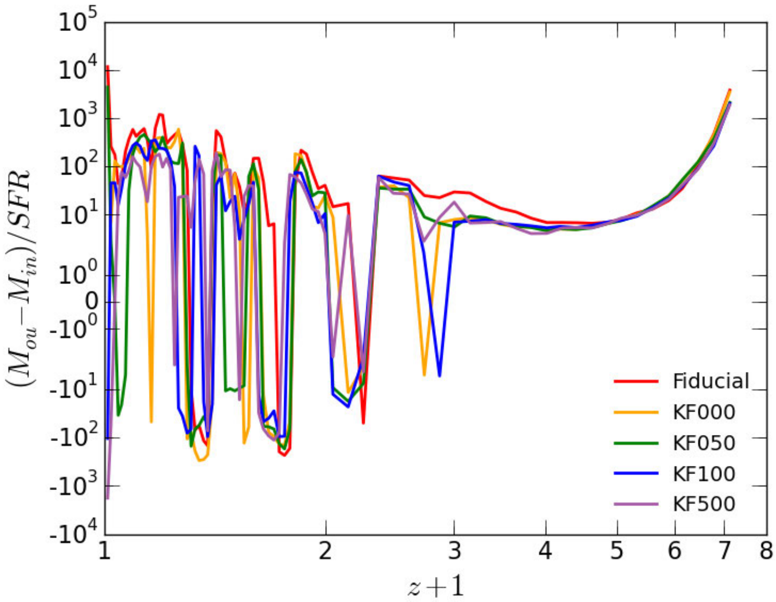

Figure 4.32: Cosmic evolution of the mass-loading factors. The lines indicate the mean values.

5 DISCUSSION

This study explores two different numerical kinetic AGN feedback models and their effect on a simulated galaxy cluster using the SPH code GADGET-3. Whereas the fiducial simulation implements the energy feedback in the radio-mode thermally, the new routine couples kinetic energy onto the gas. Two free parameters, f_{kin} which determines the energy available for kinetic feedback and v_{Wind} which determines the velocity increment of gas particles that receives kinetic feedback, of the new model are investigated. The other free parameters, ϵ_f and the wake-up call constant, have been found in previous studies. The results are compared to the fiducial simulation and all simulations are compared with theoretical and observational results.

The comparison of simulations using different values for v_{Wind} have shown that there is little difference between them (Fig. 4.10 and App. B.5). Thus it is less important what kinetic energy the gas particles receive, but that they receive it at all. This is the reasons why more attention was payed to the analyzes of the influence of f_{kin}.
A fundamental step to verify a AGN feedback scheme in cosmological simulations is to find out how well the $M_{BH} - M_*$ relation is reproduced. From Fig. 4.5, one can see that the simulations with the new kinetic AGN feedback produce slightly too massive SMBHs. Therefore the right parameter constellation that fits the relation has yet to be found. The high SMBHs masses are due to high accretion rates which are on average higher for the non-fiducial simulations as can be seen in Fig. B.3. From Fig. 4.3b it becomes clear that accretion rates are higher especially for SMBHs with masses $\geq 10^7\, M_\odot$. Since a higher accretion rate means more feedback energy (equ. 3.16), it comes as a surprise that the SFR (Fig. 4.11) is less quenched than in the fiducial simulation at redshifts $2 < z < 4$ approximately. During that redshift period, the number of SMBHs in the fiducial simulation increases more in the radio-mode and less in the quasar-mode as compared to the simulations with new kinetic AGN feedback (Tab. B.1). Since the thermal AGN feedback is the same for both simulations however, the difference must be caused by the SMBHs which are in the radio-mode. When looking at the stellar density distribution in Fig. B.5, it appears that the surplus in star formation seems to originate from the centres of subhalos. At this time the SMBHs in the BCG are are mainly in the radio-mode, where kinetic AGN feedback dominates. This means that the new kinetic AGN feedback module is less effective in quenching the SFR especially in the centres of subhalos. As the figures 4.18 and 4.30 show, does the new kinetic AGN feedback especially carry out high temperature gas through which the centre becomes cooler and more likely to form stars.

Since the main focus of this work is the concept study of a new AGN feedback scheme, the mass resolution is held low. Therefore all comparisons with theory

and observations have to be viewed with an critical eye. The low resolution does not permit a simulation of the real AGN jet propagation. Hence it is only attempted to capture the effect of the energy deposit of the mechanical jets from AGN at large scales.
As for the $M_{BH} - M_*$ relation, the $M_{BH} - \sigma_*$ relation showes too high SMBHs masses compared to both theoretical and observational findings. It is however interesting to see that there is a better agreement between the theoretical relation by Zubovas and King [195] then the observations. It is worthwhile to investigate the results of Zubovas and King [195] numerically and see if they can be reproduced.
For a long time numerical simulations overestimated the stellar mass fraction as can be seen in results of Borgani et al. [25]. With the AGN feedback implementations this is corrected to reasonable levels as shown in Fig. 4.14. The emission weighted temperatures for all simulated clusters are however too small. The reason could be the strong approximation used for the cooling function $\Lambda(T) \propto \sqrt{T}$.
When investigating the entropy profiles from the cluster centre, the simulations with new kinetic AGN feedback are closer to being cool-core, if the definition by Hahn et al. [87] is used. This indicates, that the new kinetic AGN feedback scheme could help to produce a diverse population of cool-core and non-cool-core clusters. This has so far proved to be quite a challenge for cosmological hydrodynamic simulations (Borgani and Kravtsov [26], and references therein).
Due to the low resolution, no morphology study is possible since all subhalos are not in a relaxed state [1].
This study reveals the challenges of devising numerical schemes for sub-resolution models, which must capture the physical processes given the numerical resolution.

1 If the offset between the most bound particle and the centre of mass of a subhalo is used as a proxy for determining the relaxation state.

6 CONCLUSION

This study presents a parameter study of a new routine for kinetic AGN feedback using the SPH code GADGET-3. Theoretical predictions by Churazov et al. [36] together with observations by Russell et al. [147] are used to model underlying sub-grid processes more realistically. The new model has a steady transition between the AGN radio- and quasar-mode, since the feedback processes are modeled as a function of accretion rate with respect to the Eddington-rate. Mechanical outflows are implemented as a one-time velocity increase which kicks a gas particle lying in a by-cone centred at the SMBH into the wind. Radiative feedback is implemented as thermal feedback in a spherically symmetric manner. Furthermore are free parameters of the model (e.g. α, ϵ_f) strictly linked to values inferred from observations. The most important findings are:

(i) The exact value of v_{Wind} which is imparted on a gas particles is less important than that they receive it at all.

(ii) The slope of simulated $M_{BH} - M_*$ relation is in good agreement with observations. The normalization however is too low since the new AGN feedback does not suppress accretion efficiently enough.

(iii) The new kinetic AGN feedback module is less effective in quenching the SFR especially in the centres of subhalos.

(iv) It is worthwhile to investigate the results of Zubovas and King [195] numerically and see if they can be reproduced.

(v) The new kinetic AGN feedback scheme can produce a diverse population of cool-core and non-cool-core clusters.

In future studies, more realistic AGN feedback routines will take the angular momentum of the accreted material into account which will lead to more realistic jet directions. Furthermore can the effect of a differentiation between FR-I and FR-II be studied. The current computational power does not allow to implement many of the missing small-scale physical processes within large-scale cosmological simulations Therefore more detailed advances are limited. Nevertheless, despite the crude approximations, the current AGN scheme agrees reasonable with observations and theory.

A

ADDITIONAL THEORY

A.1 BLACK HOLE HORIZONS

There are several important horizons/radii which have important implications for matter falling towards a BH. The most well known is the event horizon, which forms a boundary in spacetime beyond which events cannot affect an outside observer. Since there are four known, exact, BH solutions to the Einstein field equations, the definition of the event horizon depends on the type of BH one looks at.

Black hole type	Properties	Event horizons
Schwarzschild	Non-rotating, Uncharged	$R_H = \frac{2GM}{c^2}$
Reissner–Nordström	Non-rotating, Charged	$R_{H,\pm} = M \pm \sqrt{M^2 - Q^2}$
Kerr	Rotating, Uncharged	$R_{H,\pm} = M \pm \sqrt{M^2 - a^2}$
Kerr-Newman	Rotating, Charged	$R_{H,\pm} = M \pm \sqrt{M^2 - a^2 - Q^2}$

Table A.1: Event horizons for the four different types of BH. The gravitational constant is symbolised as G, the speed of light as c, M stands for the BH mass, a for the BH specific angular momentum ($a = |J|/M$), and Q is the electric charge

A.2 CONVERSION EFFICIENCY FOR BH ACCRETION

As already described in Sec. 2.3, the accretion phenomenon is very complex and involves a multitude of different processes which are dominant at different radii and which would all need to be taken into account for a correct description. To give a complete description of black hole accretion is out of the scope of this thesis. However a first glimpse into the topic is provided, with the goal to calculate the rest-mass to luminosity conversion efficiency defined as $\eta \equiv L/(\dot{M}c^2)$. For simplicity a stationary (not moving w.r.t. accreted matter), non-rotating black hole is considered. The environment around a BH can be divided into several regions defined by the physical conditions. The conditions in the gas outside the accretion radius (given by equ. 2.9) determines the rate of accretion. At radii $\leq r_{acc}$, the properties of the gas are affected by heating and radiative cooling. Here, the gravitational potential energy can be assumed small compared to the thermal or kinetic energy of the gas. The radius r_{rel},

$$r_{rel} \approx (T_\infty)/T_{red} \approx m_p/m_e r_g \approx 2 \times 10^3 r_g \,, \tag{A.1}$$

with m_p the proton rest mass, m_e the electron rest mass, and r_g is the gravitational/Schwarzschild radius, describes the distance of to the black hole, at which electrons become relativistic. At radii $\leq r_{rel}$ the equipartition assumption implies

that the magnetic energy density, kinetic energy density, turbulent energy density, and gravitational energy density are approximately in equipartition.
To describe gravitational effects near a non-rotating BH of mass M, the Schwarzschild line element in standard coordinates is used:

$$ds^2 = -(1 - \frac{r_g}{r})c^2dt^2 + (1 - \frac{r_g}{r})^{-1}dr^2 + r^2(d\theta^2 + sin^2\theta d\phi^2)\,. \tag{A.2}$$

The motion of the in-falling gas is described by $u^\mu = dx^\mu/ds$, the gas 4-velocity. Since spherical accretion is assumed $u^\theta = u^\phi = 0$. The radial component of 4-velocity u^r, and the baryon density n of the gas have to fulfill the conservation of mass due to the continuity equation:

$$4\pi r^2 nu = constant\,. \tag{A.3}$$

To simplify more, only the gas lying inside $r_{rel} < r < r_{acc}$ is analyzed. In this region for densities $n_\infty \geq 10^5\,cm^{-3}$, bremsstrahlung and cyclotron cooling are most important. The inflow velocity can be found by starting with the Euler equation for a steady flow, gravity as the only external force, and using spherical coordinates:

$$u\frac{du}{dr} + \frac{1}{\rho}\frac{dP}{dr} + \frac{GM}{r^2} = 0\,. \tag{A.4}$$

Black hole accretion can be approximately treated in the adiabatic domain, since the central temperature becomes high enough for the radiation field to start disintegrating the atomic nuclei, leading to a neglectable loss of radiation, so that $\gamma = 1 + 1/n < 1$. The polytropic relation reads:

$$P = K\rho^\gamma,\, K = constant\,. \tag{A.5}$$

The gradients of P and ρ have the following relation,

$$\frac{dP}{dr} = \frac{dP}{d\rho}\frac{d\rho}{dr} = c_s^2\frac{d\rho}{dr}\,. \tag{A.6}$$

To find the velocity u at a distance r, we need to integrate equ. A.4, which can be done with the help of the relation $dP = K\gamma\rho^{\gamma-1}d\rho$ and $K\gamma\rho^{\gamma-1} = \gamma P/\rho = c_s^2$. This results in the Bernoulli integral:

$$\frac{u^2}{2} + \frac{c_s^2}{\gamma - 1} - \frac{GM}{r} = \frac{c_s^2}{2} + \frac{c_s^2}{\gamma_s - 1} - \frac{GM}{r_s}\,. \tag{A.7}$$

Using $2c_s^2 = GM/r_s$ and re-grouping one gets:

$$u^2 = 2c_s^2\left(\frac{1}{\gamma_s - 1} - \frac{1}{\gamma - 1} - \frac{3}{2}\right) + \frac{2GM}{r}\,. \tag{A.8}$$

Hence, the flow velocity u approaches free fall as $r \to 0$,

$$u \sim \left(\frac{2GM}{r}\right)^{1/2}\,. \tag{A.9}$$

The conservation of mass, which is ensured by the continuity equation, implies

$$n = n_0 \left(\frac{r_{acc}}{r}\right)^{3/2} . \tag{A.10}$$

For an adiabatic flow we also have

$$T \propto n^{\gamma-1} \sim T_0 \frac{r_{acc}}{r} . \tag{A.11}$$

Assuming that the cooling is purely radiative and dominated by thermal bremsstrahlung, we can calculate the luminosity as

$$L = \int_{r_g}^{r_{acc}} F_{diss} 4\pi r^2 dr = 4\pi \int_{r_g}^{r_{acc}} j_{br}(T) 4\pi r^2 dr , \tag{A.12}$$

where the energy dissipated per unit area of the accretion sphere, F_{diss}, equal to the volume emissivity, $4\pi j_{br}$, which is can be approximated by

$$4\pi j_{br} \cong 2 \times 10^{-27} N_e^2 T_e^{1/2}\, erg\, s^{-1}\, cm^{-3} , \tag{A.13}$$

for a gas of cosmic abundances with electron temperature T_e and electron density N_e. The lower limit of integration can be taken as the Schwarzschild radius of the BH, since beyond this the accreting material cannot emit. The upper limit is the accretion radius beyond which the gas is relatively uninfluenced by gravity. Since $r_{acc} \gg r_g$ and the integrand is a decreasing function of r, we can let the upper limit tend to infinity. Integrating equ. A.12 by substituting equ. A.10 and equ. A.11 gives

$$L \sim 2.5 \times 10^{-27} r_g^{-1/2} r_{acc}^{7/2} N_0^2 T_0^{1/2}\, erg\, s^{-1} . \tag{A.14}$$

substituting $r_g = 2GM/c^2$ for a spherical BH accretion, and using equ. 2.9 gives

$$L \sim 4 \times 10^{32} M_8^3 T_8^{-3} N_0^2\, erg\, s^{-1} , \tag{A.15}$$

with $M_8 = M/(10^8 M_\odot)$ and $T_8 = T/10^8$. Finally with the luminosity L at hand, only the accretion rate $\dot{M}$, given in equ. 2.8 needs to be found. For convenience it can be re-written as

$$\dot{M} = \pi G^2 M_{BH}^2 \frac{\rho_\infty}{c_{s,\infty}^3} \approx 4 \times 10^{-5} M_8^2 T_8^{-3/2} \frac{n_\infty}{c_{s,\infty}} M_\odot . \tag{A.16}$$

Reasonable properties of the accreted ISM at far distances are: $n_\infty = 1\, cm^{-3}$, $T_\infty = 10^4\, K$. The adiabatic sound speed $c_{s,\infty}$ can be found through

$$c_{s,\infty} = \left(\frac{5kT_\infty}{3\overline{m}}\right)^{1/2} , \tag{A.17}$$

where $\overline{m}$ is the mean molecular weight, which can be approximated as $2.33 m_H$ for the ISM. In the case of a black hole with $M_{BH} = 10^8 M_\odot$, $\eta = 4.3 \times 10^{-6}$. In Fig. A.1 is $\eta_{max} = L_{Edd}/(\dot{M}c^2)$ shown.

Thus the assumptions made are neglecting a large part of luminosity sources (such as Thomson-, Compton-, and inverse Compton scattering, synchrotron radiation, and pair production/annihilation radiation). Furthermore is spherically symmetric accretion less efficient than disk accretion models. The interested reader is given a more detailed account on this topic by [77].

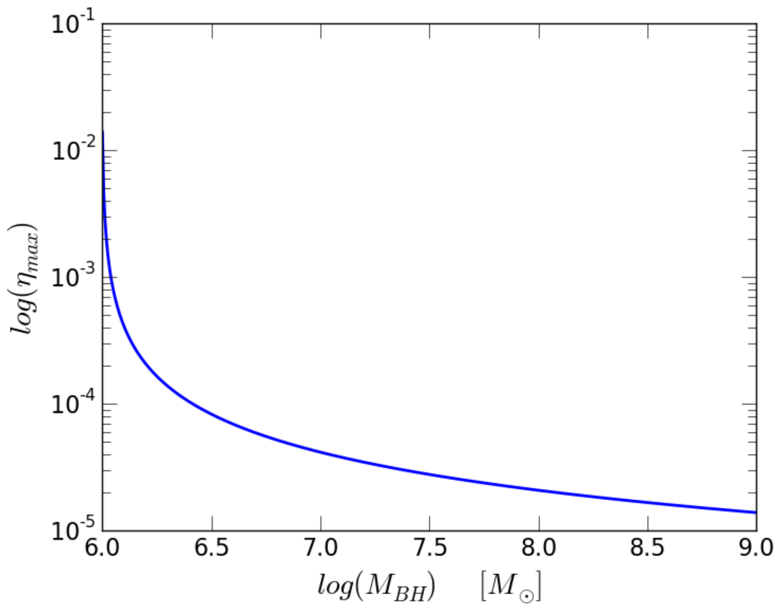

Figure A.1: Shown is the dependency of the maximum rest-mass to luminosity conversion efficiency on the BH mass.

A.3 IMAGES OF AGNS

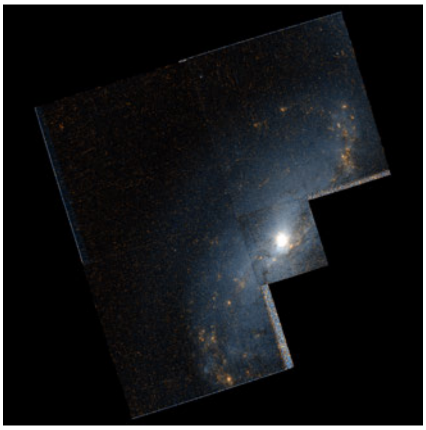

(a) Image taken with HST of NGC 3227, which is a Seyfert 1 galaxy.

(b) Image of NGC 2992 (left side), which is a Seyfert 2 galaxy.

(c) Image of NGC 7319, which is member of Stephan's galaxy Quintet. It bears a QSO in it's center, which was dicovered by the Chandra space telescope.

(d) Image of NGC 5128, which is a multicolour composite of: ESO/WFI (optical), MPIfR/ESO/APEX (submillimeter), and NASA/CXC/CfA (X-ray)

(e) Shown is M87, which has a LINER nucleus, observed with HST.

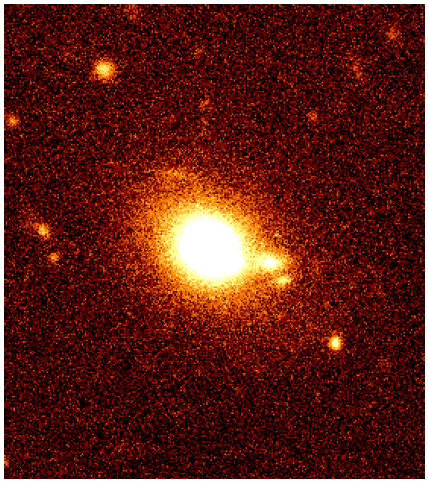

(f) Image of BL Lac object H0323+02 obtained with ESO's NTT

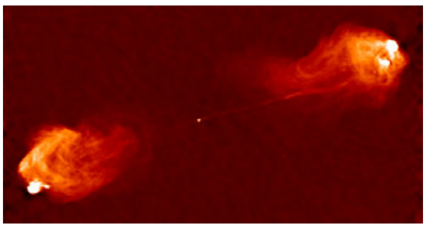

(g) This image shows the radio emission from relativistic streams of high energy particles generated by the quasar of the FRII galaxy Cygnus A.

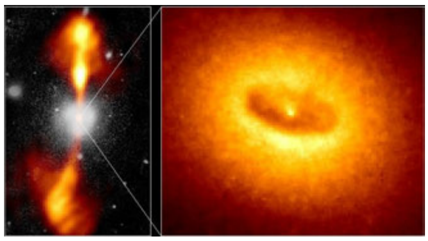

(h) The LINER harboring NGC 4261, shown in a ground-based optical/radio image (left) and HST image of gas and dust (right).

A.4 WAKE-UP CALL

The wake-up switch counteracts the problems, arising from individual times steps of particles. It was implemented into GADGET-3 by Pakmor et al. [132]. Having individual time steps for particles, which depend only on the local conditions near the particle, greatly reduces the computational costs. However if very fast particles, with small time steps, run into a region in which particles have longer time steps, they can run through them unnoticed.
As this behaviour leads to unphyiscal results, a 'wake-up' switch is impletmented, which activates inactive particles as other particles approach them which evolve on much shorter time steps. Time step lengths for individual particles are computed in every time step they are active, according to

$$\Delta t_i = \frac{Ch_i}{u_i^{sig}} \tag{A.18}$$

where C is the Courant factor, h_i is the smoothing length of the particle and u_i^{sig} the maximum singal velocity. The maximum signal velocity is computed between the active particle i and all its neighbour particles j within the entire kernel. To find differences in signal velocities within the kernel, GADGET-3 employs a condition during the hydrodynamical force computation by evaluating

$$u_{ij}^{sig} > f_w u_j^{sig} \tag{A.19}$$

with the tolerance factor f_w corresponding to a wake-up triggering criterion, which captures sudden changes in the pairwise signal velocity. The pairwise singal velocity u_{ij}^{sig} (first introduced by Monaghan [126]) determines the strength of artificial viscosity and directly includes a quantitative measure of particles disorder. It is calculated via

$$u_{ij}^{sig} = c_i^s + c_j^s - \beta\mu_{ij} \tag{A.20}$$

where c^s s is the sound speed of the particles and $\mu_{ij} = u_{ij} \cdot x_{ij}/x_{ij}$, with x_{ij} the distance between particle i and the neighbouring particles in the kernel j, the relative velocity u_{ij} and with a commonly chosen pre-factor of $\beta = 3$. We have adopted a tolerance factor of $f_w = 4.1$ for all simulations except for KF000, which results in a reduction of SFR.

A.5 SHRINKING SPHERE METHOD

It is important to choose carefully the halo centre, especially as the haloes are not spherically symmetric. The centre of each halo is determined using an iterative technique in which the centre of mass of particles within a shrinking sphere is computed recursively until a convergence criterion is met. At each step of the iteration, the centre of the sphere is reset to the last computed barycentre and the radius of the sphere is reduced by 2.5 per cent. The iteration is stopped when a specified number of particles (typically either 1000 particles or 1 percent of the particles within the high-resolution region, whichever is smaller) is reached within the sphere. Halo centres identified with this procedure are quite independent of the parameters chosen to initiate the iteration, provided that the initial sphere is large enough to encompass a large fraction of the system. In a multi-component system, such as a dark halo with substructure, this procedure isolates the densest region within the largest subcomponent. In more regular systems, the centre so obtained is in good agreement with centres obtained by weighing the centre of mass by the local density or gravitational potential of each particle. We have explicitly checked that none of the results presented here are biased by our particular choice of centring procedure.

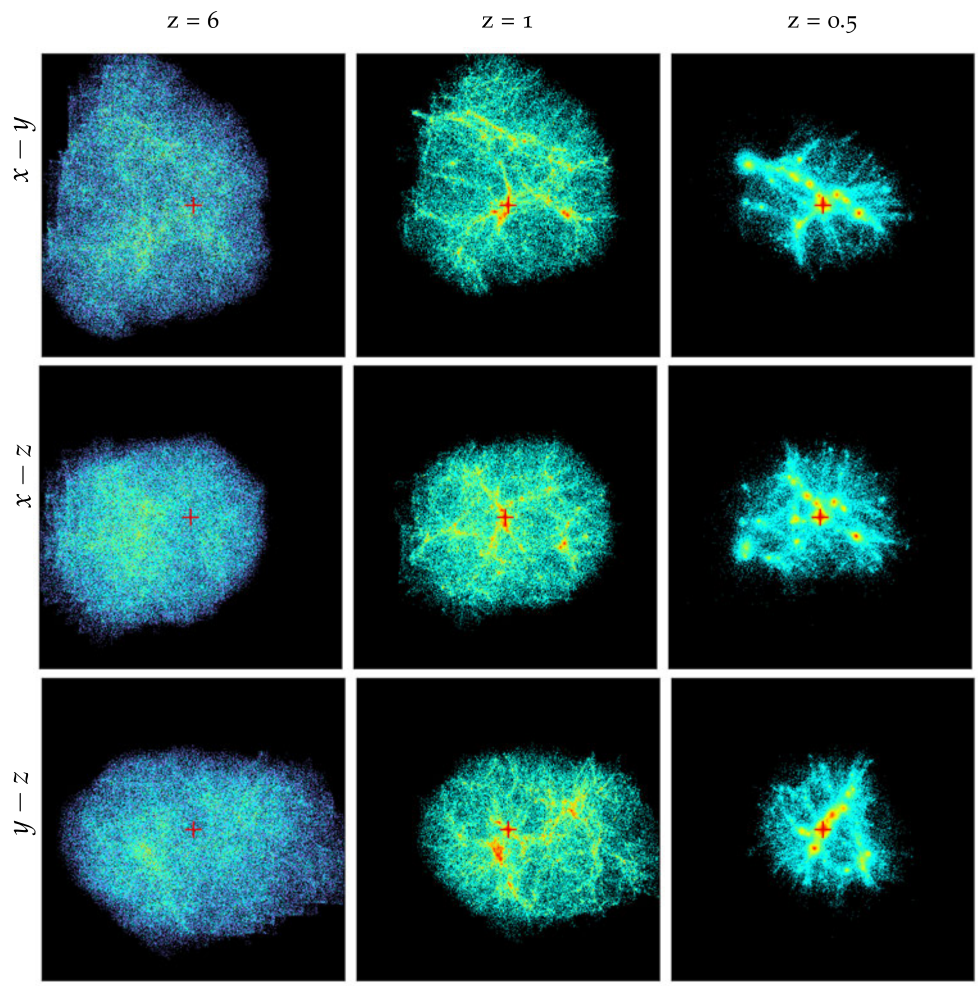

Figure A.2: Demonstration of the shrinking sphere method on the fiducial simulation for three different redshifts.

B

ADDITIONAL SIMULATION RESULTS

B.1 EDDINGTON RATIO

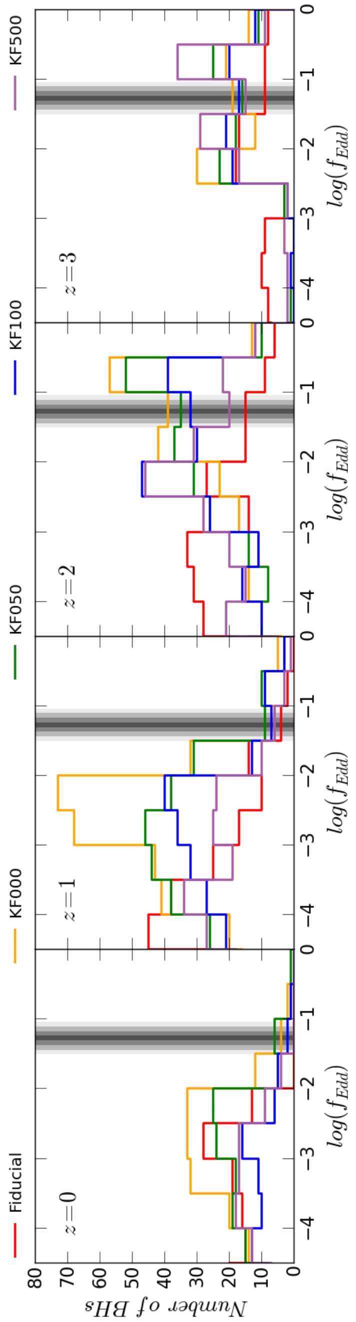

Figure B.1: Eddington ratio distributions for different redshifts $z = 0, 1, 2, 3$. The vertical grey colour gradient visualises the smooth distinction between radio- and quasar-mode adopted in the model.

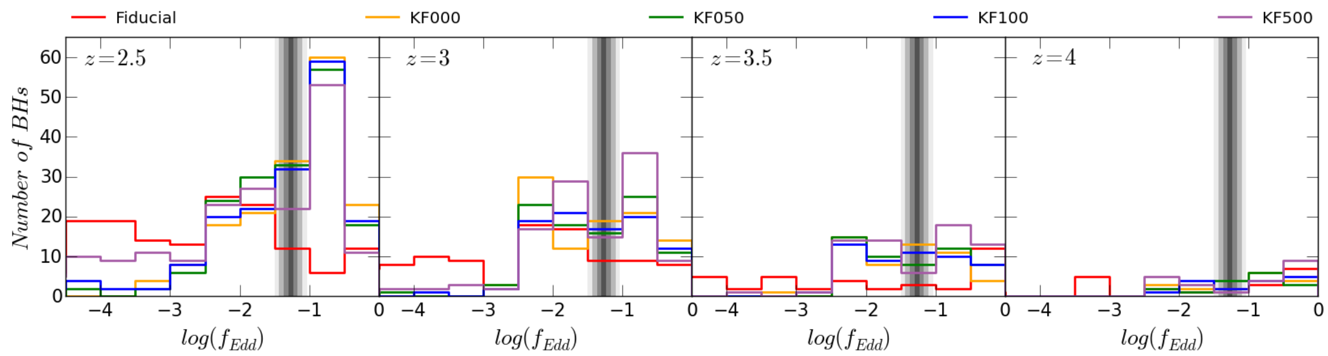

Figure B.2: Eddington ratio distributions for different redshifts $z = 2.5, 3, 3.5, 4$. The vertical grey colour gradient visualises the smooth distinction between radio- and quasar-mode adopted in the model.

	Z	*Fiducial*	*KF*000	*KF*050	*KF*100	*KF*500
radio-mode	4	11	5	4	5	9
	3.5	32	28	29	26	32
	3	92	52	54	49	62
	2.5	165	62	74	73	120
quasar-mode	4	10	12	12	11	13
	3.5	16	24	24	26	35
	3	21	47	43	45	56
	2.5	23	110	100	101	80

Table B.1

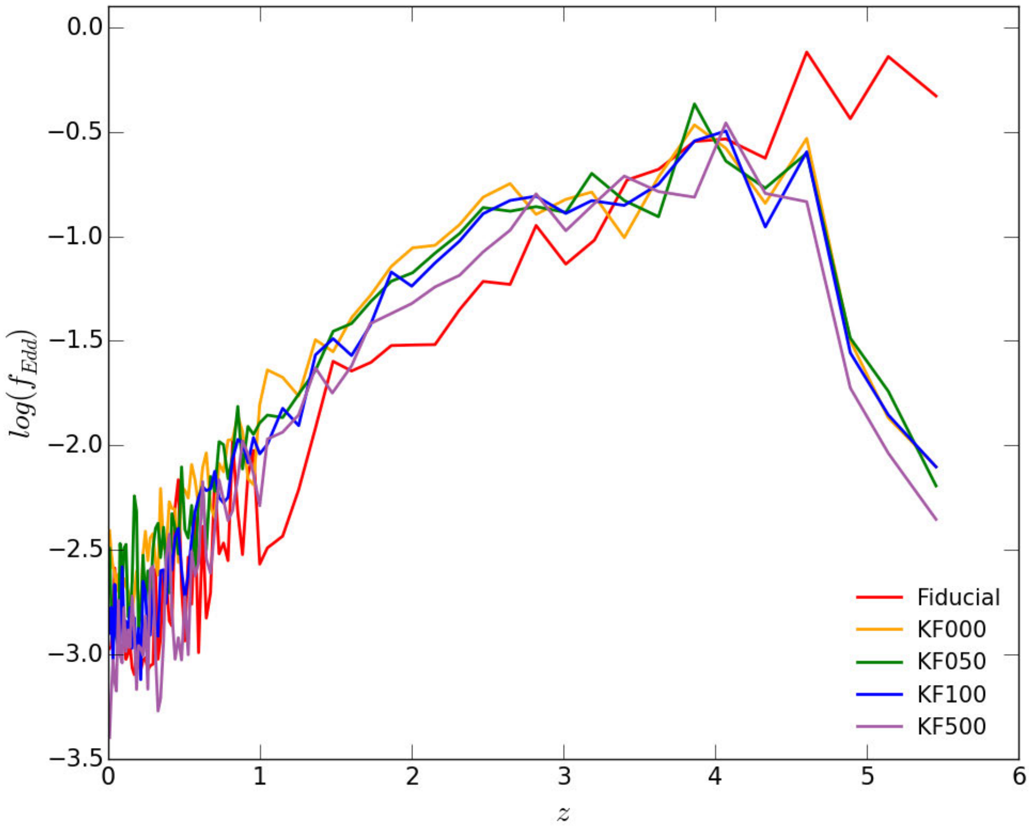

Figure B.3: Redshift evolution of the mean Eddington-ratios taking all SMBHs into account.

B.2 RADIAL PROFILES AT $z = 2 - 4$

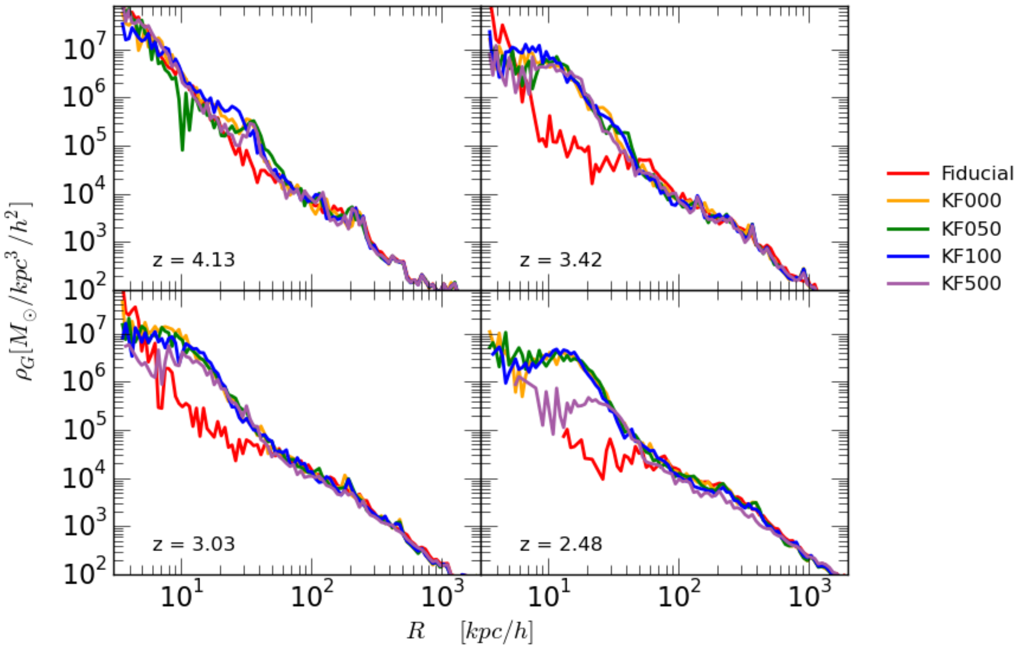

Figure B.4: Radial profiles of stellar density around the BCG centre at four different redshifts: $z = 4.13$ (top-left panel), $z = 3.42$ (top-right), $z = 3.03$ (bottom-left), and $z = 2.48$ (bottom-right).

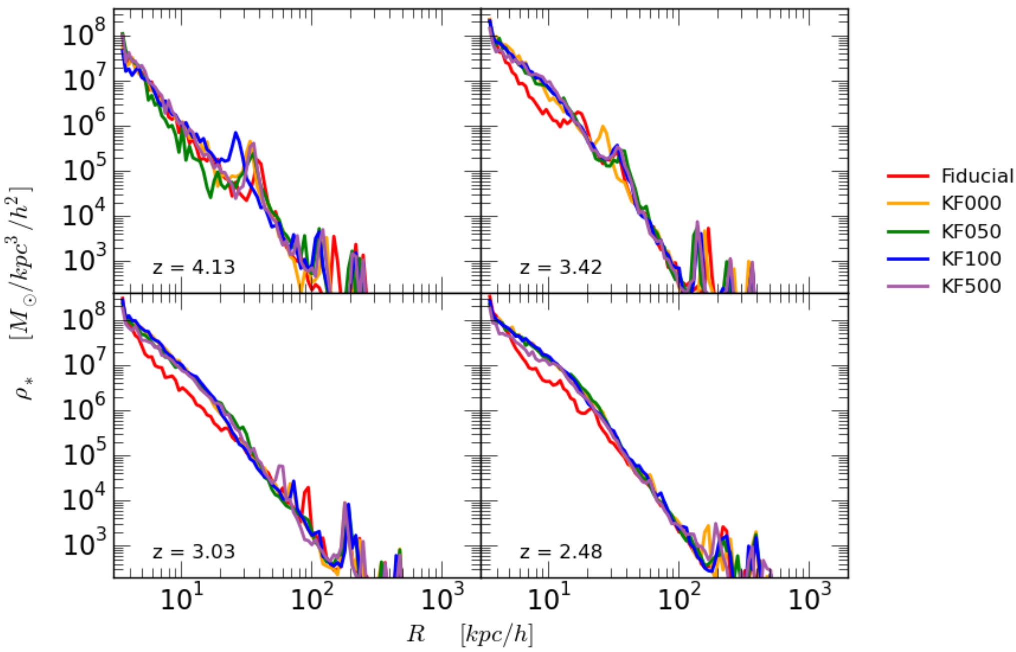

Figure B.5: Radial profiles of stellar density around the BCG centre at four different redshifts: $z = 4.13$ (top-left panel), $z = 3.42$ (top-right), $z = 3.03$ (bottom-left), and $z = 2.48$ (bottom-right).

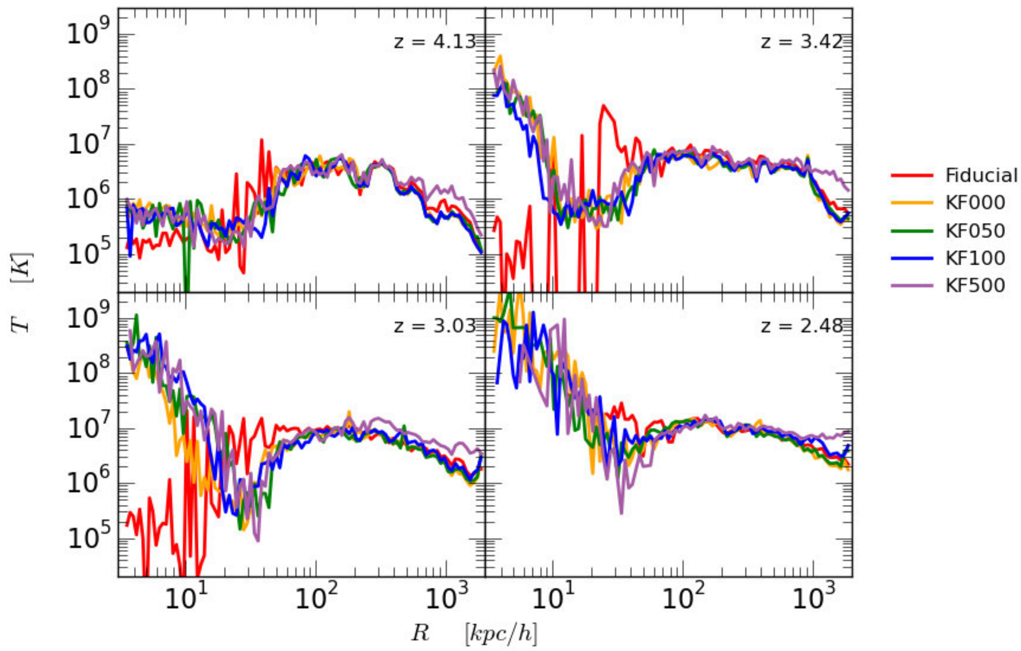

Figure B.6: Radial profiles of gas temperature around the BCG centre at four different redshifts: $z = 4.13$ (top-left panel), $z = 3.42$ (top-right), $z = 3.03$ (bottom-left), and $z = 2.48$ (bottom-right).

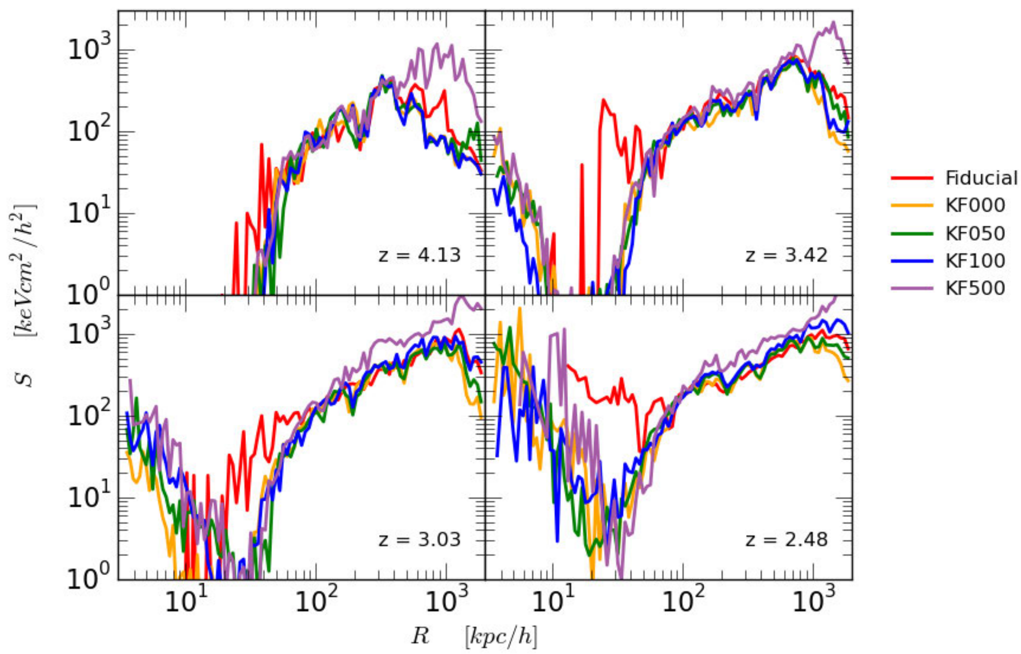

Figure B.7: Radial profiles of stellar density around the BCG centre at four different redshifts: $z = 4.13$ (top-left panel), $z = 3.42$ (top-right), $z = 3.03$ (bottom-left), and $z = 2.48$ (bottom-right).

B.3 BCG PROFILES

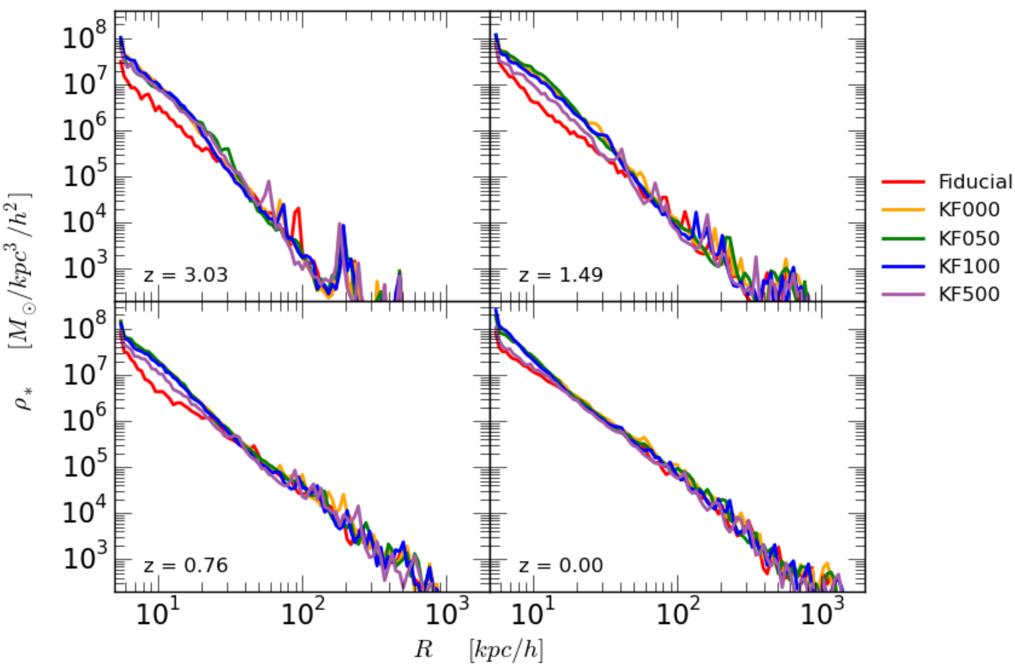

Figure B.8: Radial profiles of stellar density around the BCG centre at four different redshifts: $z = 3$ (top-left panel), $z = 1.49$ (top-right), $z = 0.76$ (bottom-left), and $z = 0$ (bottom-right).

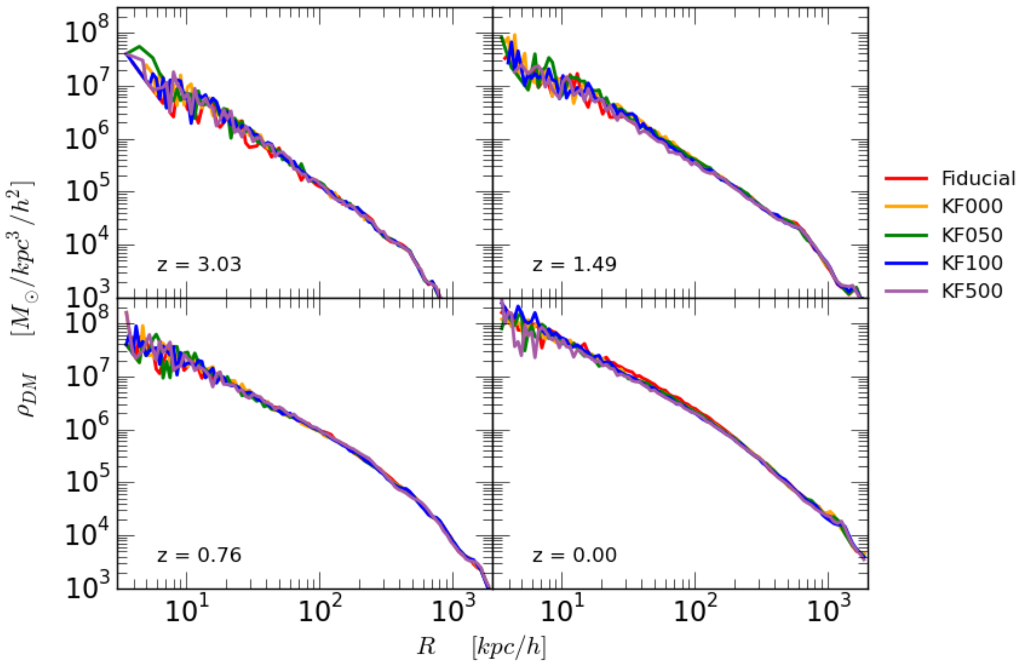

Figure B.9: Radial profiles of dark matter density around the BCG centre at four different redshifts: $z = 3$ (top-left panel), $z = 1.49$ (top-right), $z = 0.76$ (bottom-left), and $z = 0$ (bottom-right).

B.4 PHASE DIAGRAM

Here is the evolution of the phase diagram of KF500 with additional 2D maps shown. Particles of prominent features are tracked back in time. The visualization makes a connection between the gas particles which populate some of the characteristic regions in the phase diagram discussed above are shown in Sec. 4.4, to their position in space. The starting redshift from which particles are tracked back is $z = 2.65$. At that time green particles population the fast-cooling zone. They have been brought there due to thermal energy feedback of stars, supernovae, and SMBHs. Coloured in red are particles of a high temperature bump at overdensity of around ~ -2. This feature is the combined effect of a predominant thermal AGN feedback and a minor kinetic AGN feedback. Blue gas particles have received the kinetic AGN feedback and are carried outside of their host galaxies due to the wind velocity.

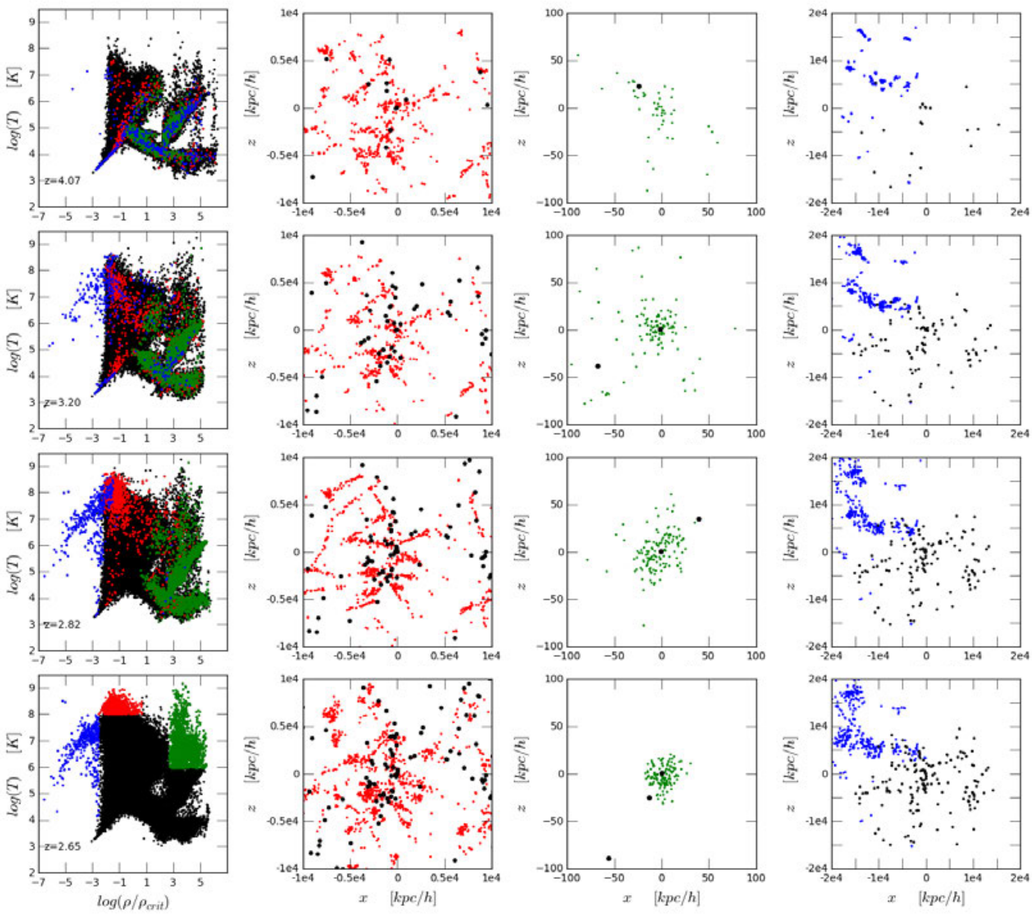

B.5 COMPARING MECHANICAL OUTFLOW VELOCITIES

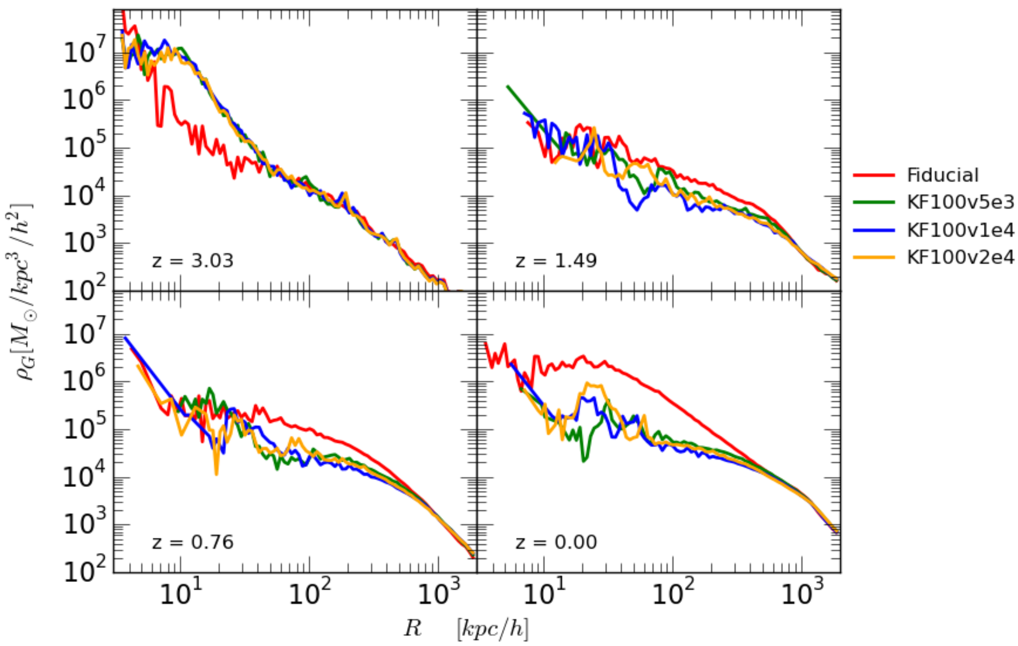

Figure B.10: Radial profiles of gas density around the BCG centre at four different redshifts: $z = 3$ (top-left panel), $z = 1.49$ (top-right), $z = 0.76$ (bottom-left), and $z = 0$ (bottom-right).

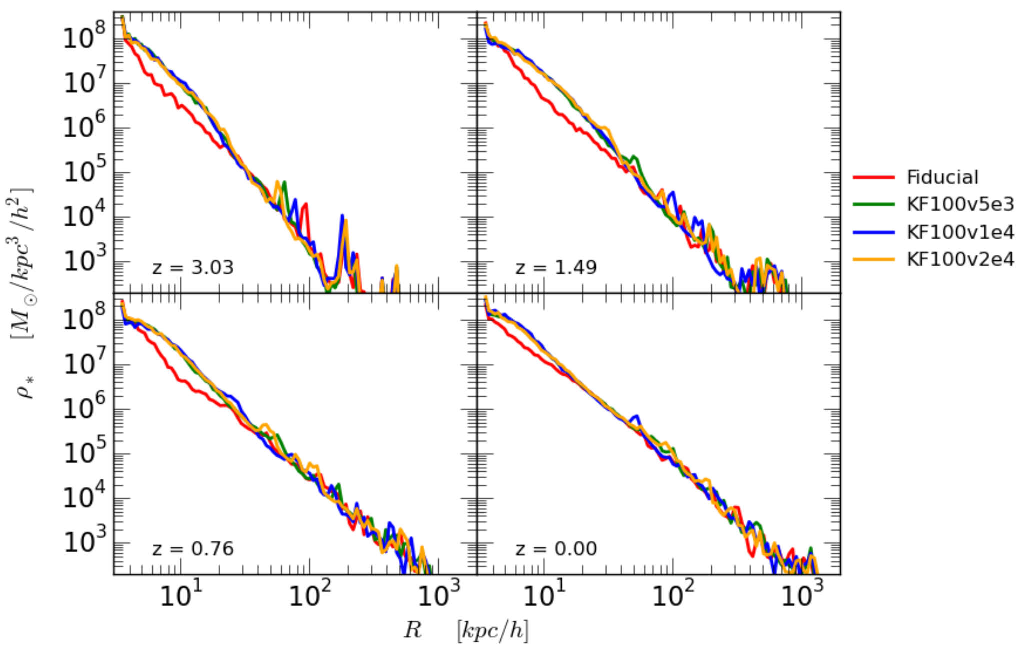

Figure B.11: Radial profiles of stellar density around the BCG centre at four different redshifts: $z = 3$ (top-left panel), $z = 1.49$ (top-right), $z = 0.76$ (bottom-left), and $z = 0$ (bottom-right).

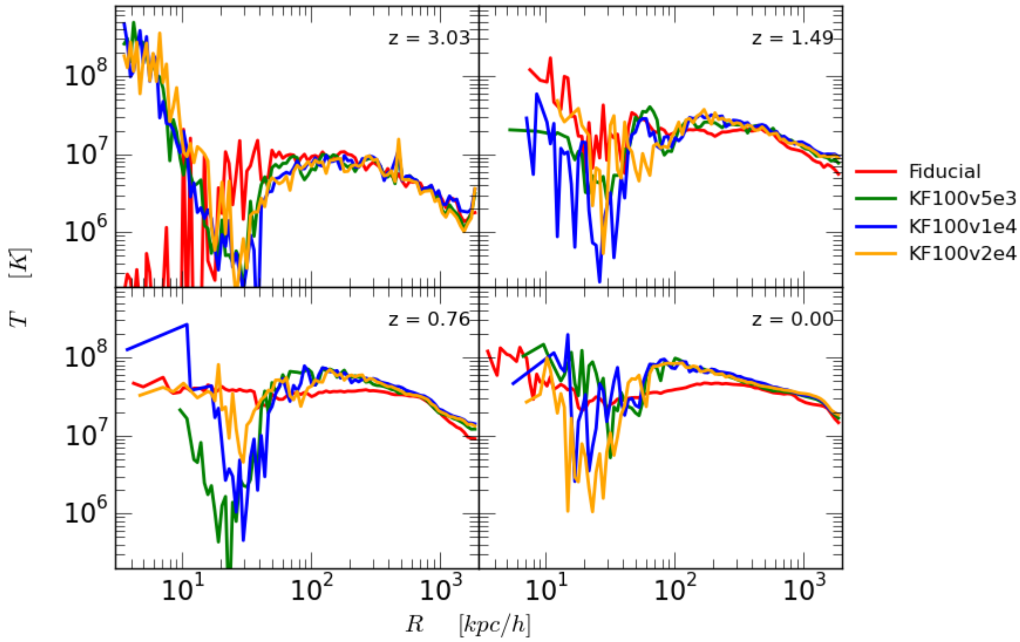

Figure B.12: Radial profiles of gas temperature around the BCG centre at four different redshifts: $z = 3$ (top-left panel), $z = 1.49$ (top-right), $z = 0.76$ (bottom-left), and $z = 0$ (bottom-right).

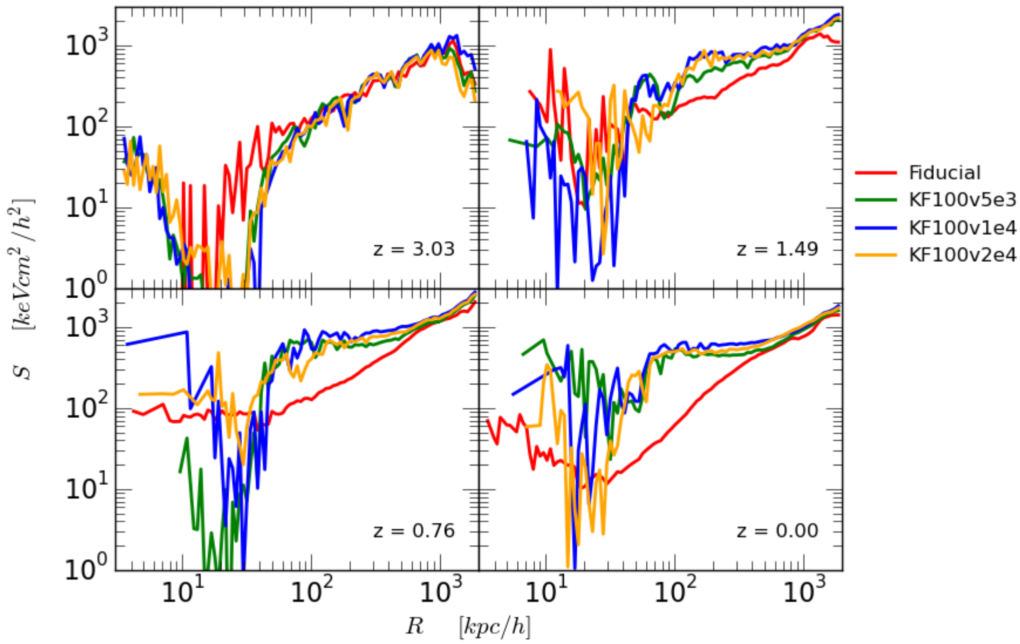

Figure B.13: Radial profiles of gas entropy around the BCG centre at four different redshifts: $z = 3$ (top-left panel), $z = 1.49$ (top-right), $z = 0.76$ (bottom-left), and $z = 0$ (bottom-right).

BIBLIOGRAPHY

[1] SJ Aarseth and F Hoyle. "Dynamical evolution of clusters of galaxies, I." In: 126.3 (1963), pp. 223–255.

[2] Sverre J Aarseth and Sverre Johannes Aarseth. *Gravitational N-body simulations: tools and algorithms*. Cambridge University Press, 2003.

[3] PAR Ade, N Aghanim, M Arnaud, M Ashdown, J Aumont, C Baccigalupi, AJ Banday, RB Barreiro, JG Bartlett, N Bartolo, et al. "Planck 2015 results-XIII. Cosmological parameters." In: *Astronomy & Astrophysics* 594 (2016), A13.

[4] Hannes Alfvén and N Herlofson. "Cosmic radiation and radio stars." In: *Physical Review* 78.5 (1950), p. 616.

[5] Robert Antonucci. "Unified models for active galactic nuclei and quasars." In: *Annual review of astronomy and astrophysics* 31 (1993), pp. 473–521.

[6] W Baade and R Minkowski. "On the Identification of Radio Sources." In: *The Astrophysical Journal* 119 (1954), p. 215.

[7] Paramita Barai, Giuseppe Murante, Stefano Borgani, Massimo Gaspari, Gian Luigi Granato, Pierluigi Monaco, and Cinthia Ragone-Figueroa. "Kinetic AGN feedback effects on cluster cool cores simulated using SPH." In: 461.2 (2016), pp. 1548–1567.

[8] Josh Barnes and Piet Hut. "A hierarchical O (N log N) force-calculation algorithm." In: *nature* 324.6096 (1986), pp. 446–449.

[9] Matthew R Bate, Ian A Bonnell, and Nigel M Price. "Modelling accretion in protobinary systems." In: 277.2 (1995), pp. 362–376.

[10] Giuseppina Battaglia, Amina Helmi, Heather Morrison, Paul Harding, Edward W Olszewski, Mario Mateo, Kenneth C Freeman, John Norris, and Stephen A Shectman. "The radial velocity dispersion profile of the Galactic halo: constraining the density profile of the dark halo of the Milky Way." In: 364.2 (2005), pp. 433–442.

[11] Alexander M Beck, Giuseppe Murante, Alexander Arth, R-S Remus, Adelheid F Teklu, Julius MF Donnert, Susana Planelles, Marcus C Beck, Pascal Förster, Maximilian Imgrund, et al. "An improved SPH scheme for cosmological simulations." In: 455.2 (2016), pp. 2110–2130.

[12] Robert H Becker, Richard L White, and David J Helfand. "The FIRST survey: faint images of the radio sky at twenty centimeters." In: *The Astrophysical Journal* 450 (1995), p. 559.

[13] Volker Beckmann and Chris Shrader. *Active galactic nuclei*. John Wiley & Sons, 2013.

[14] Mitchell C Begelman and Martin J Rees. "The fate of dense stellar systems." In: 185.4 (1978), pp. 847–860.

[15] Mitchell C Begelman, Marta Volonteri, and Martin J Rees. "Formation of supermassive black holes by direct collapse in pre-galactic haloes." In: *Monthly Notices of the Royal Astronomical Society* 370.1 (2006), pp. 289–298.

[16] Ralf Bender, John Kormendy, Gary Bower, Richard Green, Jens Thomas, Anthony C Danks, Theodore Gull, JB Hutchings, CL Joseph, ME Kaiser, et al. "HST STIS spectroscopy of the triple nucleus of M31: two nested disks in keplerian rotation around a supermassive black hole." In: *The Astrophysical Journal* 631.1 (2005), p. 280.

[17] PN Best, G Kauffmann, TM Heckman, J Brinchmann, S Charlot, Ž Ivezić, and SDM White. "The host galaxies of radio-loud active galactic nuclei: mass dependences, gas cooling and active galactic nuclei feedback." In: 362.1 (2005), pp. 25–40.

[18] James Binney and Scott Tremaine. *Galactic dynamics*. Princeton university press, 2011.

[19] Roger D Blandford and Roman L Znajek. "Electromagnetic extraction of energy from Kerr black holes." In: 179.3 (1977), pp. 433–456.

[20] JG Bolton, GJ Stanley, and OB Slee. "Positions of three discrete sources of galactic radio-frequency radiation." In: *Classics in Radio Astronomy*. Springer, 1949, pp. 239–241.

[21] A Bonafede, K Dolag, F Stasyszyn, G Murante, and S Borgani. "A non-ideal magnetohydrodynamic gadget: simulating massive galaxy clusters." In: 418.4 (2011), pp. 2234–2250.

[22] HJ Bondi. "On spherically symmetrical accretion." In: 112.2 (1952), pp. 195–204.

[23] Hermann Bondi and Fred Hoyle. "On the mechanism of accretion by stars." In: 104.5 (1944), pp. 273–282.

[24] CM Booth and Joop Schaye. "Cosmological simulations of the growth of supermassive black holes and feedback from active galactic nuclei: method and tests." In: 398.1 (2009), pp. 53–74.

[25] S Borgani, G Murante, V Springel, A Diaferio, K Dolag, L Moscardini, G Tormen, L Tornatore, and P Tozzi. "X-ray properties of galaxy clusters and groups from a cosmological hydrodynamical simulation." In: *Monthly Notices of the Royal Astronomical Society* 348.3 (2004), pp. 1078–1096.

[26] Stefano Borgani and Andrey Kravtsov. "Cosmological simulations of galaxy clusters." In: *Advanced Science Letters* 4.2 (2011), pp. 204–227.

[27] Stefano Borgani, Klaus Dolag, Giuseppe Murante, L-M Cheng, Volker Springel, Antonaldo Diaferio, Lauro Moscardini, Giuseppe Tormen, Luca Tornatore, and Paolo Tozzi. "Hot and cooled baryons in smoothed particle hydrodynamic simulations of galaxy clusters: physics and numerics." In: 367.4 (2006), pp. 1641–1654.

[28] Kenneth W Cavagnolo, Megan Donahue, G Mark Voit, and Ming Sun. "Intracluster medium entropy profiles for a Chandra archival sample of galaxy clusters." In: *The Astrophysical Journal Supplement Series* 182.1 (2009), p. 12.

[29] Renyue Cen and Jeremiah P Ostriker. "Where are the baryons?" In: *The Astrophysical Journal* 514.1 (1999), p. 1.

[30] Thomas Chrowder Chamberlin. "On a possible function of disruptive approach in the formation of meteorites, comets, and nebulae." In: *The Journal of Geology* 9.5 (1901), pp. 369–392.

[31] G Chartas, WN Brandt, and SC Gallagher. "XMM-Newton reveals the quasar outflow in PG 1115+ 080." In: *The Astrophysical Journal* 595.1 (2003), p. 85.

[32] Ena Choi, Jeremiah P Ostriker, Thorsten Naab, and Peter H Johansson. "Radiative and Momentum-based Mechanical Active Galactic Nucleus Feedback in a Three-dimensional Galaxy Evolution Code." In: *The Astrophysical Journal* 754.2 (2012), p. 125.

[33] Ena Choi, Thorsten Naab, Jeremiah P Ostriker, Peter H Johansson, and Benjamin P Moster. "Consequences of mechanical and radiative feedback from black holes in disc galaxy mergers." In: 442.1 (2014), pp. 440–453.

[34] Ena Choi, Jeremiah P Ostriker, Thorsten Naab, Ludwig Oser, and Benjamin P Moster. "The impact of mechanical AGN feedback on the formation of massive earlytype galaxies." In: 449.4 (2015), pp. 4105–4116.

[35] E Churazov, W Forman, C Jones, and H Bohringer. "Asymmetric, arc minute scale structures around NGC 1275." In: *Astr.Ap.* 356 (2000), pp. 788–794.

[36] E Churazov, S Sazonov, R Sunyaev, W Forman, C Jones, and H Böhringer. "Supermassive black holes in elliptical galaxies: switching from very bright to very dim." In: 363.1 (2005), pp. L91–L95.

[37] Francoise Combes, Gary Mamon, and Vassilis Charmandaris. "Dynamics of Galaxies: From the Early Universe to the Present." In: *Publications of the Astronomical Society of the Pacific* 112.769 (2000), p. 423. URL: http://stacks.iop.org/1538-3873/112/i=769/a=423.

[38] JJ Condon, WD Cotton, EW Greisen, QF Yin, RA Perley, GB Taylor, and JJ Broderick. "The NRAO VLA sky survey." In: *The Astronomical Journal* 115.5 (1998), p. 1693.

[39] James N Connelly, Martin Bizzarro, Alexander N Krot, Åke Nordlund, Daniel Wielandt, and Marina A Ivanova. "The absolute chronology and thermal processing of solids in the solar protoplanetary disk." In: *Science* 338.6107 (2012), pp. 651–655.

[40] Tiago Costa, Debora Sijacki, Michele Trenti, and Martin G Haehnelt. "The environment of bright QSOs at z 6: star-forming galaxies and X-ray emission." In: 439.2 (2014), pp. 2146–2174.

[41] D Michael Crenshaw, Steven B Kraemer, and Ian M George. "Mass loss from the nuclei of active galaxies." In: *Annual Review of Astronomy and Astrophysics* 41.1 (2003), pp. 117–167.

[42] Darren J Croton, Volker Springel, Simon DM White, Gabriella De Lucia, Carlos S Frenk, Liang Gao, Adrian Jenkins, Guinevere Kauffmann, JF Navarro, and Naoki Yoshida. "The many lives of active galactic nuclei: cooling flows, black holes and the luminosities and colours of galaxies." In: 365.1 (2006), pp. 11–28.

[43] Heber Doust Curtis, William Wallace Campbell, Joseph Haines Moore, Ralph Elmer Wilson, and William Hammond Wright. *Studies of the Nebulae: Made at the Lick Observatory, University of California, at Mount Hamilton, California, and Santiago, Chile*. Vol. 13. University of California Press, 1918.

[44] E Daddi, M Dickinson, G Morrison, R Chary, A Cimatti, D Elbaz, D Frayer, A Renzini, A Pope, DM Alexander, et al. "Multiwavelength study of massive galaxies at z˜ 2. I. Star formation and galaxy growth." In: *The Astrophysical Journal* 670.1 (2007), p. 156.

[45] Ruth A Daly. "Black hole spins of radio sources." In: *The Astrophysical Journal Letters* 691.2 (2009), p. L72.

[46] Ruth A Daly. "Estimates of black hole spin properties of 55 sources." In: 414.2 (2011), pp. 1253–1262.

[47] Romeel Dave, Renyue Cen, Jeremiah P Ostriker, Greg L Bryan, Lars Hernquist, Neal Katz, David H Weinberg, Michael L Norman, and Brian O'Shea. "Baryons in the warm-hot intergalactic medium." In: *The Astrophysical Journal* 552.2 (2001), p. 473.

[48] Shane W Davis and Ari Laor. "The radiative efficiency of accretion flows in individual active galactic nuclei." In: *The Astrophysical Journal* 728.2 (2011), p. 98.

[49] Walter Dehnen and Hossam Aly. "Improving convergence in smoothed particle hydrodynamics simulations without pairing instability." In: 425.2 (2012), pp. 1068–1082.

[50] AVISHAI Dekel and JOSEPH Silk. "The origin of dwarf galaxies, cold dark matter, and biased galaxy formation." In: *The Astrophysical Journal* 303 (1986), pp. 39–55.

[51] Eduardo F Del Peloso, Licio Da Silva, Gustavo F Porto De Mello, and Lilia I Arany-Prado. "The age of the Galactic thin disk from Th/Eu nucleocosmochronology: extended sample." In: *Proceedings of the International Astronomical Union* 1.S228 (2005), pp. 485–486.

[52] Roberto Della Ceca, Giovanni Lamorani, Tommaso Maccacaro, Anna Wolter, Richard Griffiths, John T Stocke, and Giancarlo Setti. "The properties of X-ray selected active galactic nuclei. 3: The radio-quiet versus radio-loud samples." In: *The Astrophysical Journal* 430 (1994), pp. 533–544.

[53] Tiziana Di Matteo, Volker Springel, and Lars Hernquist. "Energy input from quasars regulates the growth and activity of black holes and their host galaxies." In: *Nature* 433.7026 (2005), pp. 604–607.

[54] Tiziana Di Matteo, Jörg Colberg, Volker Springel, Lars Hernquist, and Debora Sijacki. "Direct cosmological simulations of the growth of black holes and galaxies." In: *The Astrophysical Journal* 676.1 (2008), p. 33.

[55] K Dolag, F Vazza, Gf Brunetti, and G Tormen. "Turbulent gas motions in galaxy cluster simulations: the role of smoothed particle hydrodynamics viscosity." In: 364.3 (2005), pp. 753–772.

[56] Klaus Dolag, M Jubelgas, V Springel, S Borgani, and E Rasia. "Thermal conduction in simulated galaxy clusters." In: *The Astrophysical Journal Letters* 606.2 (2004), p. L97.

[57] Raoul Marie Du Ligondès and Théophile Moreux. *Formation mécanique du système du monde, avec un résumé de la nouvelle théorie*. Vol. 25. Gauthier-Villars et fils, 1897.

[58] RJH Dunn and AC Fabian. "Investigating AGN heating in a sample of nearby clusters." In: *Monthly Notices of the Royal Astronomical Society* 373.3 (2006), pp. 959–971.

[59] L Dunne, RJ Ivison, S Maddox, M Cirasuolo, AM Mortier, S Foucaud, E Ibar, O Almaini, C Simpson, and R McLure. "The star formation history of K-selected galaxies." In: 394.1 (2009), pp. 3–20.

[60] G Efstathiou. "A model of supernova feedback in galaxy formation." In: 317.3 (2000), pp. 697–719.

[61] D Elbaz, E Daddi, D Le Borgne, M Dickinson, DM Alexander, R-R Chary, J-L Starck, WN Brandt, M Kitzbichler, E MacDonald, et al. "The reversal of the star formation-density relation in the distant universe." In: *Astronomy & Astrophysics* 468.1 (2007), pp. 33–48.

[62] D Elbaz, M Dickinson, HS Hwang, T Díaz-Santos, G Magdis, B Magnelli, D Le Borgne, F Galliano, M Pannella, P Chanial, et al. "GOODS–Herschel: an infrared main sequence for star-forming galaxies." In: *Astronomy & Astrophysics* 533 (2011), A119.

[63] Moshe Elitzur and Isaac Shlosman. "The AGN-obscuring Torus: The End of the "Doughnut" Paradigm?" In: *The Astrophysical Journal Letters* 648.2 (2006), p. L101.

[64] Martin Elvis, Belinda J Wilkes, Jonathan C McDowell, Richard F Green, Jill Bechtold, SP Willner, MS Oey, Elisha Polomski, and Roc Cutri. "Atlas of quasar energy distributions." In: *The Astrophysical Journal Supplement Series* 95 (1994), pp. 1–68.

[65] Michael Eracleous and Jules P Halpern. "Doubled-peaked emission lines in active galactic nuclei." In: *The Astrophysical Journal Supplement Series* 90 (1994), pp. 1–30.

[66] AC Fabian. "The obscured growth of massive black holes." In: 308.4 (1999), pp. L39–L43.

[67] AC Fabian. "Observational evidence of active galactic nuclei feedback." In: *Annual Review of Astronomy and Astrophysics* 50 (2012), pp. 455–489.

[68] Andrew C Fabian. "Cooling flows in clusters of galaxies." In: *Annual Review of Astronomy and Astrophysics* 32.1 (1994), pp. 277–318.

[69] D Fabjan, S Borgani, L Tornatore, A Saro, G Murante, and K Dolag. "Simulating the effect of active galactic nuclei feedback on the metal enrichment of galaxy clusters." In: 401.3 (2010), pp. 1670–1690.

[70] Edward Arthur Fath. "The spectra of some spiral nebulae and globular star clusters." In: *Publications of the Astronomical Society of the Pacific* 21.126 (1909), pp. 138–143.

[71] Robert Fender, Stephane Corbel, Tasso Tzioumis, Vince McIntyre, Duncan Campbell-Wilson, Mike Nowak, Ravi Sood, Richard Hunstead, Alan Harmon, Philippe Durouchoux, et al. "Quenching of the radio jet during the X-ray high state of GX 339–4." In: *The Astrophysical Journal Letters* 519.2 (1999), p. L165.

[72] L. Ferrarese and D. Merritt. "A Fundamental Relation between Supermassive Black Holes and Their Host Galaxies." In: *The Astrophysical Journal Letters* 539 (2000), pp. L9–L12.

[73] Laura Ferrarese and David Merritt. "A fundamental relation between supermassive black holes and their host galaxies." In: *The Astrophysical Journal Letters* 539.1 (2000), p. L9.

[74] Georg Feulner, Armin Gabasch, Mara Salvato, Niv Drory, Ulrich Hopp, and Ralf Bender. "Specific star formation rates to redshift 5 from the FORS deep field and the GOODS-S field." In: *The Astrophysical Journal Letters* 633.1 (2005), p. L9.

[75] F Fiore, M Brusa, F Cocchia, A Baldi, N Carangelo, P Ciliegi, A Comastri, F La Franca, R Maiolino, G Matt, et al. "The HELLAS2XMM survey-IV. Optical identifications and the evolution of the accretion luminosity in the Universe." In: *Astronomy & Astrophysics* 409.1 (2003), pp. 79–90.

[76] A Franceschini, S Vercellone, and AC Fabian. "Supermassive black holes in early-type galaxies: relationship with radio emission and constraints on the black hole mass function." In: 297.3 (1998), pp. 817–824.

[77] Juhan Frank, Andrew King, and Derek Raine. *Accretion power in astrophysics*. Cambridge university press, 2002.

[78] Marijn Franx, Pieter G van Dokkum, Natascha M Förster Schreiber, Stijn Wuyts, Ivo Labbé, and Sune Toft. "Structure and star formation in galaxies out to z= 3: evidence for surface density dependent evolution and upsizing." In: *The Astrophysical Journal* 688.2 (2008), p. 770.

[79] Elena Gallo, Robert P Fender, and GG Pooley. "A universal radio–X-ray correlation in low/hard state black hole binaries." In: 344.1 (2003), pp. 60–72.

[80] David Garofalo, Dan A Evans, and Rita M Sambruna. "The evolution of radio-loud active galactic nuclei as a function of black hole spin." In: 406.2 (2010), pp. 975–986.

[81] M Gaspari, M Ruszkowski, and S Peng Oh. "Chaotic cold accretion on to black holes." In: (2013), stt692.

[82] Karl Gebhardt, Ralf Bender, Gary Bower, Alan Dressler, SM Faber, Alexei V Filippenko, Richard Green, Carl Grillmair, Luis C Ho, John Kormendy, et al. "A relationship between nuclear black hole mass and galaxy velocity dispersion." In: *The Astrophysical Journal Letters* 539.1 (2000), p. L13.

[83] Anthony H Gonzalez, Suresh Sivanandam, Ann I Zabludoff, and Dennis Zaritsky. "Galaxy cluster baryon fractions revisited." In: *The Astrophysical Journal* 778.1 (2013), p. 14.

[84] Valentino González, Rychard J Bouwens, Ivo Labbé, Garth Illingworth, Pascal Oesch, Marijn Franx, and Dan Magee. "THE REST-FRAME UV-TO-OPTICAL COLORS AND SPECTRAL ENERGY DISTRIBUTIONS OF z 4-7 GALAXIES." In: *The Astrophysical Journal* 755.2 (2012), p. 148.

[85] Kayhan Gültekin, Douglas O Richstone, Karl Gebhardt, Tod R Lauer, Scott Tremaine, Monique C Aller, Ralf Bender, Alan Dressler, SM Faber, Alexei V Filippenko, et al. "The M-σ and ML relations in galactic bulges, and determinations of their intrinsic scatter." In: *The Astrophysical Journal* 698.1 (2009), p. 198.

[86] F. Haardt and P. Madau. "Radiative Transfer in a Clumpy Universe. II. The Ultraviolet Extragalactic Background." In: *The Astrophysical Journal* 461 (1996), p. 20.

[87] Oliver Hahn, Davide Martizzi, Hao-Yi Wu, August E Evrard, Romain Teyssier, and Risa H Wechsler. "rhapsody-g simulations–I. The cool cores, hot gas and stellar content of massive galaxy clusters." In: 470.1 (2017), pp. 166–186.

[88] Tomohiro Harada, Chul-Moon Yoo, and Kazunori Kohri. "Threshold of primordial black hole formation." In: *Physical Review D* 88.8 (2013), p. 084051.

[89] Lars Hernquist and Neal Katz. "TREESPH-A unification of SPH with the hierarchical tree method." In: *The Astrophysical Journal Supplement Series* 70 (1989), pp. 419–446.

[90] Michaela Hirschmann, Sadegh Khochfar, Andreas Burkert, Thorsten Naab, Shy Genel, and Rachel S Somerville. "On the evolution of the intrinsic scatter in black hole versus galaxy mass relations." In: *Monthly Notices of the Royal Astronomical Society* 407.2 (2010), pp. 1016–1032.

[91] Michaela Hirschmann, Rachel S Somerville, Thorsten Naab, and Andreas Burkert. "Origin of the antihierarchical growth of black holes." In: *Monthly Notices of the Royal Astronomical Society* 426.1 (2012), pp. 237–257.

[92] Michaela Hirschmann, Thorsten Naab, Romeel Davé, Benjamin D Oppenheimer, Jeremiah P Ostriker, Rachel S Somerville, Ludwig Oser, Reinhard Genzel, Linda J Tacconi, Natascha M Förster-Schreiber, et al. "The effect of metal enrichment and galactic winds on galaxy formation in cosmological zoom simulations." In: *Monthly Notices of the Royal Astronomical Society* 436.4 (2013), pp. 2929–2949.

[93] Michaela Hirschmann, Klaus Dolag, Alexandro Saro, Lisa Bachmann, Stefano Borgani, and Andreas Burkert. "Cosmological simulations of black hole growth: AGN luminosities and downsizing." In: 442.3 (2014), pp. 2304–2324.

[94] Luis C Ho. "On the relationship between radio emission and black hole mass in galactic nuclei." In: *The Astrophysical Journal* 564.1 (2002), p. 120.

[95] Roger W Hockney and James W Eastwood. *Computer simulation using particles*. crc Press, 1988.

[96] Erik Holmberg. "On the Clustering Tendencies among the Nebulae. II. a Study of Encounters Between Laboratory Models of Stellar Systems by a New Integration Procedure." In: *The Astrophysical Journal* 94 (1941), p. 385.

[97] Andrew M Hopkins and John F Beacom. "On the normalization of the cosmic star formation history." In: *The Astrophysical Journal* 651.1 (2006), p. 142.

[98] Fred Hoyle and William A Fowler. "On the nature of strong radio sources." In: 125.2 (1962), pp. 169–176.

[99] Fred Hoyle and Raymond A Lyttleton. "The effect of interstellar matter on climatic variation." In: *Mathematical Proceedings of the Cambridge Philosophical Society*. Vol. 35. 03. Cambridge Univ Press. 1939, pp. 405–415.

[100] Edwin P Hubble. "Extragalactic nebulae." In: *The Astrophysical Journal* 64 (1926).

[101] W Ishibashi and AC Fabian. "Active galactic nucleus feedback and triggering of star formation in galaxies." In: 427.4 (2012), pp. 2998–3005.

[102] Ranty R Islam, James E Taylor, and Joseph Silk. "Massive black hole remnants of the first stars in galactic haloes." In: *Monthly Notices of the Royal Astronomical Society* 340.2 (2003), pp. 647–656.

[103] Knud Jahnke and Andrea V Macciò. "The non-causal origin of the black-hole-galaxy scaling relations." In: *The Astrophysical Journal* 734.2 (2011), p. 92.

[104] PH Johansson and G Efstathiou. "A model for the metallicity evolution of damped Lyman α systems." In: 371.3 (2006), pp. 1519–1535.

[105] Neal Katz, David H Weinberg, and Lars Hernquist. "Cosmological simulations with TreeSPH." In: *arXiv preprint astro-ph/9509107* (1995).

[106] Brandon C Kelly and Yue Shen. "The demographics of broad-line quasars in the mass-luminosity plane. II. Black hole mass and eddington ratio functions." In: *The Astrophysical Journal* 764.1 (2013), p. 45.

[107] Brandon C Kelly, Marianne Vestergaard, Xiaohui Fan, Philip Hopkins, Lars Hernquist, and Aneta Siemiginowska. "Constraints on black hole growth, quasar lifetimes, and Eddington ratio distributions from the SDSS broad-line quasar black hole mass function." In: *The Astrophysical Journal* 719.2 (2010), p. 1315.

[108] P Kharb, ML Lister, and NJ Cooper. "Extended radio emission in MOJAVE Blazars: Challenges to Unification." In: *The Astrophysical Journal* 710.1 (2010), p. 764.

[109] Ji-hoon Kim, John H Wise, Marcelo A Alvarez, and Tom Abel. "Galaxy formation with self-consistently modeled stars and massive black holes. i. feedback-regulated star formation and black hole growth." In: *The Astrophysical Journal* 738.1 (2011), p. 54.

[110] Juhan Kim, Changbom Park, Graziano Rossi, Sang Min Lee, and J Richard Gott III. "The New Horizon Run Cosmological N-Body Simulations." In: *Journal of Korean Astronomical Society* 44 (2011), pp. 217–234.

[111] Andrew King. "Black holes, galaxy formation, and the MBH-σ relation." In: *The Astrophysical Journal Letters* 596.1 (2003), p. L27.

[112] Juna A Kollmeier, Christopher A Onken, Christopher S Kochanek, Andrew Gould, David H Weinberg, Matthias Dietrich, Richard Cool, Arjun Dey, Daniel J Eisenstein, Buell T Jannuzi, et al. "Black hole masses and eddington ratios at 0.3< z< 4." In: *The Astrophysical Journal* 648.1 (2006), p. 128.

[113] John Kormendy and Douglas Richstone. "Inward bound—the search for supermassive black holes in galactic nuclei." In: *Annual Review of Astronomy and Astrophysics* 33.1 (1995), pp. 581–624.

[114] Dharam V Lal, Prajval Shastri, and Denise C Gabuzda. "Seyfert Galaxies: Nuclear Radio Structure and Unification." In: *The Astrophysical Journal* 731.1 (2011), p. 68.

[115] Yen-Ting Lin, Joseph J Mohr, and S Adam Stanford. "Near-infrared properties of galaxy clusters: luminosity as a binding mass predictor and the state of cluster baryons." In: *The Astrophysical Journal* 591.2 (2003), p. 749.

[116] Thomas J Maccarone, Arunav Kundu, Stephen E Zepf, and Katherine L Rhode. "A black hole in a globular cluster." In: *Nature* 445.7124 (2007), pp. 183–185.

[117] Piero Madau and Martin J Rees. "Massive black holes as population III remnants." In: *The Astrophysical Journal Letters* 551.1 (2001), p. L27.

[118] Karl Mannheim. "On the Difference Between Radio Loud and Radio Quiet AGN." In: *Symposium-International Astronomical Union*. Vol. 159. Cambridge Univ Press. 1994, pp. 285–288.

[119] BJ Maughan, C Jones, W Forman, and L Van Speybroeck. "Images, structural properties, and metal abundances of galaxy clusters observed with Chandra ACIS-I at 0.1< z< 1.3." In: *The Astrophysical Journal Supplement Series* 174.1 (2008), p. 117.

[120] Ian G McCarthy, Joop Schaye, Trevor J Ponman, Richard G Bower, Craig M Booth, C Dalla Vecchia, Robert A Crain, Volker Springel, Tom Theuns, and Robert PC Wiersma. "The case for AGN feedback in galaxy groups." In: 406.2 (2010), pp. 822–839.

[121] Nicholas J McConnell and Chung-Pei Ma. "Revisiting the scaling relations of black hole masses and host galaxy properties." In: *The Astrophysical Journal* 764.2 (2013), p. 184.

[122] Christopher F McKee and Jeremiah P Ostriker. "A theory of the interstellar medium-Three components regulated by supernova explosions in an inhomogeneous substrate." In: *The Astrophysical Journal* 218 (1977), pp. 148–169.

[123] BR McNamara, M Wise, PEJ Nulsen, LP David, CL Sarazin, M Bautz, M Markevitch, A Vikhlinin, WR Forman, C Jones, et al. "Chandra X-ray observations of the Hydra A cluster: an interaction between the radio source and the X-ray-emitting gas." In: *The Astrophysical Journal Letters* 534.2 (2000), p. L135.

[124] Andrea Merloni and Sebastian Heinz. "Cosmological evolution of the AGN kinetic luminosity function." In: *Proceedings of the International Astronomical Union* 2.S238 (2006), pp. 65–70.

[125] M Mezcua and MA Prieto. "Evidence of parsec-scale jets in Low-luminosity Active Galactic Nuclei." In: *The Astrophysical Journal* 787.1 (2014), p. 62.

[126] JJ Monaghan. "SPH and Riemann solvers." In: *Journal of Computational Physics* 136.2 (1997), pp. 298–307.

[127] Forest R Moulton. "On the evolution of the solar system." In: *The Astrophysical Journal* 22 (1905), p. 165.

[128] R. Narayan and I. Yi. "Advection-dominated accretion: A self-similar solution." In: *The Astrophysical Journal* 428 (1994), pp. L13–L16.

[129] Ramesh Narayan and Eliot Quataert. "Black hole accretion." In: *Science* 307.5706 (2005), pp. 77–80.

[130] Charles H Nelson. "Black hole mass, velocity dispersion, and the radio source in active galactic nuclei." In: *The Astrophysical Journal Letters* 544.2 (2000), p. L91.

[131] Ludwig Oser, Jeremiah P Ostriker, Thorsten Naab, Peter H Johansson, and Andreas Burkert. "The two phases of galaxy formation." In: *The Astrophysical Journal* 725.2 (2010), p. 2312.

[132] R Pakmor, P Edelmann, FK Röpke, and W Hillebrandt. "Stellar GADGET: a smoothed particle hydrodynamics code for stellar astrophysics and its application to Type Ia supernovae from white dwarf mergers." In: 424.3 (2012), pp. 2222–2231.

[133] Jorge Peñarrubia, Yin-Zhe Ma, Matthew G Walker, and Alan McConnachie. "A dynamical model of the local cosmic expansion." In: 443.3 (2014), pp. 2204–2222.

[134] Roger Penrose. ""Golden Oldie": Gravitational Collapse: The Role of General Relativity." In: *General Relativity and Gravitation* 34.7 (2002), pp. 1141–1165.

[135] Bradley M Peterson. *An introduction to active galactic nuclei*. Cambridge University Press, 1997.

[136] Edward A Pier and Julian H Krolik. "Infrared spectra of obscuring dust tori around active galactic nuclei. I-Calculational method and basic trends." In: *The Astrophysical Journal* 401 (1992), pp. 99–109.

[137] S Planelles, S Borgani, D Fabjan, M Killedar, G Murante, GL Granato, C Ragone-Figueroa, and K Dolag. "On the role of AGN feedback on the thermal and chemodynamical properties of the hot intracluster medium." In: (2013), stt2141.

[138] Chris Power, JF Navarro, A Jenkins, CS Frenk, Simon DM White, V Springel, J Stadel, and T Quinn. "The inner structure of ΛCDM haloes—I. A numerical convergence study." In: 338.1 (2003), pp. 14–34.

[139] Daniel J Price. "Modelling discontinuities and Kelvin–Helmholtz instabilities in SPH." In: *Journal of Computational Physics* 227.24 (2008), pp. 10040–10057.

[140] MA Prieto, J Reunanen, KRW Tristram, N Neumayer, JA Fernandez-Ontiveros, M Orienti, and K Meisenheimer. "The spectral energy distribution of the central parsecs of the nearest AGN." In: 402.2 (2010), pp. 724–744.

[141] E Rasia, S Borgani, G Murante, S Planelles, AM Beck, V Biffi, C Ragone-Figueroa, GL Granato, LK Steinborn, and K Dolag. "Cool Core Clusters from Cosmological Simulations." In: *The Astrophysical Journal Letters* 813.1 (2015), p. L17.

[142] Grote Reber. "Notes: Cosmic Static." In: *The Astrophysical Journal* 91 (1940), pp. 621–624.

[143] JN Reeves, PT O'Brien, V Braito, E Behar, L Miller, TJ Turner, AC Fabian, S Kaspi, R Mushotzky, and M Ward. "A Compton-thick wind in the high-luminosity quasar, PDS 456." In: *The Astrophysical Journal* 701.1 (2009), p. 493.

[144] Rhea-Silvia Remus. "The outer halos of elliptical galaxies : implications for their formation histories." In: (2015).

[145] Brant Robertson, James S Bullock, Thomas J Cox, Tiziana Di Matteo, Lars Hernquist, Volker Springel, and Naoki Yoshida. "A merger-driven scenario for cosmological disk galaxy formation." In: *The Astrophysical Journal* 645.2 (2006), p. 986.

[146] Carl L Rodriguez, Meagan Morscher, Bharath Pattabiraman, Sourav Chatterjee, Carl-Johan Haster, and Frederic A Rasio. "Binary Black Hole Mergers from Globular Clusters: Implications for Advanced LIGO." In: *Physical Review Letters* 115.5 (2015), p. 051101.

[147] HR Russell, BR McNamara, AC Edge, MT Hogan, RA Main, and AN Vantyghem. "Radiative efficiency, variability and Bondi accretion on to massive black holes: the transition from radio AGN to quasars in brightest cluster galaxies." In: 432.1 (2013), pp. 530–553.

[148] Samir Salim, R Michael Rich, Stéphane Charlot, Jarle Brinchmann, Benjamin D Johnson, David Schiminovich, Mark Seibert, Ryan Mallery, Timothy M Heckman, Karl Forster, et al. "UV star formation rates in the local universe." In: *The Astrophysical Journal Supplement Series* 173.2 (2007), p. 267.

[149] EE Salpeter. "Accretion of interstellar matter by massive objects." In: *The Astrophysical Journal* 140 (1964), pp. 796–800.

[150] Edwin E Salpeter. "The Luminosity Function and Stellar Evolution." In: *The Astrophysical Journal* 121 (1955), p. 161.

[151] Kevin Schawinski, Daniel Thomas, Marc Sarzi, Claudia Maraston, Sugata Kaviraj, Seok-Joo Joo, K Yi Sukyoung, and Joseph Silk. "Observational evidence for AGN feedback in early-type galaxies." In: 382.4 (2007), pp. 1415–1431.

[152] Joop Schaye, Robert A Crain, Richard G Bower, Michelle Furlong, Matthieu Schaller, Tom Theuns, Claudio Dalla Vecchia, Carlos S Frenk, IG McCarthy, John C Helly, et al. "The EAGLE project: simulating the evolution and assembly of galaxies and their environments." In: 446.1 (2015), pp. 521–554.

[153] David Schiminovich, Barbara Catinella, Guinevere Kauffmann, Silvia Fabello, Jing Wang, Cameron Hummels, Jenna Lemonias, Sean M Moran, Ronin Wu, Riccardo Giovanelli, et al. "The GALEX Arecibo SDSS Survey–II. The star formation efficiency of massive galaxies." In: 408.2 (2010), pp. 919–934.

[154] A Schulze, A Bongiorno, I Gavignaud, M Schramm, J Silverman, A Merloni, G Zamorani, M Hirschmann, V Mainieri, L Wisotzki, et al. "The cosmic growth of the active black hole population at 1." In: 447.3 (2015), pp. 2085–2111.

[155] Andreas Schulze and Lutz Wisotzki. "Low redshift AGN in the Hamburg/ESO Survey-II. The active black hole mass function and the distribution function of Eddington ratios." In: *Astronomy & Astrophysics* 516 (2010), A87.

[156] Carl K Seyfert. "Nuclear Emission in Spiral Nebulae." In: *The Astrophysical Journal* 97 (1943), p. 28.

[157] N.I. Shakura and R. A. Sunyaev. "Black holes in binary systems. Observational appearance." In: *Annual Review of Astronomy and Astrophysics* 24 (1973), pp. 337–355.

[158] Yue Shen and Brandon C Kelly. "The demographics of broad-line quasars in the mass-luminosity plane. I. Testing FWHM-based virial black hole masses." In: *The Astrophysical Journal* 746.2 (2012), p. 169.

[159] Debora Sijacki and Volker Springel. "Physical viscosity in smoothed particle hydrodynamics simulations of galaxy clusters." In: 371.3 (2006), pp. 1025–1046.

[160] J. Silk and M. J. Rees. "Quasars and galaxy formation." In: *Astronomy and Astrophysics* 331 (1998), pp. L1–L4.

[161] Joseph Silk. "Unleashing Positive Feedback: Linking the Rates of Star Formation, Supermassive Black Hole Accretion, and Outflows in Distant Galaxies." In: *The Astrophysical Journal* 772.2 (2013), p. 112.

[162] Vesto Melvin Slipher. "The spectrum and velocity of the nebula NGC 1068 (M 77)." In: *Lowell Observatory Bulletin* 3 (1917), pp. 59–62.

[163] Volker Springel. "The cosmological simulation code GADGET-2." In: 364.4 (2005), pp. 1105–1134.

[164] Volker Springel, Tiziana Di Matteo, and Lars Hernquist. "Modelling feedback from stars and black holes in galaxy mergers." In: 361.3 (2005), pp. 776–794.

[165] Volker Springel and Lars Hernquist. "Cosmological smoothed particle hydrodynamics simulations: the entropy equation." In: 333.3 (2002), pp. 649–664.

[166] Volker Springel and Lars Hernquist. "Cosmological smoothed particle hydrodynamics simulations: a hybrid multiphase model for star formation." In: 339.2 (2003), pp. 289–311.

[167] Volker Springel, Jie Wang, Mark Vogelsberger, Aaron Ludlow, Adrian Jenkins, Amina Helmi, Julio F Navarro, Carlos S Frenk, and Simon DM White. "The Aquarius Project: the subhaloes of galactic haloes." In: 391.4 (2008), pp. 1685–1711.

[168] RA Sramek and DW Weedman. "The radio properties of optically discovered quasars." In: *The Astrophysical Journal* 238 (1980), pp. 435–444.

[169] Daniel P Stark, Richard S Ellis, Andrew Bunker, Kevin Bundy, Tom Targett, Andrew Benson, and Mark Lacy. "The evolutionary history of Lyman break galaxies between redshift 4 and 6: observing successive generations of massive galaxies in formation." In: *The Astrophysical Journal* 697.2 (2009), p. 1493.

[170] Daniel P Stark, Matthew A Schenker, Richard Ellis, Brant Robertson, Ross McLure, and James Dunlop. "Keck spectroscopy of $3< z< 7$ faint Lyman break galaxies: the importance of nebular emission in understanding the specific star formation rate and stellar mass density." In: *The Astrophysical Journal* 763.2 (2013), p. 129.

[171] Lisa K Steinborn, Klaus Dolag, Michaela Hirschmann, M Almudena Prieto, and Rhea-Silvia Remus. "A refined sub-grid model for black hole accretion and AGN feedback in large cosmological simulations." In: 448.2 (2015), pp. 1504–1525.

[172] Charles L Steinhardt and Martin Elvis. "The quasar mass–luminosity plane– I. A sub-Eddington limit for quasars." In: 402.4 (2010), pp. 2637–2648.

[173] John T Stocke, Simon L Morris, IM Gioia, T Maccacaro, R Schild, A Wolter, Thomas A Fleming, and J Patrick Henry. “The Einstein observatory extended medium-sensitivity survey. II-the optical identifications.” In: *The Astrophysical Journal Supplement Series* 76 (1991), pp. 813–874.

[174] Chris Stoughton, Robert H Lupton, Mariangela Bernardi, Michael R Blanton, Scott Burles, Francisco J Castander, AJ Connolly, Daniel J Eisenstein, Joshua A Frieman, GS Hennessy, et al. “Sloan digital sky survey: early data release.” In: *The Astronomical Journal* 123.1 (2002), p. 485.

[175] LJ Tacconi, R Genzel, R Neri, P Cox, MC Cooper, KL Shapiro, A Bolatto, N Bouché, F Bournaud, A Burkert, et al. “High molecular gas fractions in normal massive star forming galaxies in the young Universe.” In: *arXiv preprint arXiv:1002.2149* (2010).

[176] LJ Tacconi, R Neri, R Genzel, Francoise Combes, A Bolatto, Michael C Cooper, S Wuyts, F Bournaud, A Burkert, J Comerford, et al. “Phibss: molecular gas content and scaling relations in z 1-3 massive, main-sequence star-forming galaxies.” In: *The Astrophysical Journal* 768.1 (2013), p. 74.

[177] Clive Tadhunter. “An introduction to active galactic nuclei: Classification and unification.” In: *New Astronomy Reviews* 52.6 (2008), pp. 227–239.

[178] F Tombesi, M Cappi, JN Reeves, GGC Palumbo, T Yaqoob, V Braito, and M Dadina. “Evidence for ultra-fast outflows in radio-quiet AGNs-I. Detection and statistical incidence of Fe K-shell absorption lines.” In: *Astronomy & Astrophysics* 521 (2010), A57.

[179] Alar Toomre. “Gravitational interactions between galaxies.” In: *The formation and dynamics of galaxies*. Springer, 1974, pp. 347–365.

[180] Alar Toomre and Juri Toomre. “Galactic bridges and tails.” In: *The Astrophysical Journal* 178 (1972), pp. 623–666.

[181] Scott Tremaine, Karl Gebhardt, Ralf Bender, Gary Bower, Alan Dressler, S Mi Faber, Alexei V Filippenko, Richard Green, Carl Grillmair, Luis C Ho, et al. “The slope of the black hole mass versus velocity dispersion correlation.” In: *The Astrophysical Journal* 574.2 (2002), p. 740.

[182] P Valageas, R Schaeffer, and Joseph Silk. “The phase-diagram of cosmological baryons.” In: *Astronomy & Astrophysics* 388.3 (2002), pp. 741–757.

[183] Patrick Valageas, Richard Schaeffer, and Joseph Silk. “The phase diagram of the intergalactic medium and the entropy floor of groups and clusters: are clusters born warm?” In: 344.1 (2003), pp. 53–59.

[184] M-P Véron-Cetty and Philippe Véron. “A catalogue of quasars and active nuclei.” In: *Astronomy & Astrophysics* 518 (2010), A10.

[185] Marianne Vestergaard. “Occurrence and Global Properties of Narrow C IV λ1549 Å Absorption Lines in Moderate-Redshift Quasars.” In: *The Astrophysical Journal* 599.1 (2003), p. 116.

[186] Marta Volonteri and Priyamvada Natarajan. “Journey to the M BH–σ relation: the fate of low-mass black holes in the Universe.” In: *Monthly Notices of the Royal Astronomical Society* 400.4 (2009), pp. 1911–1918.

[187] Sebastian Von Hoerner. "Die numerische integration des n-körper-problemes für sternhaufen. i." In: *Zeitschrift fur Astrophysik* 50 (1960).

[188] R. Weinberger et al. "Simulating galaxy formation with black hole driven thermal and kinetic feedback." In: 465 (2017), pp. 3291–3308.

[189] Rainer Weinberger, Volker Springel, Lars Hernquist, Annalisa Pillepich, Federico Marinacci, Rüdiger Pakmor, Dylan Nelson, Shy Genel, Mark Vogelsberger, Jill Naiman, et al. "Simulating galaxy formation with black hole driven thermal and kinetic feedback." In: 465.3 (2016), pp. 3291–3308.

[190] Fred L Whipple and Jesse L Greenstein. "On the origin of interstellar radio disturbances." In: *Proceedings of the National Academy of Sciences* 23.3 (1937), pp. 177–181.

[191] Lodewijk Woltjer. "Emission Nuclei in Galaxies." In: *The Astrophysical Journal* 130 (1959), p. 38.

[192] H-Y Karen Yang and Christopher S Reynolds. "HOW AGN JETS HEAT THE INTRACLUSTER MEDIUM—INSIGHTS FROM HYDRODYNAMIC SIMULATIONS." In: *The Astrophysical Journal* 829.2 (2016), p. 90.

[193] Ya B Zel'dovich and ID Novikov. "The radiation of gravity waves by bodies moving in the field of a collapsing star." In: *Soviet Physics Doklady*. Vol. 9. 1964, p. 246.

[194] XZ Zheng, EF Bell, RS Somerville, H-W Rix, K Jahnke, F Fontanot, GH Rieke, D Schiminovich, and K Meisenheimer. "Observational constraints on the co-evolution of supermassive black holes and galaxies." In: *The Astrophysical Journal* 707.2 (2009), p. 1566.

[195] Kastytis Zubovas and Andrew R King. "The M–σ relation in different environments." In: 426.4 (2012), pp. 2751–2757.

ACKNOWLEDGMENTS

First and foremost I want to thank my supervisor Dr. Klaus Dolag for making it possible for me to work together with the Universitäts-Sternwarte München (USM) of the LMU and the Osservatorio Astronomico di Trieste (OATs) of INAF. Equally grateful am I to Dr. Stefano Borgani and Dr. Giuseppe Murante, who made my stay in Trieste a truly scholarly one. Furthermore am I indebted to Dr. Dunja Fabian, who helped me to achieve more insights.
A thanks goes to the people I had the chance to get to know in Munich, with whom I spend uncountable joyful moments playing music or games, wandering through the nights, exploring the mountains and friendly discussions from which everyone emerged always wiser.
Last but most important do I want to recognize the unbreakable believe of my family in me, without which I wouldn't have come so far.

ERKLÄRUNG

Hiermit erkläre ich, die vorliegende Arbeit selbständig verfasst zu haben und keine anderen als die in der Arbeit angegebenen Quellen und Hilfsmittel benutzt zu haben.

München, 9. August 2017

Christoph Becker